



저작자표시-비영리-변경금지 2.0 대한민국

이용자는 아래의 조건을 따르는 경우에 한하여 자유롭게

- 이 저작물을 복제, 배포, 전송, 전시, 공연 및 방송할 수 있습니다.

다음과 같은 조건을 따라야 합니다:



저작자표시. 귀하는 원저작자를 표시하여야 합니다.



비영리. 귀하는 이 저작물을 영리 목적으로 이용할 수 없습니다.



변경금지. 귀하는 이 저작물을 개작, 변형 또는 가공할 수 없습니다.

- 귀하는, 이 저작물의 재이용이나 배포의 경우, 이 저작물에 적용된 이용허락조건을 명확하게 나타내어야 합니다.
- 저작권자로부터 별도의 허가를 받으면 이러한 조건들은 적용되지 않습니다.

저작권법에 따른 이용자의 권리는 위의 내용에 의하여 영향을 받지 않습니다.

이것은 [이용허락규약\(Legal Code\)](#)을 이해하기 쉽게 요약한 것입니다.

[Disclaimer](#)

이학박사 학위논문

# Highly Controlled Noble Metal Nanostructures Synthesis and Their Optical/Catalytic Properties

고도로 제어된 귀금속 나노구조체의  
합성 및 광학/촉매 특성

2022년 8월

서울대학교 대학원

화학부 무기화학

이 정 연

# Highly Controlled Noble Metal Nanostructures Synthesis and Their Optical/Catalytic Properties

고도로 제어된 귀금속 나노구조체의 합성 및  
광학/촉매 특성

지도교수 남 좌 민

이 논문을 이학박사 학위논문으로 제출함  
2022년 8월

서울대학교 대학원  
화학부 무기화학  
이 정 연

이정연의 이학박사 학위논문을 인준함  
2022년 8월

위 원 장	<u>          홍  병  희          </u>	(인)
부위원장	<u>          남  좌  민          </u>	(인)
위  원	<u>          임  중  우          </u>	(인)
위  원	<u>          이  윤  호          </u>	(인)
위  원	<u>          오  정  욱          </u>	(인)

## Abstract

# Highly Controlled Noble Metal Nanostructures Synthesis and Their Optical/Catalytic Properties

Chungyeon Lee

Department of Chemistry

The Graduate School

Seoul National University

Recently, expansion in the applications of metal nanoparticles has resulted in increased demand for particle control. Understanding how to control nanoparticles can provide insight into the design and synthesis of more suitable structures for optical and catalytic applications. Herein, an optimal Au nanostructure for quantitative surface-enhanced Raman scattering (SERS) and a highly active electro-oxidation ethanol reaction (EOR) is presented. Intragap nanostructures with nanometer-scale intragaps show reliability as well as quantitative and increased stability of the SERS signal as the Raman molecules are located inside the fixed size gap. Although various methods for the synthesis of intragap nanostructures have been developed, there is still a demand for an increased understanding of the factors that affect the SERS uniformity and stability that occur in the intragap, for practical applications. Therefore, precise

control and synthesis of well-defined intragap nanoparticles with consideration of SERS variables is important. Owing to its high surface-to-volume structural characteristics, the nanoporous structure is attractive for electrochemical reaction catalysts. Most existing metal nanoporous structures are porous Au thin films, and their structures are fabricated by dealloying. Compared with the Au nanoporous film, Au porous nanoparticles show a higher surface-to-volume ratio, and their ligaments are more curved in a small volume and can inevitably expose many surface defects. However, the developed Au nanoporous particles require a rough and complex multi-step synthesis for alloying–dealloying. Therefore, a method for the facile synthesis of Au nanoporous particles under mild conditions should be devised for the large-scale production of catalysts with advanced performance.

This thesis suggests highly controlled metal nanostructures composed of Au and the fabrication methods for the most efficient optical and catalytic performance. In particular, for reliable and quantitative SERS applications, the intragap shape of intragap nanoparticles is highly controlled, and the effect of optical uniformity and stability is investigated. Furthermore, to enhance the electrocatalytic efficiency of Au-based nanoparticles, porous Au nanoparticles with abundant active sites were fabricated using the alloying–dealloying process. Additionally, by adjusting the Au-to-Ag ratio of the alloy nanoparticles during the process, the Au nanoporous structure can be optimized for enhanced surface-defect-dependent catalytic activity.

Chapter 1 provides an overview of noble metal nanoparticle synthesis and its various applications. First, we reviewed the principles of fabrication and control of Au-based nanoparticles for optimized SERS and electrocatalysis. In particular, Au-based intragap nanoparticles and porous structure synthetic methods were introduced. We then investigated the SERS and electrocatalyst applications of the highly controlled nanoparticles and studied their influencing factors.

Chapter 2 presents highly controlled single-crystalline smooth intragap nanoparticles (SSINs) for reliable and quantitative surface-enhanced Raman scattering (SERS). We investigated the impact of the intragap shape on the amplified SERS intensity and uniformity of each nanoparticle and compared it to polycrystalline rough intragap nanoparticles (PRINs). Further, the well-defined and stable structure exhibited an increasingly constant and reliable signal under harsh laser exposure.

Chapter 3 presents the rational design of a highly porous Au-Ag alloy Knotted Nano Ball (KNB). Precise regulation of the relative reduction rates of Au and Ag during seed-mediated growth, followed by a dealloying reaction, facilitates the formation of highly porous Au-Ag alloy nanoparticles, which are easily adjustable for synthesizing nanoparticles of different pore sizes. The optimized pore size of the nanoparticles showed the highest mass activity among the Au-based catalysis EOR. We argued that the different ratios of ligament surface defects on different nanostructures play an important role in the mass activity and

specific activity of the EOR reaction.

In conclusion, well-designed, high-yield nanoparticles will achieve maximum efficiency in specific applications and have the potential to become essential for the practical commercial use of nanoparticles in the future. For this reason, a synthetic understanding that can control nanoparticles into desired shapes is essential, and we must consider the influencing factors in particular applications and optimize them.

**Keyword : Noble Metal Nanostructure, Plasmonic Intragap nanoparticle, Nanoporous Gold Structure, Surface-Enhanced Raman Scattering(SERS), Electro-Ethanol oxidation Reaction**

**Student Number : 2015-20397**

# Contents

<b>Abstract</b> .....	i
<b>Contents</b> .....	iv
<b>List of Figures</b> .....	vi
<b>List of Tables</b> .....	xiv
<b>Citations to Previously Published Works</b> .....	xv

## **Chapter 1. Introduction: Highly Controlled Noble Metal Nanostructures Synthesis and Their Applications...1**

1.1 Introduction .....	2
1.2 Plasmonic Nanogap Structure Synthesis and Their Optical Studies .....	3
1.3 Nanoporous Structure Synthesis and Their Catalytic Studies.....	28
1.4 Conclusion.....	41
1.5 References .....	42

## **Chapter 2. The Effect of Intragap Morphology of Inta-nanogap Particle on the SERS Uniformity and Stability .....53**

2.1 Introduction.....	54
2.2 Experimental Section .....	56
2.3 Results and Discussion .....	63
2.4 Conclusion .....	84
2.5 References.....	86

<b>Chapter 3. Kinetically Controlled Synthesis of Au-Ag Alloy Knotted Nano Ball(KNB): Enhanced Ethanol Electro- oxidation .....</b>	<b>90</b>
3.1 Introduction.....	91
3.2 Experimental Section .....	93
3.3 Results and Discussion .....	98
3.4 Conclusion .....	127
3.5 References.....	128
<b>Abstract in Korean .....</b>	<b>131</b>

# List of Figures

- Figure 1.1** Plasmonic gap nanostructures with their optical properties and sensing applications. ....4
- Figure 1.2** Schematic illustration of three different types of growth modes. (A) Depositing metal preferably deposit onto the core metal particles, epitaxially in a layer-by-layer fashion. Frank-van der Merwe (FM) mode. (B) Depositing metal grow on the high energy sites of substrate metal particles and forms island in order to minimize strain energy. Volmer-Weber (VW) mode. (C) Depositing metal and core metal particles has relatively large lattice mismatch occurs Stranski-Krastanov (SK) mode .....8
- Figure 1.3** Intragap nanoparticle formation strategies. (A) Single-strand thiolated-DNA-based intragap formation in AuNNPs. (B) Programmable gap morphology by varying DNA sequences. (C) Cyclodextrin-based intranogap particles (CIP) capable of accommodating 10 different Raman dyes. (D) Verified intragap size via different surface density of 1,4-BDT of GERT. (E) Silica dielectric intragap of nanomatryoshilka. (F) Polydopamine based intragap formation and multishell plasmonic nanogapped particles via metallization. (G) Selective, interdiffusive dealloying (SID) based formation of dealloyed intragap particles. .... 13
- Figure 1.4** Optical properties of nanogap particles. (A) Wavelength shift of the plamone resonance depending on the gap size, which is controlled by UV-irradiation. (B) Subangstrom gap size control in NPoM constructs via central lanthanide ion and their corresponding resonance wavelengths. (C) Wavelength shift of the plasmon

resonance of Au nanocube-Au nanosphere dimers with different gap morphology.  
 .....20

**Figure 1.5** Optical properties of nanogap particles. (A) Modified Raman selection rules depending on atomic protrusions in the nanogap. (B) Wavelength shift of the plasmon resonance in NPoM systems depending on the conductance of the molecules in the nanogap. (C) Metal composition-dependent far- and near-field properties of intragap particles. ....25

**Figure 1.6** AgCl sacrificial crystal and aligned microporous film-template-based nanoporous Au formation. (A) Synthesis scheme for nanoporous hollow Au nanoparticles using AuCl as a sacrificial template, and representative SEM image of the corresponding steps. (B) Synthetic method and SEM of macroporous Au films by filled with Au nanoparticle on the ordered microporous PS crystal film followed by removing PS templates and copper hydroxide nanostrand layer. ....29

**Figure 1.7** The structure and mechanism of evolution in dealloying of nanoporous Au. (A) The cross-section scanning electron micrographs(SEM) of dealloyed nanoporous Au thin film. (B) Working model for nanoporous Au evolution from Au-Ag alloy system (Au atom, orange; Ag atom, gray). The Dealloying process begins with selectively dissolved Ag atoms (less noble metal) from homogeneous Au-Ag alloy. As dealloying continues, surface diffusion of Au atoms (noble metal) passivates Ag-etched surface sites. This process generates bicontinuous nanoporous with ligaments with Au-rich surfaces and Ag-rich interiors. 31

**Figure 1.8** Substrate-based and free-standing synthesis of nanoporous Au. (A) Schematic

formation pathway for substrate-based synthesis of porous Au nanoparticles combining the dewetting process and dealloying and the corresponding SEM images of the contour of the porous Au nanoparticles. (B) Optical and SEM images of white-gold leaf before and after dealloying. Chemically dealloying in nitric acid for 15 min results in a free-standing nanoporous gold membrane.

.....33

**Figure 1.9** Dealloying-based Au porous nanoparticles synthesis. (A) Au-Ag alloy was obtained by subjected to high-temperature annealing (950°C) from Au core-Ag shell under silica shell protection. After chemical dealloying, AuAg@void@SiO<sub>2</sub> nanoparticle was fabricated. (B) A facile synthetic method for Au core/porous shell nanoparticles by co-reduction of Au and Ag on the nanoparticle core and chemical dealloying. ....35

**Figure 1.10** Various porosity and surface atomic structure of Au nanoporous catalyst. (A) Schematic illustration of synthesizing various Au nanoporous structures, and different reaction pathways according to the pore size. (B) TEM and HAADF-STEM images of nanopore show (100) surface plane with atomic kinks and (111) surface plane with monoatomic layer island, convex terrace, and concave stepped surface along the edge. ....39

**Figure 2.1** Synthetic strategy of singlecrystalline smooth intragap nanoparticles (SSINs) and polycrystalline rough intragap nanoparticles (PRINs). Scheme for synthesizing SSINs and PRINs through a galvanic/reduction reaction (GRR) and selective-interdiffusive dealloying (SID) process, respectively. ....64

**Figure 2.2** (A) TEM and (B) UV-Vis extinction of 40 nm Au nanosphere particles

(AuNSs) .	66
<b>Figure 2.3</b> Different reducing agent effects on the silver shell Au core-Ag shell formation with (A) AA and (B) L-SA.	66
<b>Figure 2.4</b> NH <sub>4</sub> OH concentration and NaOH effects on the silver shell formation (A) 0.1 M NH <sub>4</sub> OH (B) 0.1 M NaOH (C) stock NH <sub>4</sub> OH (D) without NH <sub>4</sub> OH.	67
<b>Figure 2.5</b> Temperature effect on the Au shell morphology during galvanic/reduction reaction (A) 90 °C, (B) 60 °C, (C) 25 °C.	68
<b>Figure 2.6</b> Synthetic strategy and structural analysis singlecrystalline smooth intragap nanoparticles (SSINs) and polycrystalline rough intragap nanoparticles (PRINs). HAADF-STEM and HR-TEM images of (A) SSINs, (B) PRINs shows smooth and rough intragap. HR-TEM image and Selective area electron diffraction (SAED) pattern of shell region showing the singlecrystalline structure of (C) SSINs and polycrystalline structure of (D) PRINs. (E) The intragap size ( $r_2-r_1$ ) distribution at the specific rotation angle in single nanoparticle. Intragap size distributions of 100 particles of (F) SSINs and (G) PRINs which were analyzed from the TEM images.	70
<b>Figure 2.7</b> TEM images of SSINs.	73
<b>Figure 2.8</b> Nanogap size, shell thickness, and particle size distributions of (A-B) PRINs and (C-D) SSINs. The TEM images of 100 particles were analyzed.	74
<b>Figure 2.9</b> EDX elemental mapping and atomic % of Au and Ag (A) PRINs (B) SSINs. The scale bar is 20 nm.	75
<b>Figure 2.10</b> Single-particle scattering analysis and ensemble UV-Vis extinction spectra of PRINs and SSINs. Dark-field microscope images of (A) PRINs and (B)	

SSINs and corresponding single-particle scattering spectra of (C) PRINs and (D) SSINs. We acquired scattering spectra with an exposure time of 3 s. (E) Ensemble UV-Vis extinction spectra of as-synthesized PRINs and SSINs solution. (F) The solution extinction spectra from five different batches of SSINs solutions. ....	77
<b>Figure 2.11</b> (A) Solution-based UV-vis spectra of PRINs and SSINs. Solution-based SERS spectra of NPs with (B) 785 nm (6 mW) (C) 514 nm (5 mW), (D) 633 nm (3 mW) laser with and acquisition time of 10 s. All the measurements were performed with 100 pM of particles. ....	78
<b>Figure 2.12</b> Theoretical calculation and SERS enhancement factor (EF) distributions from AFM-correlated Raman spectroscopy-based single-particle analysis. (A) Calculated electric near-field distributions of each nanoparticle with different intragap morphologies. (B) SERS EF distribution at $1098\text{ cm}^{-1}$ of each of 200 individual nanoparticles and EF distribution plot as a percentage in (C) PRINs and (D) SSINs, respectively. The excitation wavelength is 785 nm. ....	80
<b>Figure 2.13</b> SERS intensity for 200 single nanoparticles of (A) PRINs and (B) SSINs. ....	82
<b>Figure 2.14</b> AFM-correlated Raman spectroscopic result and corresponding single-particle SERS analysis. Magnified AFM image of a single (A) PRIN and (B) SSIN. SERS spectra and polarization-resolved plot at $1005\text{ cm}^{-1}$ and $1098\text{ cm}^{-1}$ with respect to a rotation angle ( $\Theta$ ), respectively. ....	83
<b>Figure 2.15</b> Time-dependent SERS signal of a single nanoparticle for hotspot stability test. (A and B) Topographical matching of AFM image (left) and Rayleigh	

scattering image (right) for (A) PRINs and (B) SSINs. The inset shows a magnified AFM image of a nanoparticle. (C and D) Time-dependent Raman profiles of a single nanoparticle. (E and F) SERS spectra of single nanoparticle for 30, 1800, and 3630 s and time-dependent plots of the  $I_{1104(0)}/I_{1104(30)}$  ratio. All the spectra were measured using 785 nm excitation laser at laser power of mV and acquisition time of 30s.....85

**Figure 3.1** Schematic illustration of the alloying-dealloying-based synthetic strategy for Au-Ag Knotted Nano Ball (KNB) particles and Au core-hollow shell (CHS) nanoparticles. ....99

**Figure 3.2** Elemental mapping images of (A) Au-Ag Alloy NP and (B) Au@Ag-Au double shell NP for each element and merged images Au (red), Ag (green). Scale bars are 25 nm. (C-D) TEM images and EDX line scan profiles across the NP : (C) Au-Ag Alloy NP, (D) Au@Ag-Au double shell NP. (E-F) Low magnification TEM images of (E) Au-Ag Alloy NP and (F) Au@Ag-Au double shell NP. The inset shows a ring shaped SAED pattern, indicating there is a polycrystalline structure. ....101

**Figure 3.3** Low magnification EDS of Au-Ag alloy NP and Au@Ag-Au double shell NP. Facile synthesis of both particles were synthesized in a high yield. ..102

**Figure 3.4** (A-B) Time-dependent UV-vis spectra showing (A) the consistent band position of SPR absorption in the growth solution of Au-Ag alloy NP and (B) a significant blue shift with time in the solution of Au@Ag-Au double shell NP. The kinetic measurement by tracking the extinction at maximum wavelengths of gold and silver of (C) Au-Ag alloy NP and (D) Au@Ag-Au double shell NP. (E)

Schematic illustration of the possible growth processes with kinetic control growth. ....	106
<b>Figure 3.5</b> Au-Ag co-reduction in low pH condition. (A) TEM images of Au and Ag precursor co-reduction on the 10 nm Au seed. (B) Time-dependent UV-vis spectra in 1 min interval showing a significant blue shift with time in the solution. Insets represent contour plots of the changes in the UV vis extinction spectra with increasing irradiation time. (C) Plotting of Maximum extinction peak with time-dependent growth of Au or Ag on the 10 nm core Au nanoparticle. ....	107
<b>Figure 3.6</b> Syntheses and characterization of KNB and CHS. The TEM image and EDX elemental mapping images of the synthesized (A) CHS, (B) KNB showing a high-yield synthesis of the targeted nanostructures. (C-D) The HR-TEM images and SAED pattern of the ligaments of CHS and KNB (E) (F) TEM and HAADF STEM images of cross section of the KNB obtained by cutting the nanoparticle by using a focused ion beam (FIB). (G) A stepped surface is shown at the surface of the shell and intensity profile obtained from the dotted arrow region, indicates that the shell surface has stepped surface defect sites. ....	109
<b>Figure 3.7</b> Changes in structure and optical properties of KNB with dealloying reaction. (A) Structural and Ag/Au atomic ratio changes in KNB with increase in amount of Fe(NO <sub>3</sub> ) <sub>3</sub> added. (B) Interior-nanogap-formation-dependent UV-vis spectra of KNB. (C) Particle size distribution of nanoparticle before and after dealloying. ....	110
<b>Figure 3.8</b> A tilt series of TEM images of an individual KNB for tomography	

reconstruction. TEM images were collected with the tilt angles of $-30^\circ$ , $-15^\circ$ , $0^\circ$ , $15^\circ$ , $30^\circ$ . .....	112
<b>Figure 3.9</b> KNB size and composition ratio controllable. The TEM image of the synthesized KNB size and composition control 50 nm to 100 nm and 20 at % to 60 at % . .....	113
<b>Figure 3.10</b> Cyclic voltammetry at various electrochemical set-up. Cyclic voltammograms of KNB and blank glassy carbon in deoxygenated solutions containing 0.5 M KOH with and without 1 M $C_2H_5OH$ . .....	115
<b>Figure 3.11</b> CV curves performed in 0.5 M $H_2SO_4$ . (A) CV curves in 0.5 M KOH electrolyte solutions containing 1 M ethanol. (B) All CV was measured at a potential sweep rate of 50 mV/s. The currents were normalized against the mass loaded on each electrode. ....	117
<b>Figure 3.12</b> (A) The SEM and TEM images of the synthesized (A) KNB 60, (B) KNB 40 and (C) KNB 20. (D) CV curves of ANP 40, KNB 60, KNB 40 and KNB 20 in 0.5 M $H_2SO_4$ and (E) in 0.5 M KOH electrolyte solutions containing 1 M ethanol at a potential sweep rate of 50 mV/s . (F) Electrochemically Active Surface Area (ECSA), (G) Mass activities and (H) specific activities. ....	119
<b>Figure 3.13</b> (A) Chromoamperometric results of EOR at 0.28 V on ANP 40, KNB 60, KNB 40 and KNB 20 in 0.5 M KOH + 1.0 M ethanol solution. (B) CV curves of KNB 40 with a scan rate of 5, 10, 20, 30, 40, 50 mV/s in 0.5 M KOH and 1.0 M ethanol. (C) The linear relationship between the forward peak current and square root of scan rate ( $v^{1/2}$ ) . .....	121
<b>Figure 3.14</b> Underpotential deposition of lead (pb-UPD) of (A) KNB 60, (B) KNB 40,	

(C) KNB 20 and (D) the percentages of different facets in Au-Ag alloy 40 and KNB 40. Pb-UPD in 0.1 M NaOH + 1 mM Pb(NO<sub>3</sub>)<sub>2</sub>. Scan rate: 50 mV/s.

.....123

**Figure 3.15** Underpotential deposition of lead (pb-UPD) of (A) KNB 60, (B) KNB 40

(C) KNB 20 in 0.1 M NaOH + 1 mM Pb(NO<sub>3</sub>)<sub>2</sub>. Scan rate: 50 mV/s. 126

## List of Tables

**Table 1.1** Comparison of the activities of various Au catalyst for EOR. ....127

## **Citations to Previously Published Works**

Chapter 1 has appeared in the following paper

“Synthesis, Assembly, Optical Properties, and Sensing Applications of Plasmonic Gap Nanostructures” J. -M. Kim<sup>†</sup>, C. Lee<sup>†</sup>, Y. Lee<sup>†</sup>, J. Lee, S. -J. Park, S. Park, and J. -M. Nam, *Advanced Materials*, 2006966, (2021).

<sup>†</sup> represents equal contribution.

## **Chapter 1.**

# **Highly Controlled Noble Metal Nanostructures Synthesis and Their Applications**

## 1.1 Introduction

With the development of advanced nanotechnology, significant progress has been made in fabricating various metal nanoparticles through chemical synthetic methods. Especially, the colloidal synthesis approach has been adopted as a fundamental and practical study due to its simple preparation and large scale-up capability for high-quality nanoparticles.<sup>[1]</sup> In addition, the controllability of metal nanoparticles with distinct shapes and sizes by selecting different reducing agents, surfactants, additives, and various synthetic conditions in wet chemistry, enables the production of nanoparticles with desired physicochemical properties.<sup>[2]</sup> For further application, the flexibility in modifying the surface of as-prepared colloidal nanoparticles by specific functionality ligands makes this method more attractive.<sup>[3]</sup> The most representative examples are Au nanospheres,<sup>[4]</sup> nanocubes,<sup>[5]</sup> nano triangles,<sup>[6]</sup> and nanorods,<sup>[7]</sup> and they are typically chosen due to their high uniformity and precision. These properties play a critical role in efficiency improvements in several applications, including catalysis<sup>[8]</sup> and surface-enhanced Raman spectroscopy (SERS)<sup>[9]</sup>. Hence, understanding the principles for synthesizing nanoparticles of various shapes and sizes and efforts to achieve high uniformity and yield are essential to developing insight into factors influencing metal nanoparticle optical and catalytic applications. Here, we introduce promising metal nanostructures and synthetic methods for optical and catalytic applications and present optimal structures by understanding the factors influencing their properties.

## **1.2 Plasmonic Intragap Nanostructure Synthesis and Their Optical Study**

### **1.2.1 Plasmonic Nanogap Structure Synthesis**

Plasmonic nanostructures exhibit localized surface plasmon resonance (LSPR), which induces strong enhancement and confinement of resonant incident light on the surface of the subwavelength-scale nanostructure.<sup>[9]</sup> Major progresses have been made in the synthesis and fabrication methods of plasmonic nanostructures with various sizes, shapes, and compositions.<sup>[1,2]</sup> Plasmonic nanostructures can be formed from simple nanoparticles and thin metal films<sup>[10]</sup> to more functional or complex structures such as plasmonic mode-displaying nanopatterns,<sup>[11]</sup> nanoparticles with diverse optical characteristics, and sharp-tip structures with a highly focused field at the end of the tip.<sup>[12]</sup> In particular, plasmonic gap nanostructures (PGNs) are among the most promising materials for diverse applications with highly localized field and amplified optical signals in the gap including sensing, spectroscopy, optics, biomedicine, electronics, and energy applications.<sup>[13–16]</sup> The development of bottom-up synthetic methods enabled the access to numerous nanogap structures with diverse gap sizes, morphologies, and compositions.<sup>[17]</sup> The highly localized electric field inside the plasmonic nanogap and the appearance of plasmonic coupling in closely neighboring structures have been studied, leading to the discovery of interesting optical phenomena and advances in sensing such as ultrasensitive spectroscopy, single-molecule sensing methods, and in situ detection techniques.<sup>[18,19]</sup> As small changes in the distance, morphology, and composition of the

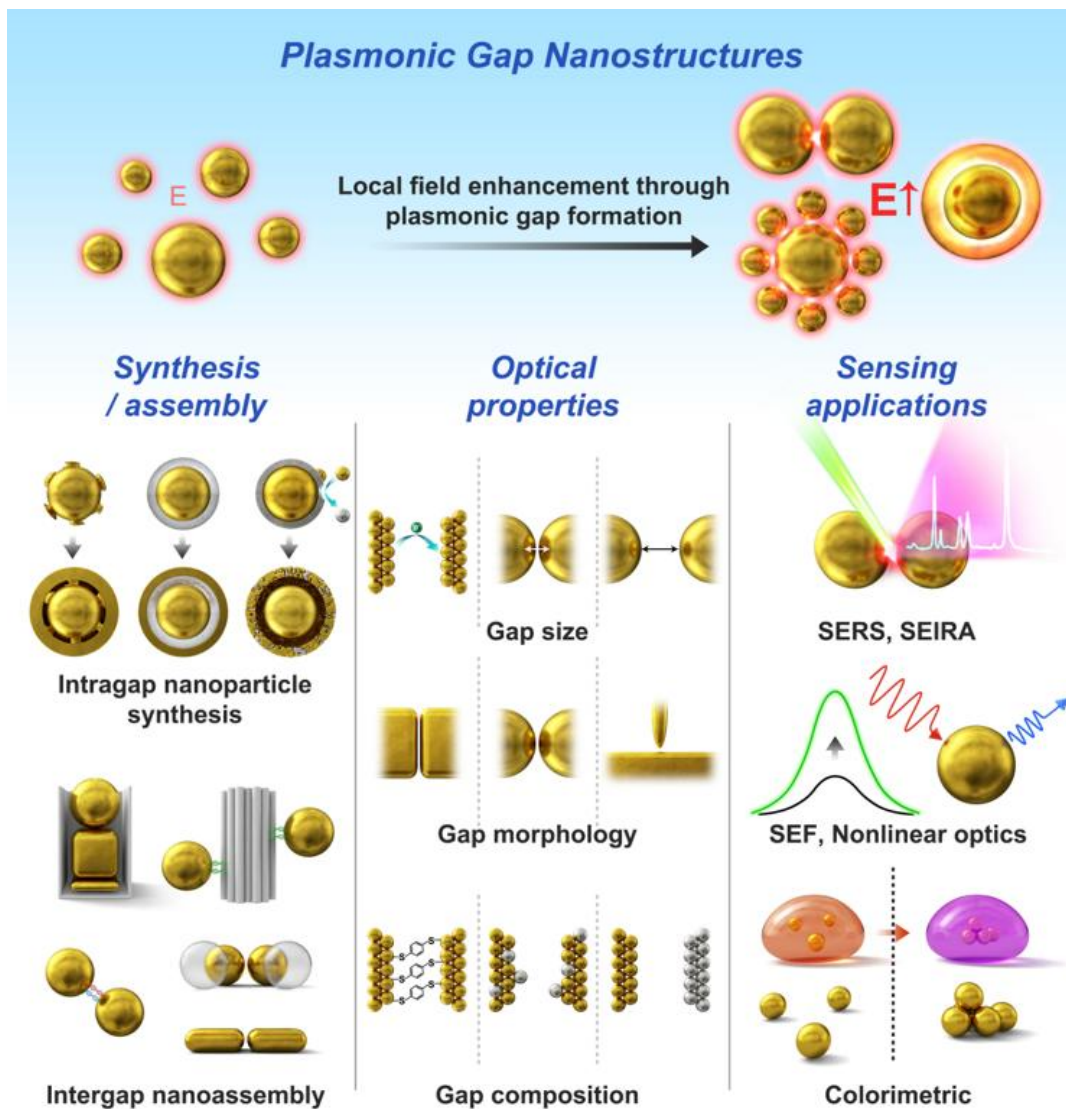


**Figure 1.1 Plasmonic gap nanostructures with their optical properties and sensing applications.**<sup>[17]</sup>

nanogap lead to significant variations in the optical responses, the highly precise, controllable, and high-yielding preparation of PGNs is important to achieve reproducible and reliable results (Figure 1.1.).

The reproducible and precise production of plasmonic nanogaps is critical for obtaining reliable SERS signals since the spectral features of the plasmon coupling are highly sensitive to the sub-nanometer distance and/or shape of the nanogap.<sup>[20]</sup> However, the accurate, scalable, and reproducible synthesis of PGNs remains challenging, particularly over a large number of particles. Hence, insights into previously designed and synthesized gap nanostructures and their optical properties aid the design of nanogap systems for practical applications. In this section, we will describe and discuss various synthetic and assembly strategies that have been developed in precisely forming PGNs over the past decades.

### *Synthesis of Plasmonic Intragap Nanostructures*

Plasmonic intragap NPs are structures with a nanometer-sized internal spacing within a single NP. These uniformly sized intragap NPs not only show strong optical properties and little particle-by-particle signal variations but also provide the stability of the electric field distribution from unwanted interference effects in the surrounding environment due to the shell outlayer.<sup>[21]</sup> The reliable optical outputs generated by these rigid, uniform intragaps are advantageous in ensuring reproducible and quantitative SERS signals, especially for biomedical applications including and biosensing and

imaging.<sup>[22,23]</sup> Despite these advantages, there are still synthetic challenges, including the scale-up issue, to obtain an ideal nanogap inside a particle with excellent and controllable optical performance for practical applications. The most commonly studied intragap nanostructures are core–gap–shell structures, in which a complete shell surrounds a core particle with a nanosized internal gap. The synthesis of core–gap–shell structures involves three stages: preparation of the nanocore, modification of the core surface by gap-forming functional ligands, and shell formation. As the modification of the NP core is strongly influenced by metal surface chemistry and the functional groups and charges of the surface ligands<sup>[24]</sup>, the affinity between core and ligands should be carefully considered. The proper selection and control of the spacer ligands that mediate the gap formation and gap size control are the key factor in the intragap formation chemistry. In general, to generate intragaps, ligands must prevent the formation of a shell that covers the core without an internal gap. Excessively dense coverage of ligands on the particle surface may also interfere with the shell formation around the core. As such, most composite environments affect each other during surface modification, gap, and shell formation. Thus, the formation of an intragap requires a highly precise synthetic strategy with a controlled chemistry. Three different models are mainly used to describe the growth of new metal layers on metal seeds, namely the Frank–van der Merwe (FM), Stranski–Krastanov (SK), and Volmer–Weber (VW) modes (Figure 1.2.).<sup>[25]</sup> These growth models are based on the difference in overall process energy consisting of surface energy (solid/solution interface energy) for each core and shell, strain energy that can be

caused by lattice mismatch between core and shell, and interfacial energy.<sup>[32]</sup> When the metal core surface is capped by weak surfactants, the interfacial energy becomes small and no lattice mismatch between core and shell, leading the secondary metal to predominantly grow epitaxially on the core without a gap (FM mode, Figure 1.2.A). In contrast, when the metal core surface is stabilized by functional molecules with strong bonding, the surface energy of the core becomes lower while interface energy and strain energy become important. Therefore, the secondary metal is not favored to grow epitaxially. Thus, growth initiates from a point of the core at specific sites with high surface energy, leading to island growth (VW mode, Figure 1.2.C). In the VW mode, the nucleation sites become “nanobridge”-like structures which connect cores and shells and subsequently determine the shape of gaps. Finally, the other growth mode is a combination of two preceding modes (SK mode, Figure 1.2.B). Hence, in the synthesis of the intragap in core–shell structures (particularly for the case with Au core and Au shell), it is essential to consider overall excess energy while noting that nucleation sites are very difficult to be formed on the core if the surface ligands are too densely modified. The strategies for the core–gap–shell (CGS)-type intragap structure synthesis can be classified depending on the growth mode of the second metal layer as follows: 1) intragap formation via nucleation on the core, 2) intragap formation via metal shell growth on the spacer ligands, and 3) intragap formation via sacrificial metal layer (Figure 1.3.). Core surface modification is often required to ensure the formation of a nanogap between the core and shell. Surface modification is feasible by materials that act as

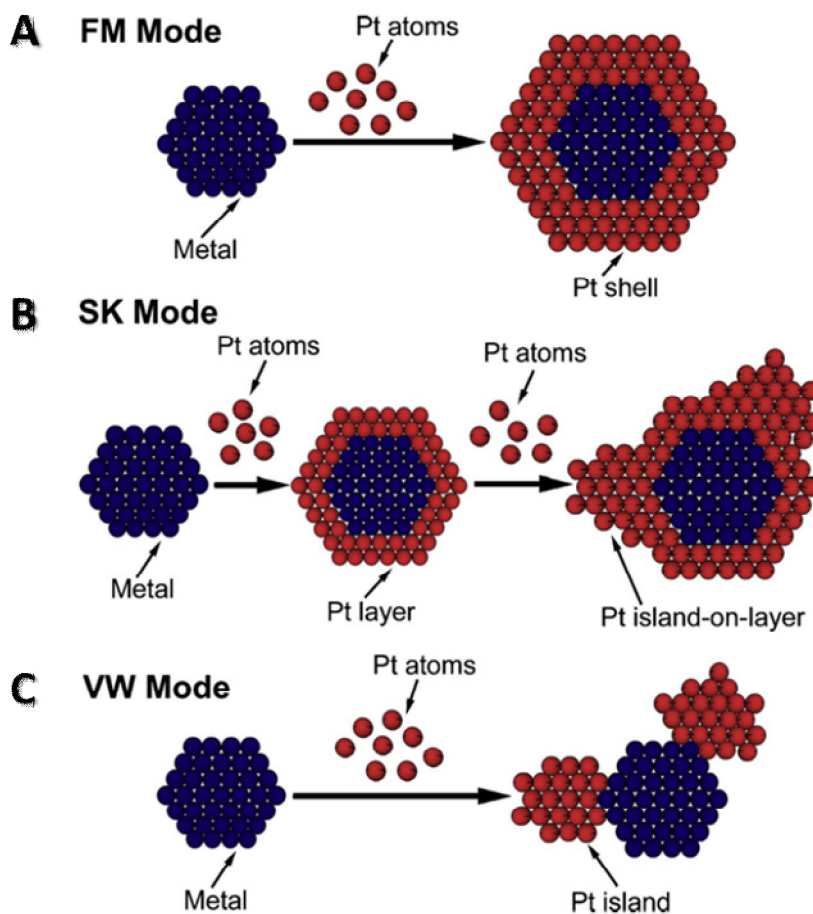


**Figure 1.2 Schematic illustration of three different types of growth modes.** (A) Depositing metal preferably deposit onto the core metal particles, epitaxially in a layer-by-layer fashion. Frank-van der Merwe (FM) mode. (B) Depositing metal grow on the high energy sites of substrate metal particles and forms island in order to minimize strain energy. Volmer-Weber (VW) mode. (C) Depositing metal and core metal particles has relatively large lattice mismatch occurs Stranski-Krastanov (SK) mode.<sup>[25]</sup>

surface coverage ligands and/or analytes on the metal core and usually, these bind by strong S-Au bond with the Au core. Ligands such as thiolated DNA<sup>[21,23,26-30]</sup> and aromatic thiols<sup>[31-38]</sup> are most commonly used, as they increase the interfacial energy, effectively protect the core, and allow the nucleation for second shell growth on specific exposed surfaces (VW mode). Using a thiolated DNA strand as an intragap formation mediator, an Au-nanobridged nanogap particle (AuNNP) with a gap of  $\approx 1$  nm was first synthesized in a remarkably high yield ( $\approx 95\%$ , Figure 1.3.A).<sup>[21]</sup> The 1-nm-thick thiolated single DNA strand (thiol-ssDNA) can bind to AuNP surface and control the formation of the internal gap—the thiolated DNA strands effectively protect the Au core and play a key role in the gap formation during the growth of the Au shell. During the formation of the internal nanogap and Au shell on a DNA-modified Au core, within the first few seconds, nucleations occur on the part of the Au core surface where DNA bases did not bind, and the budding Au nanostructures are connected and smoothed to form the Au shell. In the formation of the intragap, the nucleation sites are grown to form the nanobridges that connect the core with the shell, and different numbers and sizes of Au nanobridges are formed based on the sequence of thiolated DNA bases [polyadenine (poly(A)), polythymine (poly(T)), polyguanine (poly(G)), and polycytosine (poly(C))] and the density of DNA grafting (Figure 1.3.B).<sup>[26,28]</sup> The results show that the number of intragaps and the gap size and shape can be controlled by regulating the interfacial energy with different DNA sequences and densities. A recent report regarding cyclodextrin (CD)-based intranogap particles (CIPs) shows creation of a narrow and

uniform  $\approx 1$  nm gap inside a plasmonic particle by nucleation on the CD-modified core particle surface (Figure 1.3.C).<sup>[39]</sup> It was found that CDs play a key role in the formation of intragap, and the number of modified CDs per each core affects Au shell growth and gap formation and morphology. Densely modified nanometer-sized macrocyclic oligosaccharides (CD in this case) on the Au core induce a small number of budding Au nanostructures and leads to the incomplete shell formation. It was observed that less densely modified CDs allow more Au bridge structures while CDs without modification lead to no gap formation inside the particles. The Au cores with optimally modified CDs resulted in the formation of clear and uniform intragaps with >97% synthetic yield. Aromatic thiols tend to form a self-assembled monolayer through stable Au-S coupling that insulates the Au surface.<sup>[40]</sup> Especially, the use of 1,4-benzenedithiol (1,4-BDT), which acts both as excellent core protector and spectroscopic analyte, for creating intragaps has been extensively studied (Figure 1.3.D).<sup>[32–38]</sup> Both ends of the 1,4-BDT molecules covalently bind to the core and the shell surface via Au-S bonds, and depending on the orientation of the molecules and the formation of multilayers, the intragap varies from 0.7 to 2 nm.<sup>[34,38]</sup> After surface modification of the Au core with 1,4-BDT, nucleation begins at an early stage of Au shell formation. The Au nuclei gradually grow outward, forming a budding structure which becomes the Au bridge between the core and the shell and ultimately encloses the Au core. The dielectric materials and polymers that can modify metal cores to increase the interface energy are good spacer candidates to form gaps inside metal NPs.<sup>[38,41–43]</sup> Unlike DNA and small molecules, the

materials that form tightly blocking spacers or thick layers highly increase interfacial energy, rendering nucleation on the core surface often energetically unfavorable during shell formation. In such cases, the nucleation energy barrier can be reduced by providing artificial nucleation sites or introducing functional groups for metallization on the capping ligands. The metal clusters formed on the functional groups of the ligands provide energetically unstable sites in which metal nucleation occurs, and a shell of composite is formed upon their growth. The Stöber process enables the formation of a uniform SiO<sub>2</sub> layer on the Au core, and the thickness of the shell can be adjusted, providing a spacer between Au core and shell.<sup>[41]</sup> This thick, dense shell layer is favorable to form intragap, but prevents nucleation on the Au core surface due to the large interfacial energy. Therefore, it is necessary to provide artificial nucleation sites by attaching small Au colloids ( $\approx 2$  nm) to the silane-functionalized Au/SiO<sub>2</sub> NPs. Subsequently, a complete outer Au layer is formed by reduction of Au<sup>3+</sup> from a plating solution. Such particles consisting of a Au core and a dielectric layer (SiO<sub>2</sub>) covered by an outer Au shell are known as nanomategyoshkas (Figure 1.3.E).<sup>[38,41,43]</sup> Depending on the thickness of the SiO<sub>2</sub> layer, the size of the intragap can be adjusted in the range of 10–100 nm. Using polydopamine (PDA) as a nanoscale spacer that can universally adhere to various colloidal substrates, the PGNs with a desired intragap size are recently reported (Figure 1.3.F).<sup>[44]</sup> PDA can be deposited on an Au core by consecutive oxidation, intramolecular cyclization, and oligomerization/self-assembly under alkaline conditions, forming a highly crosslinked, rigid PDA shell with a precisely controlled thickness in the

range of 2–13 nm. Quantitative molecular fixation into the nanogap was possible by linking PDA functional groups, such as quinones, with the thiol or amine groups of Raman-active molecules by Michael addition and/or Schiff base reaction. Furthermore, the catechol unit of PDA also functions as a metallization site, inducing the localized reduction of metal precursors. Upon addition of  $\text{KAuCl}_4$  and  $\text{NH}_2\text{OH}$ ,  $[\text{AuCl}_4]^-$  ions are reduced by the PDA's catechol groups initiating metallization and forming a Au shell on the surface of the PDA layer as the amount of Au precursor increases. The intragap size of the particle corresponds to the thickness of the PDA shell (2–13 nm). Upon repeated cycles of PDA coating and metallization, two or three plasmonic multi-nanogaps were obtained. Thus far, the presented methods for the preparation of intragap particles require interlayer ligands to form the plasmonic intragap during a secondary growth phase. In such cases, the interlayer material selection requires a profound knowledge of the system, the interlayer formation/optimization step needs to be further added, and one should take the growth conditions of the shells into consideration. Another strategy to form an intragap involves the use of a sacrificial metal layer. Recently, dealloyed intranagap particles (DIPs) with an intragap of  $\approx 2$  nm were prepared by the highly controllable, facile selective- interdiffusive dealloying technique in  $\approx 95\%$  yield without the requirement of an interlayer (Figure 1.3.G).<sup>[22]</sup> During the poly(vinylpyrrolidone) (PVP)-mediated Ag and Au coreduction in Au NPs, the growth of the Ag shells can be preferential and faster than that of the Au layers due to the strong affinity between Ag and the pyrrolidone groups of PVP, leading to Au/Au–Ag core/alloy shell NPs.

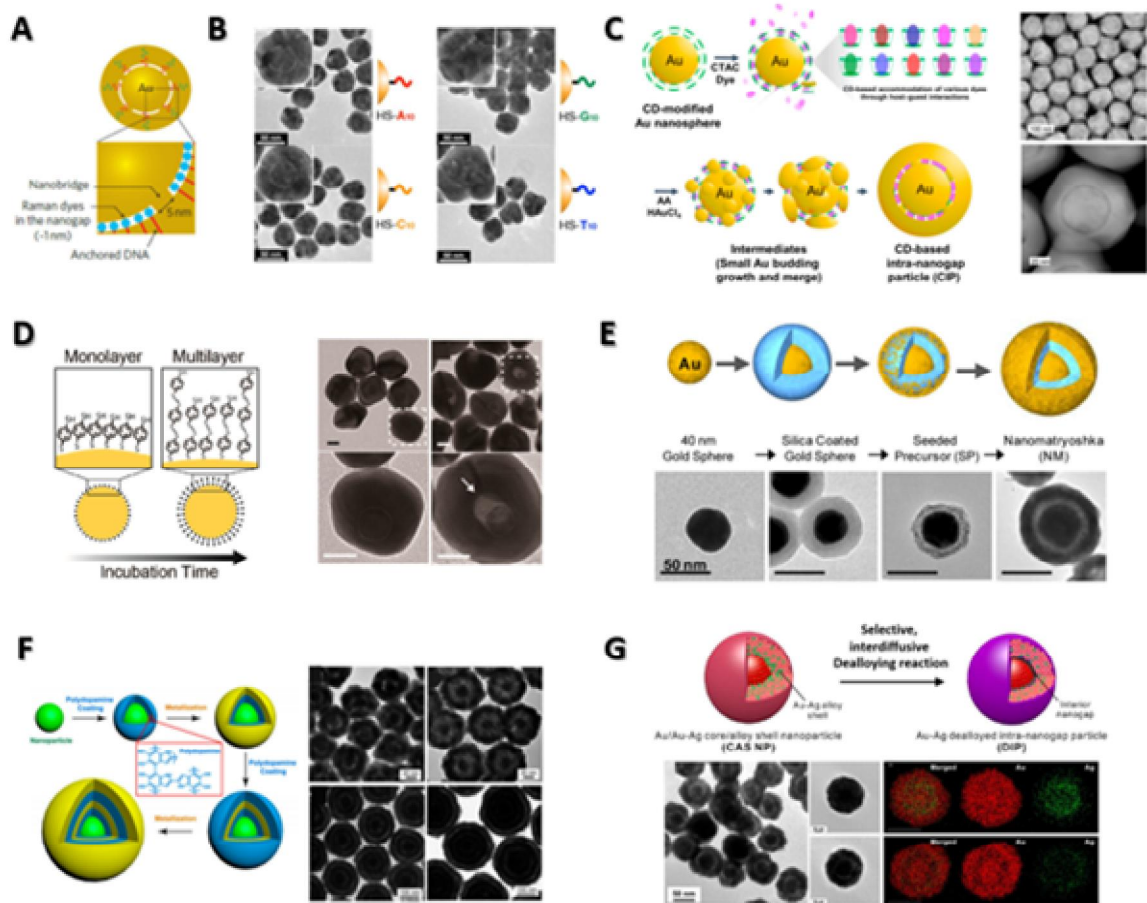


**Figure 1.3 Intragap nanoparticle formation strategies.** (A) Single-strand thiolated-DNA-based intragap formation in AuNNPs.<sup>[21]</sup> (B) Programmable gap morphology by varying DNA sequences.<sup>[26]</sup> (C) Cyclodextrin-based intranagap particles (CIP) capable of accommodating 10 different Raman dyes.<sup>[39]</sup> (D) Verified intragap size via different surface density of 1,4-BDT of GERT.<sup>[34]</sup> (E) Silica dielectric intragap of nanomatryoshilka.<sup>[42]</sup> (F) Polydopamine based intragap formation and multishell plasmonic nanogapped particles via metallization.<sup>[44]</sup> (G) Selective, interdiffusive dealloying (SID) based formation of dealloyed intragap particles.<sup>[22]</sup>

Subsequent selective Ag-etching with  $\text{Fe}(\text{NO}_3)_3$  delivers an intragap of  $\approx 2$  nm. As the dealloying reaction progresses, the outmost Ag atoms of the intermediate Ag layer are dissolved first, generating vacancies. These vacancies diffuse inward and accumulate near the Au core while the Au metal atoms diffuse outward and interconnect to form a dense shell, resulting in the formation of a nanogap due to the nanometer-scale Kirkendall effect.

### **1.2.2 Optical Study of Plasmonic Nanogap Structures**

Plasmonic nanoparticles that exhibit subwavelength scale optical and confine electric field at the metal/dielectric interface have been adopted for plasmon-enhanced spectroscopy applications such as SERS, metal enhanced fluorescence, photoluminescence, surface-enhanced IR absorption, etc. Considering the size, shape, and morphology dependence of LSPR, which enables precise controlling of optical properties of nanoparticles for desirable applications, designing optimal nanostructure for efficient improvement would be significant. Nevertheless, a non-controlled morphology of the metal nanoparticles and aggregation induced by harsh conditions or absence of understanding of the affecting factor leads to poor efficiency and undesirable properties. In particular, SERS is the most distinguished and widely investigated field for the rational design of such plasmonic nanoparticles and significantly improving their performance. The following section attempts to introduce and discuss the factors that comprehensively affect SERS.

## *Surface-Enhanced Raman Scattering*

SERS is based on the strongly enhanced inelastic light scattering from molecules positioned on the surface of a plasmonic metal NP. Molecules located in the hot-spot, the nanogap in which a strongly enhanced electromagnetic field exists due to the plasmon coupling, generate a greatly enhanced SERS signal that can be exploited in ultrasensitive sensing applications.<sup>[20]</sup> SERS provides fingerprint molecular information with narrow vibrational modes and allows multiplexed detection. Moreover, the high photostability of SERS is due to the extremely short lifetime of Raman scattering, which renders it suitable for imaging applications.<sup>[29,45]</sup> In this regard, there is a keen interest in the implementation of rational designs for the development of PGNs for SERS-based sensing applications. Since field enhancements vary significantly depending on the gap size, morphology, and composition, the investigation of the optical properties and development of precise-controlled fabrication methods are necessary to fully understand and exploit these nanostructures. In this section, we review the optical properties of nanogaps with regard to the size, morphology, and composition of the PGNs.

### *Gap Size*

The gap size significantly affects the degree of coupling in the plasmonically coupled nanostructures, which in turn affects the field enhancement within the nanogap as well as the resonance wavelength of the coupled system. The gap size-dependent plasmonic response has been investigated experimentally and theoretically. For the gap sizes larger

than a few nm, the classical electromagnetic theory using Maxwell's equations suitably explains the red-shift of the hybridized plasmon resonance and the local electromagnetic field enhancement as the gap size decreases. However, when the gap size is smaller than a few nm, the near- and far-field properties of the plasmonic nanostructure cannot be described by classical approaches because electron nonlocal and tunneling effects become non-negligible.<sup>[16,46]</sup> For the gaps smaller than a few nm, empirical results start to diverge from classical theoretical predictions due to nonlocal effects. The classical model describes charges mainly with surface charge density, assuming that charges could be fully localized along particle surface with an infinitely small thickness. However, in a real system, charges spread over the distance from the surface, having a volume charge density. Nonlocal hydrodynamic models have been utilized to predict the correct plasmonic resonance and local field enhancement.<sup>[47]</sup> For plasmonic nanostructures with sub-nanometer gaps, electron tunneling phenomena become significant. By the tunneling effect, both blueshift of the bonding plasmon compared to classical prediction and appearance of the charge transfer plasmon in the interparticle gap and disappearance of the gap plasmon mode in the intraparticle gap have been explained. Also, as the plasmonic systems typically require large computational time and cost with fully quantum simulations, semiclassical models such as quantum-corrected model (QCM) were suggested. The QCM method utilizes a virtual bridge with conductivity inside the gap to model electron tunneling, while still using Maxwell's equations.<sup>[38,48]</sup> Although comprehensive theoretical models have been investigated for the quantum regime, the

synthetic design, and fabrication strategy to control the gap sizes within the sub-nanometer range in a reliable and reproducible manner remains challenging. In this regard, plasmonic constructs with tunable gap sizes within the sub-nanometer range were recently synthesized using bottom-up nanoassembly.<sup>[49–53]</sup> Lee et al. synthesized plasmonic Au–Ag core–shell nanodumbbells using hybridization of DNA-modified AuNPs and Ag shell formation.<sup>[52]</sup> The interparticle plasmonic nanogap was controlled at a sub-nanometer level by the Ag shell thickness. The SERS signal from a single nanodumbbell structure with a single Raman dye molecule at the center of the nanogap was acquired by an atomic force microscopy-correlated Raman microscope. Importantly, the SERS signal increased as the gap size decreased, and exhibited a maximum at sub-1 nm nanogap, in good agreement with simulations of the highest electromagnetic enhancement within the gap. These results indicate that a small change in gap size largely affects the SERS intensity and highlight the importance of precision in the synthesis of  $\approx 1$  nm nanogaps for SERS applications. Moreover, DNA origami was used to control the intergap between plasmonic particles. Simonchelli et al. demonstrated that the optothermal-induced shrinking of a DNA origami template enabled control over the gap size between two AuNPs in the range of 1–2 nm.<sup>[51]</sup> In this study, the intensity of the SERS signal from a single molecule that was located in the gap increased with the decrease in the gap size. Cha et al. prepared plasmonic AuNP dimers on a glass slide using the masked desilanization method with adsorption of alkanedithiol linkers between two AuNPs in  $\approx 90\%$  yield.<sup>[50]</sup> The interparticle gap size was tuned at the molecular level

using alkanedithiols of different length. They observed a progressive red-shift of the plasmon mode with the decrease in the gap size. Importantly, as the size reached the sub-nanometer regime, the resonance wavelength underwent a blueshift and broadening. These results represent a deviation from the prediction of the classical electromagnetic theory and indicate that quantum effects play a significant role in that regime. The same research group also demonstrated the continuous gap size tuning using UV-irradiation induced photooxidative desorption of alkanedithiol linkers from the interparticle gaps of the AuNP dimers.<sup>[54]</sup> The gap size was varied depending on the irradiation time, enabling the investigation of the corresponding plasmonic properties (Figure 1.4.A). The irradiation time-dependent extinction spectrum of the dimers exhibited a transition from the classical over the nonlocal and quantum regimes and finally reached the touching regime. This approach is a useful tool for the exploration of the optical properties of plasmon coupling depending on the gap size and the fabrication of AuNP dimers with a desired gap distance. However, the reproducibility of the method and efficiency of fine-tuning, especially in the quantum regime, should be demonstrated and improved. In addition, the possibility of configuration changes of the alkanedithiols due to compressive vdW forces was not considered. An attractive plasmonic nanostructure, NPoM, is a robust nanogap platform that has been extensively studied regarding various optical phenomena due to its straightforward fabrication and strong field enhancement in the nanogap, which is derived from plasmonic coupling between the NP and its image charges on the metal film.<sup>[55]</sup> Furthermore, Mertens et al. introduced graphene as a

spacer between the AuNPs and an Au film to create stable and tunable sub-nanometer gaps down to 0.34 nm, the thickness of a single graphene layer.<sup>[56]</sup> The number of graphene layers determined the gap size. Importantly, a spectral doublet of the coupled plasmon resonance, which originated from the coupling between charge-transfer and gap plasmons, was observed when a single layer of graphene was used as the spacer. This indicated that the quantum tunneling regime was achieved using a single layer of graphene, in the angstrom-scale gap which exists between the nontouching and touching regimes. Recently, bis-phthalocyanine complexes of different rare-earth metals were employed as a plasmonic spacer in NPoM constructs. These sandwich complexes were capable of unprecedented and reproducible subangstrom control over the gap size in the range of 0.39–0.41 nm depending on the metal center (Figure 1.4.B).<sup>[53]</sup> The anomalously large spectral shift that was observed with varying central lanthanide ions cannot be described by any theoretical model, implying that subtle changes in the chemical environment are non-negligible, and improved theory and new treatments must be developed, especially for the sub-nanometer scale regime. While intergap plasmonic nanostructures have been extensively investigated regarding their gap size-dependent optical properties, intragap structures composed of core, gap, and shell are also promising nanostructures for various applications due to the potential accommodation of Raman-active or fluorescent molecules in the nanogaps. For example, Kulkarni et al. studied plasmonic intragap structures with gaps smaller than 0.5 nm and reported that the absorption cross section and local field enhancement calculated by the time-dependent

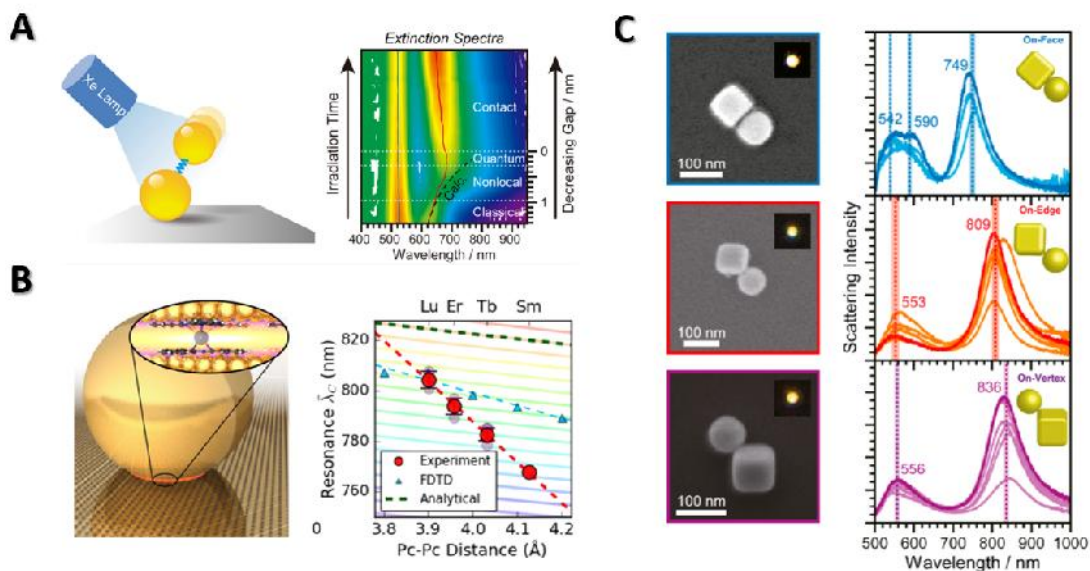


**Figure 1.41 Optical properties of nanogap particles.** (A) Wavelength shift of the plamone resonance depending on the gap size, which is controlled by UV-irradiation.<sup>[54]</sup> (B) Subangstrom gap size control in NPoM constructs via central lanthanide ion and their corresponding resonance wavelengths.<sup>[53]</sup> (C) Wavelength shift of the plasmon resonance of Au nanocube-Au nanosphere dimers with different gap morphology.<sup>[57]</sup>

density functional theory significantly deviates from the classical predictions.<sup>[58]</sup> Owing to these small gap sizes, the potential barrier between core and shell decreased, thus facilitating electron tunneling within the gap. Furthermore, Lin et al. synthesized plasmonic intragap particles with 0.72 nm nanogaps using a self-assembled monolayer of 1,4-BDT molecules on the cores.<sup>[38]</sup> The electron transport through the sub-nanometer gap occurred via molecular junctions, resulting in disappearance of the gap plasmon mode. These results differ from the classical theory predictions and indicate the significant effect of chemicals in the narrow gap.

### *Gap Morphology*

In PGNs, the gap size is only one among the many factors that enable tuning of the plasmon response. Changes in the gap morphology strongly influence the plasmonic behavior, such as far- and near-field responses, as they affect the resonance wavelength and local field enhancement.<sup>[59]</sup> In particular, even small morphology changes induce significantly different plasmonic responses because of the strong interactions with light.<sup>[60]</sup> Esteban et al. studied the influence of the gap morphology of plasmonic dimers (round or flat gap terminations) on the far- and near-field response using electromagnetic calculations and quantum corrected models.<sup>[61]</sup> The conventional round terminated gap led to a red-shift of the plasmon mode as the gap size decreased and larger field enhancement than that of its flat counterpart. Interestingly, the flat terminated gap

exhibited two sets of plasmon modes, a strongly radiative one and a weakly radiative one which was strongly confined to the gap. In addition, the onset distance of electron tunneling was larger for the flat terminated gap than for the round one. These results indicate that the gap morphology largely affects both the near- and the far-field properties. Hence, the choice of the gap morphology is important in exploiting the appropriate plasmonic response for a given application. Kim et al. used the bottom-up nanoassembly approach combined with the masked desilanization method to prepare Au nanosphere–Au nanocube dimers.<sup>[57]</sup> Different gap morphologies were obtained depending on the adsorbing position of the sphere with regard to the cube (face, edge, or vertex) (Figure 1.4.C). The energy of the coupled plasmon mode of the dimer was lower as the sphere interacted with the protrusion region of the cube. This result is aligned with the Coulomb's law, in which the interaction energy is proportional to the charge of the particles. As the charge density of the cube significantly differs between face, edge, and vertex, the relative orientation of the nanosphere with regard to the cube is a key factor influencing the plasmon coupling of the dimer. Therefore, the lowest energy of the coupled plasmon mode results from the interaction of the nanosphere with a protrusion region of the cube, such as a vertex where the largest charge density exists. Different gap morphologies of intragap nanostructures can be obtained by tuning DNA sequences modified on core NPs. Oh et al. synthesized Au-NNPs using DNA-modified Au cores on which different DNA sequences were modified.<sup>[26]</sup> Varying binding affinities between DNA bases (A, T, G, C) and Au surface lead to different numbers and sizes of

nanobridges within the intragap. The arc angle (and size) of the intragap determined by the density of nanobridges results in distinct EM-field enhancements. Depending on the arc angle of the intragap, the strongest SERS signals were generated with different excitation wavelengths. These results suggest that the size and number of the nanobridges within an intragap are the key determining factors to fully understand and utilize the optical properties of plasmonic intragap nanostructures with a desired excitation wavelength. Remarkably, not only the nanostructure protrusions, but also atomic protrusions inside the gap alter the plasmon response. Recently, Benz et al. first showed that individual atomic protrusions inside the gap can confine light within  $1 \text{ nm}^3$ , and these so-called “picocavities” are capable of single molecule spectroscopy.<sup>[60]</sup> Such extreme optical confinement generates strong field gradients depending on the relative position of picocavity and molecule, resulting in modified SERS selection rules and selective excitation of specific vibration modes that are typically Raman inactive. For this reason, observation of SERS blinking phenomena in a region other than that of persistent SERS lines indicates the existence of a picocavity containing a single molecule and the appearance and disappearance of picocavities under continuous laser exposure. The atomic-scale diffusion was also suggested to explain the SERS blinking. Picocavities are widespread in PGNs, and can be observed by near-field measurements. However, the instability of the observed picocavities at room temperature is an obstacle to the exploitation of the extreme optical confinement in various light–matter applications. Recent studies focused on demonstrating the existence of picocavities under ambient

conditions using spectral information from SERS measurements.<sup>[62,63]</sup> In NPoM nanocavities, the thiol group of the analyte molecules binds to the lower Au substrate while the other functional groups are oriented outward. In such cases, there are two typical picocavities with an atomic protrusion on the surface of the Au substrate or AuNP. These different atomic configurations generate different field gradients across a single molecule, leading to distinct sets of SERS peaks, indicating that subtle changes in the atomic environment around a molecule significantly affect its spectral features (Figure 1.5.A).<sup>[62]</sup> However, the control over the site position of the atomic protrusion relative to a single molecule inside a nanogap and the fabrication of robust picocavities remain formidable challenges. If the atomic position and configuration in the nanogap could be precisely modulated, the sub-nanometer hot-spots could enable the development of various unprecedented plasmon-enhanced applications such as single molecule photochemistry and real-space visualization of molecular vibration modes.<sup>[63]</sup>

### *Gap Composition*

The chemical composition in the nanogap also largely affects the plasmon mode and the field enhancement in PGNs. Using electron energy-loss spectroscopy, Tan et al. first showed the generation of the tunneling charge transfer plasmon (tCTP) mode through conductive molecules in the gap.<sup>[65]</sup> Importantly, when the insulating molecules in the nanogap were substituted by conductive ones, a distinct spectral change was observed and tunneling occurred, revealing the tCTP mode even in the 1.3 nm gap. This finding is remarkable for a conventional nanogap system, as

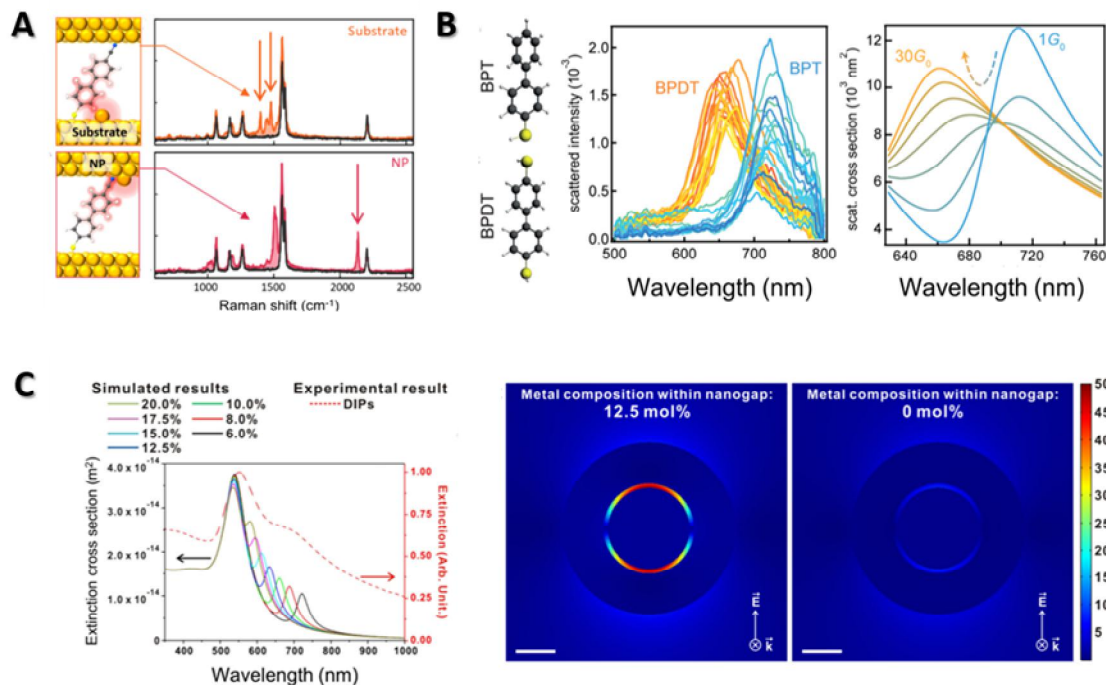


**Figure 1.5 Optical properties of nanogap particles.** (A) Modified Raman selection rules depending on atomic protrusions in the nanogap.<sup>[62]</sup> (B) Wavelength shift of the plasmon resonance in NPoM systems depending on the conductance of the molecules in the nanogap.<sup>[64]</sup> (C) Metal composition-dependent far- and near-field properties of intragap particles.<sup>[22]</sup>

quantum mechanical effects are generally observed in gaps of sub-nanometer size. In addition, the onset tunneling distance can be varied depending on the molecules inside the nanogap. For instance, a relatively large onset distance is expected when using longer conductive molecules. Moreover, far-field scattering spectroscopy can be used to observe the effect of conductive molecules on the plasmon mode.<sup>[60]</sup> Self-assembled molecular monolayers of different conductivities were used as spacers in NPoM constructs. Specifically, biphenyl-4,4'-dithiol (BPDT) and BPT were studied. As BPDT has two thiol groups on opposite sides, it can adsorb on the Au substrate and on the AuNP. As such, the  $\pi$ -orbitals of the phenyl rings form a conduction link across the nanogap. In contrast, the lack of the second thiol group in BPT disrupts conductivity leading to an insulating junction. The scattering spectra of NPoMs containing BPDT or BPT as nanogap spacers were measured. Interestingly, a blueshift of the coupled plasmon resonance was observed for NPoM constructs with the BPDT molecular junction. When mixtures of BPDT and BPT were used, a continuous blueshift was observed with the increase in the BPDT mole fraction. Hence, the blueshift corresponds to the increase in the molecular conductivity in the nanogap, which was confirmed by a numerical simulation (Figure 1.5.B). In addition, the current across the nanogap reduces the local field due to the conductive molecular junction, leading to a decrease in the SERS intensity. Recently, Cui et al. observed similar far- and near-field effects using conductive and insulating molecules in the nanogap of Au nanoplate–Au nanosphere heterodimers.<sup>[66]</sup> They introduced a Si substrate with a high-dielectric-constant to induce

higher-order plasmon mode excitation and Fano resonance. Interestingly, the spectral features of the Fano resonance and higher-order charge transfer plasmon mode were affected by the conductivity of the molecular junctions in the nanogap. Moreover, the local field enhancement in the nanogap region was reduced because of the conductive junction, resulting in a reduction of the SERS intensity. In addition to the molecular junction of the plasmonic nanogap, the metal composition in the nanogap also strongly influences the plasmon responses. Kim et al. showed that the metal composition of an intragap particle influenced the local field enhancement in the gap region and the resonance wavelength of the NP.<sup>[22]</sup> The intragap particles were synthesized by selective, interdiffusive dealloying (SID) reaction of alloyed NPs. Upon dealloying, metal residues might remain in the gap region. Interestingly, the plasmon resonance peak was continuously tuned according to the amount of metal residue due to the change in the effective dielectric function of the nanogap. Importantly, the enhancement of the near-field response in the intragap region was stronger for gaps containing metal residues than for water-filled intragaps, suggesting that metal residues in the intragap are important for field enhancement applications such as SERS (Figure 1.5.C).

## 1.3 Nanoporous Structure Synthesis and Their Catalytic Studies

### 1.3.1 Nanoporous Au Structures Synthesis

Compared to solid and dense nanostructures, nanoporous materials refer to materials with a large number of nanometer-sized pores and significant-high surface area.<sup>[67]</sup> Especially, metal nanoporous materials have recently paid attention to their unusual physical, chemical, and mechanical properties due to their nanopore structures.<sup>[68-70]</sup> Recently, nanoporous metal materials have been widely applied in various fields, and many researchers are developing various methods to synthesize them effectively.<sup>[71]</sup> At present, the preparation methods of NPG mainly include the template or dealloying method. The template method to form nanoporous structures uses anodic aluminum oxide (AAO)<sup>[72]</sup>, porous silica<sup>[73]</sup>, inorganic or copolymer template<sup>[74,75]</sup>, Etc<sup>[76]</sup>. This organic or inorganic porous template fill with metal, and the template is eliminated by annealing or dissolution for the final product. Using AgCl sacrificial nanocrystals is one example of using a template for forming hollow nanoporous gold nanoparticles (Figure 1.6.A).<sup>[74]</sup> This One-step synthetic method uses Au and Ag precursor, hydroquinone reducing agent, and PVP surfactant evolute of Au nanoporous on the AgCl cubic template. By washing with concentrated NH<sub>4</sub>OH, the AgCl sacrificial template can remove and eventually form nanoporous hollow Au. This method has the advantages of free-standing synthesis and is relatively easy to control the particle size (150-1,000 nm) and ligament thickness (21-52 nm). Macroporous nanoparticle films were fabricated on a macroporous substrate by using the pre-ordered polystyrene (PS) crystal templates on the

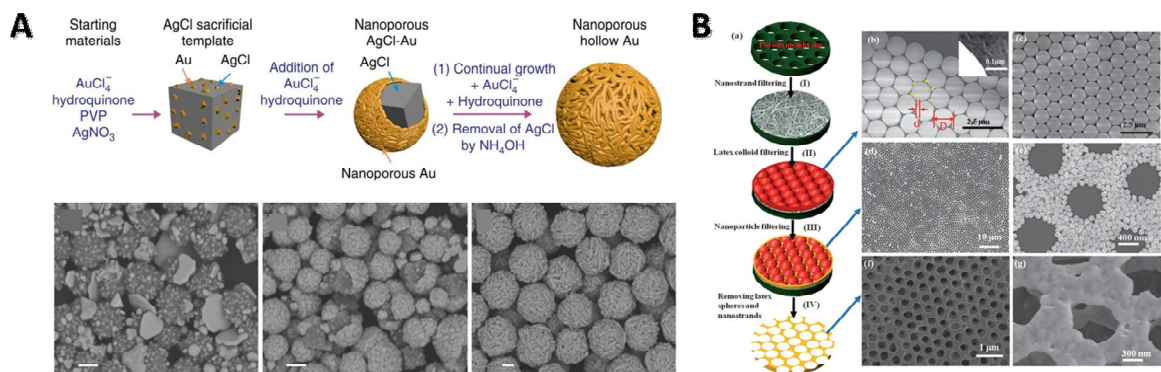


**Figure 1.6 AgCl sacrificial crystal and aligned microporous film-template-based nanoporous Au formation.** (A) Synthesis scheme for nanoporous hollow Au nanoparticles using AuCl as a sacrificial template, and representative SEM image of the corresponding steps.<sup>[74]</sup> (B) Synthetic method and SEM of macroporous Au films by filled with Au nanoparticle on the ordered microporous PS crystal film followed by removing PS templates and copper hydroxide nanostrand layer.<sup>[75]</sup>

ultrathin copper hydroxide nanostrad (CHN) layer by filtration techniques (Figure 1.6.B)<sup>[75]</sup>. The PS sphere could be efficiently ordered in the hexagonally closed-packed (hcp) arrays on the CHN layer. A subsequent curing step enabled the nanoparticle dispersion into the interstitial space of the PS sphere array. Then finally, macroporous nanoparticle films were released from the template by treatment of heating and HCl. However, synthesizing various porous structures requires corresponding porous templates to be newly designed and limits controllability.

#### *Dealloying Reaction for Nanoporous Structure Synthesis*

Dealloying is one of the representative methods for synthesizing nanoporous metal structures derived from a spontaneous corrosion process that selectively removes relatively less noble metal elements from metal alloys.<sup>[77,78]</sup> The dissolved less noble elements form a void within the nanostructure during the dealloying. In contrast, the remaining noble elements build highly curved many ligaments through nucleation and surface diffusion to minimize surface energy. As a result, the intrinsic metal-void bicontinuous structure is formed, consisting of three-dimensionally interconnected ligaments (Figure 1.7.A).<sup>[77]</sup> The working model for nanoporous Au evolution from Au-Ag alloy illustrate in Figure 1.7.B.<sup>[78]</sup> The Dealloying process begins with selectively dissolved Ag atoms (less noble metal) from homogeneous Au-Ag alloy. As dealloying continues, surface diffusion of Au atoms (noble metal) passivates Ag-etched surface sites. This process generates bicontinuous nanoporous with ligaments with Au-rich surfaces

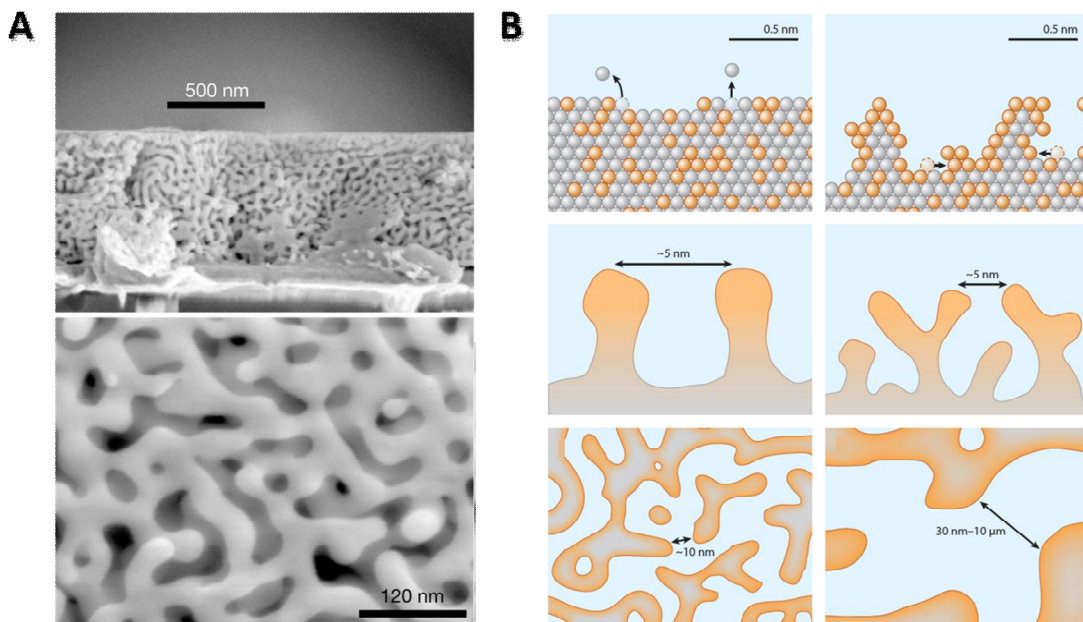


**Figure 1.7 The structure and mechanism of evolution in dealloying of nanoporous Au.**

(A) The cross-section scanning electron micrographs (SEM) of dealloyed nanoporous Au thin film.<sup>[77]</sup> (B) Working model for nanoporous Au evolution from Au-Ag alloy system (Au atom, orange; Ag atom, gray).<sup>[78]</sup> The Dealloying process begins with selectively dissolved Ag atoms (less noble metal) from homogeneous Au-Ag alloy. As dealloying continues, surface diffusion of Au atoms (noble metal) passivates Ag-etched surface sites. This process generates bicontinuous nanoporous with ligaments with Au-rich surfaces and Ag-rich interiors.

and Ag-rich interiors. Dealloying for synthesizing nanoporous metal structures employs alloy materials such as Au-Ag, Ni-Au, Al-Au, Zn-Cu, Al-Cu, Mn-Cu, Ni-Cu, Etc. The morphology (e.g., pore size, ligament thickness) of dealloyed nanoporous structures can be tuned depending on the composition or distribution of metal components in alloy material.<sup>[79]</sup> However, some combination of alloy elements has barrier with the percolation network, pattern-forming instability, or parting limit due to the differences in the alloy phase diagram, lattice constants of components, and the inclination to passivate during dealloying. The most commonly used Au-Ag alloy system exhibits the advantages of a single fcc crystal phase with low lattice mismatch, the so-called solid solution. Although Au-Ag alloy is advantageous for forming solid solutions, the sintering process is unavoidable for fusing two metal components by applying heat below the melting point or pressure to produce an alloy. For this reason, the preparation of nanoporous metal structure mainly includes a template-dealloying-based method for maintaining the structure at high temperatures. As shown in Figure 1.8.A, the nanoporous gold film has been produced by depositing Au and Ag alloys onto support made of a SiO<sub>2</sub>/Si wafer substrate using an alloy target.<sup>[80]</sup> The Au/Ag bi-layer films were deposited on the substrate and annealed at 900°C in Ar for the dewetting process. The dewetting process by annealing induced Au-Ag alloy nanoparticles formation on the substrates and followed by nitric acid treatment to remove the Ag (dealloying). The resulting nanoporous gold nanoparticles on the substrate possess a much higher surface-to-volume ratio than the bulk nanoporous gold samples or nanoparticles. However, the support-

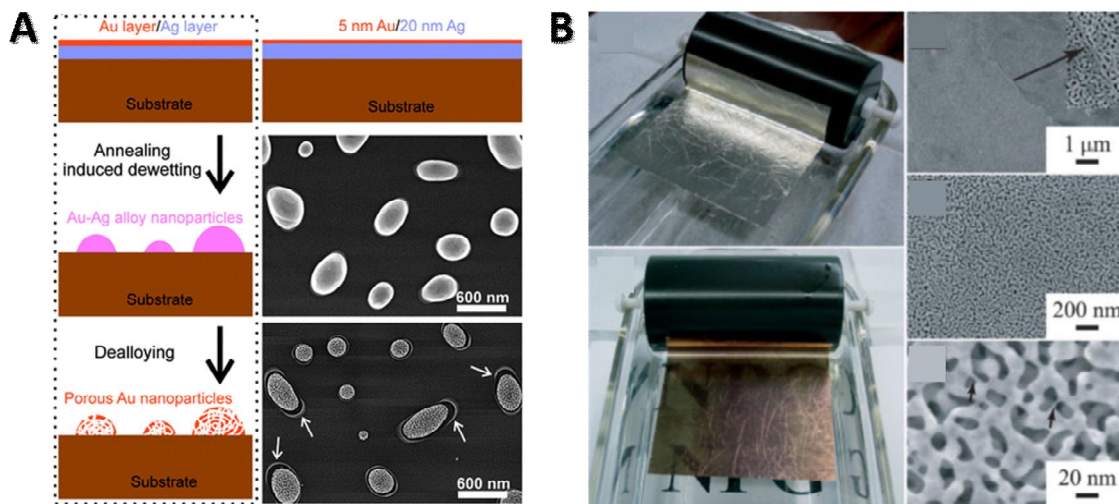


**Figure 1.8 Substrate-based and free-standing synthesis of nanoporous Au.** (A) Schematic formation pathway for substrate-based synthesis of porous Au nanoparticles combining the dewetting process and dealloying and the corresponding SEM images of the contour of the porous Au nanoparticles.<sup>[80]</sup> (B) Optical and SEM images of white-gold leaf before and after dealloying. Chemically dealloying in nitric acid for 15 min results in a free-standing nanoporous gold membrane.<sup>[81]</sup>

based nanoporous gold structure has a limitation in that it cannot be applied to more diverse fields because one side is fixed to the support. Commonly used non-supported nanoporous gold film fabricate by chemical dealloying using 100 nm thickness of Ag-Au alloy leaf, which soak in a  $\text{HNO}_3$  solution for 3h at room temperature (Figure 1.8.B).<sup>[81]</sup> As synthesized, nanoporous Au film was treated with DIW to wash the remaining  $\text{HNO}_3$  and annealed at  $80^\circ\text{C}$  for a uniform and homogeneous nanoporous alloy structure. The general alloying process for dealloying accompanies hush conditions for fully alloyed, such as high-temperature sintering. Therefore, fabricating free-standing colloidal alloy nanoparticles is more challenging for porous nanoparticles than 2D porous film. Recently, free-standing colloidal dealloyed Au porous nanoparticles were synthesized with  $\text{SiO}_2$  shell protection (Figure 1.9.A).<sup>[82]</sup> During the high-temperature annealing process reaching  $950^\circ\text{C}$ , the  $\text{SiO}_2$  shell can form fully alloyed Au-Ag nanoparticles from Au core-Ag shell nanoparticles while protecting their structure from aggregation or collapse. The resulting AuAg alloy@ $\text{SiO}_2$  nanoparticles encased in silica shells were subsequently dealloyed with nitric acid, forming highly porous Au-Ag nanoparticles. One of the most facile and straightforward synthetic strategies to form highly porous Au nanoparticles is the simultaneous reduction of Au and Ag precursors on the Au core for making alloy nanoparticles, followed by dealloying (Figure 1.9.B).<sup>[83]</sup> This method does not need a high-temperature annealing process for forming AuAg alloy but should consider Ag/Au ratio for elemental well-distribution in the shell region. By simply tuning the Ag/Au ratio from 1 to 7, the elemental distribution can be controlled in the shell region due to the

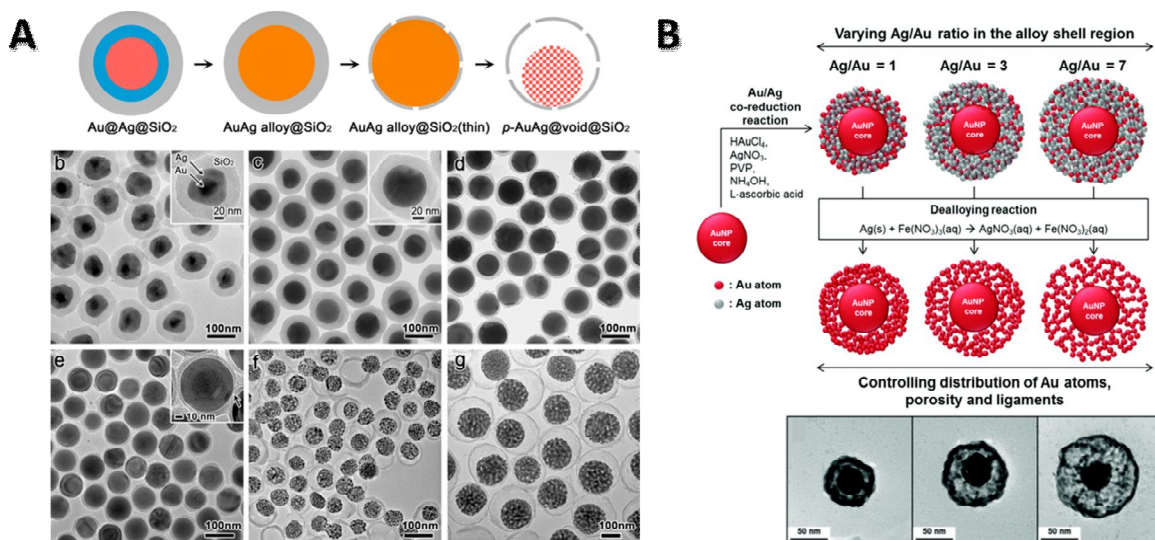


**Figure 1.9 Dealloying-based Au porous nanoparticles synthesis.** (A) Au-Ag alloy was obtained by subjected to high-temperature annealing (950°C) from Au core-Ag shell under silica shell protection. After chemical dealloying, AuAg@void@SiO<sub>2</sub> nanoparticle was fabricated.<sup>[82]</sup> (B) A facile synthetic method for Au core/porous shell nanoparticles by co-reduction of Au and Ag on the nanoparticle core and chemical dealloying.<sup>[83]</sup>

different reduction rates of Au and Ag. This method does not need a high-temperature annealing process, and forming AuAg alloy at room temperature in wet chemistry for 1h. The optimized Ag/Au molar ratio results in an atomic-scale well-mixed alloy shell and following dealloying forms highly porous Au core/porous shell nanoparticles.

### **1.3.2 Electrocatalytic Studies of Nanoporous Au structures**

As various methods for synthesizing nanoporous Au metal have been developed, many studies have reported that the metal-void bicontinuous structure plays an essential role in improving the electrocatalytic performance.<sup>[69,84]</sup> The origins of electrocatalytic activities are comprehended based on their atomic-scale structures of ligaments surface. Moreover, the high surface-to-volume ratio of a nanoporous Au metal can increase the probability of interaction between a molecule of react and the active site of metal, which significantly affects the electrochemical efficiency. In this section, we review the catalytic properties of nanoporous structure with regard to the surface area, specific surface structure, and composition of Au nanoporous.

#### *High surface-to-volume ratio of nanocatalyst*

It is obvious that the nanoporous structures possess an extremely high surface-area-to-volume ratio compared to solid nanostructures, providing a higher chance for catalytic reactions. Moreover, complex 3D bicontinuous structure and large internal surface area enable the supply of high density of active catalytic sites and increase the dwell time of

intermediates. However, Au nanoporous structures with a high surface area can be composed of various pore and ligament sizes, which can serve different functions as catalysts, so it is important to perceive a structure-activity relationship and optimize the structure for a specific reaction. Catalyst with small and many pores increases the electrochemically active area (ECSA) and supplies abundant catalytic sites, while larger pores can improve the molecule transportation into the internal surface of the catalyst and increase reaction probability. Recently, 3D hierarchically porous Au nanostructures were fabricated through the proximity-field nanopatterning and dealloying method (Figure 1.10.A). The porous Au nanostructures were efficiently designed with macroporous networks and interconnected nanopores. Compared to the Au catalyst with no pore (nt-Au) and only nanopores (N-Au) or micropores (M-Au), the catalyst with a hierarchical porous structure (NM-Au) shows efficient mass transport and higher mass activity in the electrocatalytic CO<sub>2</sub> reduction reaction. Studying the mass transport effect within 3D hierarchically porous Au nanostructures reflects the importance of optimal pore size and distribution for efficient electrocatalyst.

#### *Specific surface structures of active sites*

Unlike the bulk metal, the complex 3D structure of Au nanoporous catalyst exhibits remarkable catalytic performance in significant oxidation and hydrogenation reactions.<sup>[85]</sup> Recent studies, through the improvement of understanding of surface chemistry of Au and density functional theory (DFT) calculations, suggest that the

catalytic activity originates from the highly abundant active site, including the undercoordinated atoms on the locally curved ligament surfaces.<sup>[86,87]</sup> The surface atoms can be classified into terraces, step edges, and kink, and their atomic coordination numbers (ACNs) decrease in order, respectively. Figure 1.10.B shows high-resolution transmission electron microscopy (HR-TEM) images of exposed dealloyed Au membranes surfaces.<sup>[88]</sup> Abundant atomic steps and kinks were observed for highly curved surfaces with convex or concave structures.<sup>[89,90]</sup> Among the surface defects, the lower ACNs, such as steps and kinks, provide primary sites for activating molecular oxygen.<sup>[91]</sup> However, recent studies report that the electrocatalytic activity on the undercoordinated Au surface does not always have high catalytic activity. Therefore, it can be further improved by optimizing the atomic scale of surface structures according to the type of reaction and catalyst.<sup>[93–95]</sup> For example, although selective methanol oxidation and CO oxidation reaction require O<sub>2</sub> activation, Au nanoporous catalysts were not necessarily active for CO oxidation.<sup>[96]</sup> In another study, the surface structure of the catalyst for optimal catalytic performances was engineering by using different surfactants during the dealloying electrolyte.<sup>[93]</sup> As prepared, two types of Au nanoporous, which have rich {111} facets and rich {100} facets and step/kink sites, show improvement in catalytic activities toward methanol oxidation reaction and oxygen reduction reaction, respectively. These studies consistently suggest a more complicated fundamental structure-activity relationship that cannot be fully explained independently based on highly-active undercoordinated sites.

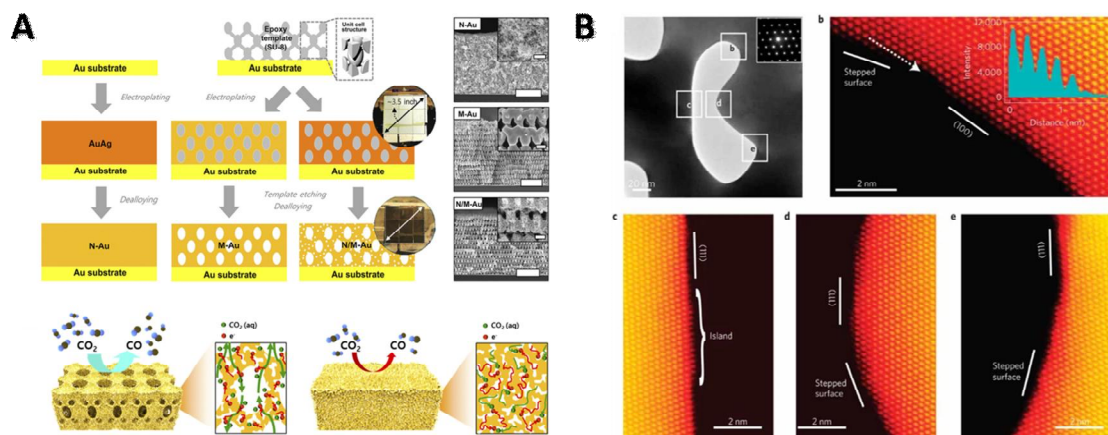


**Figure 1.10** Various porosity and surface atomic structure of Au nanoporous catalyst. (A) Schematic illustration of synthesizing various Au nanoporous structures, and different reaction pathways according to the pore size.<sup>[92]</sup> (B) TEM and HAADF-STEM images of nanopore show (100) surface plane with atomic kinks and (111) surface plane with monoatomic layer island, convex terrace, and concave stepped surface along the edge.<sup>[88]</sup>

### *Composition of nanocatalyst*

It has long been understood that the Au catalyst was active in molecular oxygen on the surface defect, which is composed of the high density of low-coordination sites present on the curved ligaments. However, arising from the rapid progress in mechanism studies, it is now known that the type of metal component constituting the catalyst also affects the electrocatalytic activity in addition to the coordination number.<sup>[97]</sup> Generally, as-prepared Au nanoporous catalysts through the dealloying are dominated by Au, but less-noble elements cannot be completely dissolved and are always inevitably contained. The influence of residual less-noble metal on the activation of molecular oxygen is suggested by recent experiments that increase the binding energy of molecular oxygen on Au surfaces in the presence of residual Ag.<sup>[98]</sup> Particularly, DFT model studies on the Au (321) surface demonstrate that the adsorption energy of molecular oxygen becomes more negative and lowers the activation barrier for O<sub>2</sub> dissociation when Ag atoms substitute Au atoms.<sup>[99,100]</sup> In addition, the residual Ag also plays a critical role in stabilizing the surface active sites, greatly enhancing the durability and activity of electrocatalyst toward the oxidation of four different alcohol fuels.<sup>[101]</sup> The investigation of the high activity of CO oxidation with Au-Cu alloy porous catalyst also claims that the residual Cu promotes the molecular oxygen activation on Au nanoporous surface.<sup>[102]</sup>

## **1.4 Conclusion**

The accurate recognition of the crucial roles of noble metal nanoparticles in intriguing optical and catalytic properties gives us insights and suggests a direction for future work in nanotechnology. As we discussed above, we better understand the design principles of nanoparticles considering the effect factor, and the optical, and catalytic properties can be further developed. Furthermore, detailed studies of metal nanoparticles can produce unique and infinite material properties that can be exploited for the unexplored areas of research. Hence, significant efforts to optimize and overcome challenging issues would enable the reliable use of noble metal nanoparticles in various fields and provide the springboard for the commercialization of these materials, platforms, and methods.

## 1.5 References

- [1] M. Ha, J. H. Kim, M. You, Q. Li, C. Fan, J. M. Nam, *Chem. Rev.* **2019**, *119*, 12208.
- [2] Y. Wang, J. He, C. Liu, W. H. Chong, H. Chen, *Angew. Chemie - Int. Ed.* **2015**, *54*, 2022.
- [3] H. Kang, J. T. Buchman, R. S. Rodriguez, H. L. Ring, J. He, K. C. Bantz, C. L. Haynes, *Chem. Rev.* **2019**, *119*, 664.
- [4] Y. Zheng, X. Zhong, Z. Li, Y. Xia, *Part. Part. Syst. Charact.* **2014**, *31*, 266.
- [5] J. E. Park, Y. Lee, J. M. Nam, *Nano Lett.* **2018**, *18*, 6475.
- [6] L. Chen, F. Ji, Y. Xu, L. He, Y. Mi, F. Bao, B. Sun, X. Zhang, Q. Zhang, *Nano Lett.* **2014**, *14*, 7201.
- [7] L. Vigderman, B. P. Khanal, E. R. Zubarev, *Adv. Mater.* **2012**, *24*, 4811.
- [8] B. Hvolbæk, T. V. W. Janssens, B. S. Clausen, H. Falsig, C. H. Christensen, J. K. Nørskov, *Nano Today* **2007**, *2*, 14.
- [9] K. A. Willets, R. P. Van Duyne, *Annu. Rev. Phys. Chem.* **2007**, *58*, 267.
- [10] S. A. Maier, H. A. Atwater, *J. Appl. Phys.* **2005**, *98*, DOI 10.1063/1.1951057.
- [11] V. G. Kravets, A. V. Kabashin, W. L. Barnes, A. N. Grigorenko, *Chem. Rev.* **2018**, *118*, 5912.
- [12] A. B. Zrimsek, N. Chiang, M. Mattei, S. Zaleski, M. O. McAnally, C. T. Chapman, A. I. Henry, G. C. Schatz, R. P. Van Duyne, *Chem. Rev.* **2017**, *117*, 7583.
- [13] J. M. Nam, J. W. Oh, H. Lee, Y. D. Suh, *Acc. Chem. Res.* **2016**, *49*, 2746.
- [14] G. M. Akselrod, C. Argyropoulos, T. B. Hoang, C. Ciraci, C. Fang, J. Huang, D. R. Smith, M. H. Mikkelsen, *Nat. Photonics* **2014**, *8*, 835.
- [15] J. W. Kang, P. T. C. So, R. R. Dasari, D.-K. Lim, *Nano Lett.* **2015**, 150211151740009.

- [16] K. J. Savage, M. M. Hawkeye, R. Esteban, A. G. Borisov, J. Aizpurua, J. J. Baumberg, *Nature* **2012**, *491*, 574.
- [17] J. M. Kim, C. Lee, Y. Lee, J. Lee, S. J. Park, S. Park, J. M. Nam, *Adv. Mater.* **2021**, *33*, DOI 10.1002/adma.202006966.
- [18] D. K. Lim, K. S. Jeon, H. M. Kim, J. M. Nam, Y. D. Suh, *Nat. Mater.* **2010**, *9*, 60.
- [19] E. C. Le Ru, P. G. Etchegoin, *Annu. Rev. Phys. Chem.* **2012**, *63*, 65.
- [20] J. Langer, D. J. de Aberasturi, J. Aizpurua, R. A. Alvarez-Puebla, B. Auguié, J. J. Baumberg, G. C. Bazan, S. E. J. Bell, A. Boisen, A. G. Brolo, J. Choo, D. Cialla-May, V. Deckert, L. Fabris, K. Faulds, F. Javier García de Abajo, R. Goodacre, D. Graham, A. J. Haes, C. L. Haynes, C. Huck, T. Itoh, M. Käll, J. Kneipp, N. A. Kotov, H. Kuang, E. C. Le Ru, H. K. Lee, J. F. Li, X. Y. Ling, S. A. Maier, T. Mayerhöfer, M. Moskovits, K. Murakoshi, J. M. Nam, S. Nie, Y. Ozaki, I. Pastoriza-Santos, J. Perez-Juste, J. Popp, A. Pucci, S. Reich, B. Ren, G. C. Schatz, T. Shegai, S. Schlücker, L. L. Tay, K. George Thomas, Z. Q. Tian, R. P. van Duyne, T. Vo-Dinh, Y. Wang, K. A. Willets, C. Xu, H. Xu, Y. Xu, Y. S. Yamamoto, B. Zhao, L. M. Liz-Marzán, *ACS Nano* **2020**, *14*, 28.
- [21] D. K. Lim, K. S. Jeon, J. H. Hwang, H. Kim, S. Kwon, Y. D. Suh, J. M. Nam, *Nat. Nanotechnol.* **2011**, *6*, 452.
- [22] M. Kim, S. M. Ko, J. M. Kim, J. Son, C. Lee, W. K. Rhim, J. M. Nam, *ACS Cent. Sci.* **2018**, *4*, 277.
- [23] J. H. Lee, J. W. Oh, S. H. Nam, Y. S. Cha, G. H. Kim, W. K. Rhim, N. H. Kim, J. Kim, S. W. Han, Y. D. Suh, J. M. Nam, *Small* **2016**, *12*, 4726.
- [24] Y. Chen, Y. Xianyu, X. Jiang, *Acc. Chem. Res.* **2017**, *50*, 310.
- [25] Z. Peng, H. Yang, *Nano Today* **2009**, *4*, 143.

- [26] J. W. Oh, D. K. Lim, G. H. Kim, Y. D. Suh, J. M. Nam, *J. Am. Chem. Soc.* **2014**, *136*, 14052.
- [27] H. Lee, S. H. Nam, Y. J. Jung, S. Park, J. M. Kim, Y. D. Suh, D. K. Lim, *J. Mater. Chem. C* **2015**, *3*, 10728.
- [28] J. Shen, X. Jiang, L. Xu, Z. Ge, Q. Li, B. Song, L. Wang, S. Song, *ACS Appl. Nano Mater.* **2019**, *2*, 3501.
- [29] W. Zhou, Y. F. Tian, B. C. Yin, B. C. Ye, *Anal. Chem.* **2017**, *89*, 6120.
- [30] B. Zhao, J. Shen, S. Chen, D. Wang, F. Li, S. Mathur, S. Song, C. Fan, *Chem. Sci.* **2014**, *5*, 4460.
- [31] Y. Wang, K. Sentosun, A. Li, M. Coronado-Puchau, A. Sánchez-Iglesias, S. Li, X. Su, S. Bals, L. M. Liz-Marzán, *Chem. Mater.* **2015**, *27*, 8032.
- [32] Y. Zhang, Y. Gu, J. He, B. D. Thackray, J. Ye, *Nat. Commun.* **2019**, *10*, DOI 10.1038/s41467-019-11829-y.
- [33] Y. Gu, C. He, Y. Zhang, L. Lin, B. D. Thackray, J. Ye, *Nat. Commun.* **2020**, *11*, 1.
- [34] L. Lin, Q. Zhang, X. Li, M. Qiu, X. Jiang, W. Jin, H. Gu, D. Y. Lei, J. Ye, *ACS Nano* **2018**, *12*, 6492.
- [35] N. Gandra, S. Singamaneni, *Adv. Mater.* **2013**, *25*, 1022.
- [36] L. Lin, H. Gu, J. Ye, *Chem. Commun.* **2015**, *51*, 17740.
- [37] B. N. Khlebtsov, N. G. Khlebtsov, *J. Phys. Chem. C* **2016**, *120*, 15385.
- [38] L. Lin, M. Zapata, M. Xiong, Z. Liu, S. Wang, H. Xu, A. G. Borisov, H. Gu, P. Nordlander, J. Aizpurua, J. Ye, *Nano Lett.* **2015**, *15*, 6419.
- [39] J. M. Kim, J. Kim, M. Ha, J. M. Nam, *J. Phys. Chem. Lett.* **2020**, *11*, 8358.
- [40] N. Garg, E. Carrasquillo-Molina, T. R. Lee, *Langmuir* **2002**, *18*, 2717.

- [41] R. Bardhan, S. Mukherjee, N. A. Mirin, S. D. Levit, P. Nordlander, N. J. Halas, *J. Phys. Chem. C* **2010**, *114*, 7378.
- [42] C. Ayala-Orozco, J. G. Liu, M. W. Knight, Y. Wang, J. K. Day, P. Nordlander, N. J. Halas, *Nano Lett.* **2014**, *14*, 2926.
- [43] J. Song, B. Duan, C. Wang, J. Zhou, L. Pu, Z. Fang, P. Wang, T. T. Lim, H. Duan, *J. Am. Chem. Soc.* **2014**, *136*, 6838.
- [44] J. Zhou, Q. Xiong, J. Ma, J. Ren, P. B. Messersmith, P. Chen, H. Duan, *ACS Nano* **2016**, *10*, 11066.
- [45] L. A. Lane, X. Qian, S. Nie, *Chem. Rev.* **2015**, 150827155936004.
- [46] C. Ciraci, R. T. Hill, J. J. Mock, Y. Urzhumov, A. I. Fernández-Domínguez, S. A. Maier, J. B. Pendry, A. Chilkoti, D. R. Smith, *Science* **2012**, *337*, 1072.
- [47] N. A. Mortensen, S. Raza, M. Wubs, T. Søndergaard, S. I. Bozhevolnyi, *Nat. Commun.* **2014**, *5*, DOI 10.1038/ncomms4809.
- [48] W. Zhu, R. Esteban, A. G. Borisov, J. J. Baumberg, P. Nordlander, H. J. Lezec, J. Aizpurua, K. B. Crozier, *Nat. Commun.* **2016**, *7*, DOI 10.1038/ncomms11495.
- [49] H. Jung, H. Cha, D. Lee, S. Yoon, *ACS Nano* **2015**, *9*, 12292.
- [50] H. Cha, J. H. Yoon, S. Yoon, *ACS Nano* **2014**, *8*, 8554.
- [51] S. Simoncelli, E. M. Roller, P. Urban, R. Schreiber, A. J. Turberfield, T. Liedl, T. Lohmüller, *ACS Nano* **2016**, *10*, 9809.
- [52] J. H. Lee, J. M. Nam, K. S. Jeon, D. K. Lim, H. Kim, S. Kwon, H. Lee, Y. D. Suh, *ACS Nano* **2012**, *6*, 9574.
- [53] C. Readman, B. De Nijs, I. Szabó, A. Demetriadou, R. Greenhalgh, C. Durkan, E. Rosta, O. A. Scherman, J. J. Baumberg, *Nano Lett.* **2019**, *19*, 2051.

- [54] K. Y. Loh, X. Liu, *ACS Cent. Sci.* **2018**, *4*, 137.
- [55] J. J. Baumberg, J. Aizpurua, M. H. Mikkelsen, D. R. Smith, *Nat. Mater.* **2019**, *18*, 668.
- [56] J. Mertens, A. L. Eiden, D. O. Sigle, F. Huang, A. Lombardo, Z. Sun, R. S. Sundaram, A. Colli, C. Tserkezis, J. Aizpurua, S. Milana, A. C. Ferrari, J. J. Baumberg, *Nano Lett.* **2013**, *13*, 5033.
- [57] M. Kim, H. Kwon, S. Lee, S. Yoon, *ACS Nano* **2019**, *13*, 12109.
- [58] V. Kulkarni, E. Prodan, P. Nordlander, *Nano Lett.* **2013**, *13*, 5873.
- [59] J. Mertens, M. E. Kleemann, R. Chikkaraddy, P. Narang, J. J. Baumberg, *Nano Lett.* **2017**, *17*, 2568.
- [60] F. Benz, M. K. Schmidt, A. Dreismann, R. Chikkaraddy, Y. Zhang, A. Demetriadou, C. Carnegie, H. Ohadi, B. De Nijs, R. Esteban, J. Aizpurua, J. J. Baumberg, *Science (80-. )*. **2016**, *354*, 726.
- [61] R. Esteban, A. G. Borisov, P. Nordlander, J. Aizpurua, *Nat. Commun.* **2012**, *3*, 825.
- [62] C. Carnegie, J. Griffiths, B. De Nijs, C. Readman, R. Chikkaraddy, W. M. Deacon, Y. Zhang, I. Szabó, E. Rosta, J. Aizpurua, J. J. Baumberg, *J. Phys. Chem. Lett.* **2018**, *9*, 7146.
- [63] H. H. Shin, G. J. Yeon, H. K. Choi, S. M. Park, K. S. Lee, Z. H. Kim, *Nano Lett.* **2018**, *18*, 262.
- [64] F. Benz, C. Tserkezis, L. O. Herrmann, B. De Nijs, A. Sanders, D. O. Sigle, L. Pukenas, S. D. Evans, J. Aizpurua, J. J. Baumberg, *Nano Lett.* **2015**, *15*, 669.
- [65] S. Tan, L. Wu, J. K. W. Yang, P. Bai, M. Bosman, C. A. Nijhuis, *Science* **2014**, *343* VN-, 1496.
- [66] X. Cui, F. Qin, Y. Lai, H. Wang, L. Shao, H. Chen, J. Wang, H. Q. Lin, *ACS Nano* **2018**, *12*, 12541.

- [67] T. Jibowu, *Front. Nanosci. Nanotechnol.* **2016**, *2*, 165.
- [68] T. Bryce C, S. Stephen A, E. P. Luther, *Angew. Chemie - Int. Ed.* **2010**, *49*, 4544.
- [69] Z. Su, T. Chen, *Small* **2021**, *17*, 1.
- [70] C. Zhu, D. Du, A. Eychmüller, Y. Lin, *Chem. Rev.* **2015**, *115*, 8896.
- [71] A. N. Koya, X. Zhu, N. Ohannesian, A. A. Yanik, A. Alabastri, R. Proietti Zaccaria, R. Krahne, W. C. Shih, D. Garoli, *ACS Nano* **2021**, *15*, 6038.
- [72] S. J. Park, H. Han, H. Rhu, S. Baik, W. Lee, *J. Mater. Chem. C* **2013**, *1*, 5330.
- [73] Y. Kanno, T. Suzuki, Y. Yamauchi, K. Kuroda, *J. Phys. Chem. C* **2012**, *116*, 24672.
- [74] S. Pedireddy, H. K. Lee, W. W. Tjiu, I. Y. Phang, H. R. Tan, S. Q. Chua, C. Troadec, X. Y. Ling, *Nat. Commun.* **2014**, *5*, 1.
- [75] Q. Yu, H. Huang, R. Chen, H. Yang, X. Peng, Z. Ye, *J. Mater. Chem.* **2011**, *21*, 18089.
- [76] T. Juarez, J. Biener, J. Weissmüller, A. M. Hodge, *Adv. Eng. Mater.* **2017**, *19*, 1.
- [77] R. Liquid, J. Erlebacher, M. J. Aziz, A. Karma, N. Dimitrov, *Nature* **2001**, *410*, 5.
- [78] I. McCue, E. Benn, B. Gaskey, J. Erlebacher, *Annu. Rev. Mater. Res.* **2016**, *46*, 263.
- [79] Z. Zhang, Y. Wang, Z. Qi, W. Zhang, J. Qin, J. Frenzel, *J. Phys. Chem. C* **2009**, *113*, 12629.
- [80] D. Wang, P. Schaaf, *J. Mater. Chem.* **2012**, *22*, 5344.
- [81] Y. Ding, Y. J. Kim, J. Erlebacher, *Adv. Mater.* **2004**, *16*, 1897.
- [82] K. Liu, Y. Bai, L. Zhang, Z. Yang, Q. Fan, H. Zheng, Y. Yin, C. Gao, *Nano Lett.* **2016**, *16*, 3675.
- [83] M. Kim, S. M. Ko, J. M. Nam, *Nanoscale* **2016**, *8*, 11707.
- [84] J. Biener, M. M. Biener, R. J. Madix, C. M. Friend, *ACS Catal.* **2015**, *5*, 6263.
- [85] J. Fu, E. Detsi, J. T. M. De Hosson, *Surf. Coatings Technol.* **2018**, *347*, 320.

- [86] P. Liu, P. Guan, A. Hirata, L. Zhang, L. Chen, Y. Wen, Y. Ding, T. Fujita, J. Erlebacher, M. Chen, *Adv. Mater.* **2016**, *28*, 1753.
- [87] W. Zhang, J. He, S. Liu, W. Niu, P. Liu, Y. Zhao, F. Pang, W. Xi, M. Chen, S. S. Pang, Y. Ding, *Nanoscale* **2018**, *10*, 8372.
- [88] T. Fujita, P. Guan, K. McKenna, X. Lang, A. Hirata, L. Zhang, T. Tokunaga, S. Arai, Y. Yamamoto, N. Tanaka, Y. Ishikawa, N. Asao, Y. Yamamoto, J. Erlebacher, M. Chen, *Nat. Mater.* **2012**, *11*, 775.
- [89] R. Zeis, T. Lei, K. Sieradzki, J. Snyder, J. Erlebacher, *J. Catal.* **2008**, *253*, 132.
- [90] Y. Ding, M. Chen, *MRS Bull.* **2009**, *34*, 569.
- [91] H. Falsig, B. Hvolbæk, I. S. Kristensen, T. Jiang, T. Bligaard, C. H. Christensen, J. K. Nørskov, *Angew. Chemie - Int. Ed.* **2008**, *47*, 4835.
- [92] G. Hyun, J. T. Song, C. Ahn, Y. Ham, D. Cho, J. Oh, S. Jeon, *Proc. Natl. Acad. Sci. U. S. A.* **2020**, *117*, 5680.
- [93] Z. Wang, P. Liu, J. Han, C. Cheng, S. Ning, A. Hirata, T. Fujita, M. Chen, *Nat. Commun.* **2017**, *8*, 1.
- [94] Z. Wang, S. Ning, P. Liu, Y. Ding, A. Hirata, T. Fujita, M. Chen, *Adv. Mater.* **2017**, *29*, 1.
- [95] S. Mezzavilla, S. Horch, I. E. L. Stephens, B. Seger, I. Chorkendorff, *Angew. Chemie* **2019**, *131*, 3814.
- [96] M. L. Personick, B. Zugic, M. M. Biener, J. Biener, R. J. Madix, C. M. Friend, *ACS Catal.* **2015**, *5*, 4237.
- [97] C. H. W. Kelly, T. M. Benedetti, A. Alinezhad, W. Schuhmann, J. J. Gooding, R. D. Tilley, *J. Phys. Chem. C* **2018**, *122*, 21718.
- [98] T. Campbell, *Surf. Sci.* **1985**, *157*, 43.

- [99] L. V. Moskaleva, S. Röhe, A. Wittstock, V. Zielasek, T. Klüner, K. M. Neyman, M. Bäumer, *Phys. Chem. Chem. Phys.* **2011**, *13*, 4529.
- [100] L. V. Moskaleva, T. Weiss, T. Klüner, M. Bäumer, *J. Phys. Chem. C* **2015**, *119*, 9215.
- [101] G. G. Li, Y. Lin, H. Wang, *Nano Lett.* **2016**, *16*, 7248.
- [102] S. Kameoka, A. P. Tsai, *Catal. Letters* **2008**, *121*, 337.
- [103] S. Laing, L. E. Jamieson, K. Faulds, D. Graham, *Nat. Rev. Chem.* **2017**, *1*, 1.
- [104] S.-Y. Ding, J. Yi, J.-F. Li, B. Ren, D.-Y. Wu, R. Panneerselvam, Z.-Q. Tian, *Nat. Rev. Mater.* **2016**, *1*, 16021.
- [105] R. Bardhan, S. Mukherjee, N. A. Mirin, S. D. Levit, P. Nordlander, N. J. Halas, *J. Phys. Chem. C* **2010**, *114*, 7378.
- [106] J. Song, B. Duan, C. Wang, J. Zhou, L. Pu, Z. Fang, P. Wang, T. T. Lim, H. Duan, *J. Am. Chem. Soc.* **2014**, *136*, 6838.
- [107] J. Li, Z. Zhu, B. Zhu, Y. Ma, B. Lin, R. Liu, Y. Song, H. Lin, S. Tu, C. Yang, *Anal. Chem.* **2016**, *88*, 7828.
- [108] Y. Zhao, F. Zheng, W. Ke, W. Zhang, L. Shi, H. Liu, *Anal. Chem.* **2019**, *91*, 7162.
- [109] Z. Zhang, S. Zhang, M. Lin, *Chem. Commun.* **2013**, *49*, 8519.
- [110] G. Bhattacharjee, S. Majumder, D. Senapati, S. Banerjee, B. Satpati, *Mater. Chem. Phys.* **2020**, *239*, DOI 10.1016/j.matchemphys.2019.122113.
- [111] J. E. Park, S. Kim, J. Son, Y. Lee, J. M. Nam, *Nano Lett.* **2016**, *16*, 7962.
- [112] L. Ma, Y. L. Chen, D. J. Yang, H. X. Li, S. J. Ding, L. Xiong, P. L. Qin, X. B. Chen, *Nanoscale* **2020**, *12*, 4383.
- [113] W. Zhang, M. Rahmani, W. Niu, S. Ravaine, M. Hong, X. Lu, *Sci. Rep.* **2015**, *5*, 8382.
- [114] H. T. Ngo, E. Freedman, R. A. Odion, P. Strobbia, A. S. De Silva Indrasekara, P. Vohra,

- S. M. Taylor, T. Vo-Dinh, *Sci. Rep.* **2018**, *8*, 1.
- [115] A. Jaiswal, L. Tian, S. Tadepalli, K. K. Liu, M. Fei, M. E. Farrell, P. M. Pellegrino, S. Singamaneni, *Small* **2014**, *10*, 4287.
- [116] M. Kim, S. M. Ko, J. M. Kim, J. Son, C. Lee, W. K. Rhim, J. M. Nam, *ACS Cent. Sci.* **2018**, *4*, 277.
- [117] M. Urbietta, M. Barbry, Y. Zhang, P. Koval, D. Sánchez-Portal, N. Zabala, J. Aizpurua, *ACS Nano* **2018**, *12*, 585.
- [118] J. E. Park, Y. Jung, M. Kim, J. M. Nam, *ACS Cent. Sci.* **2018**, *4*, 1303.
- [119] J. Kim, K. Sim, S. Cha, J. W. Oh, J. M. Nam, *J. Raman Spectrosc.* **2021**, *52*, 375.
- [120] Y. Wang, B. Yan, L. Chen, *Chem. Rev.* **2013**, *113*, 1391.
- [121] H. Lee, J. H. Lee, S. M. Jin, Y. D. Suh, J. M. Nam, *Nano Lett.* **2013**, *13*, 6113.
- [122] W. Song, W. Li, Y. Cheng, H. Jia, G. Zhao, Y. Zhou, B. Yang, W. Xu, W. Tian, B. Zhao, *J. Raman Spectrosc.* **2006**, *37*, 755.
- [123] W. Song, Y. Wang, B. Zhao, *J. Phys. Chem. C* **2007**, *111*, 12786.
- [124] G. Gramlich, J. Zhang, W. M. Nau, *J. Am. Chem. Soc.* **2002**, *124*, 11252.
- [125] Y. C. Tsao, S. Rej, C. Y. Chiu, M. H. Huang, *J. Am. Chem. Soc.* **2014**, *136*, 396.
- [126] X. Xia, Y. Wang, A. Ruditskiy, Y. Xia, *Adv. Mater.* **2013**, *25*, 6313.
- [127] Y. Xia, X. Xia, H.-C. Peng, *J. Am. Chem. Soc.* **2015**, 150528140910003.
- [128] M. Haruta, T. Kobayashi, H. Sano, N. Yamada, *Chem. Lett.* **1987**, *16*, 405.
- [129] M. Valden, X. Lai, D. W. Goodman, *Science (80-. )*. **1998**, *281*, 1647.
- [130] G. W. Brudvig, T. M. Iverson, K. Maghlaoui, J. Barber, S. Iwata, J. Kern, W. Saenger, A. Zouni, J. Biesiadka, M. Haumann, K. Kawakami, J. R. Shen, N. Kamiya, R. H. Crabtree, G. W. Brudvig, A. Grundmeier, P. Loja, M. Haumann, J. W. Murray, V. L. Pecoraro, G.

- Christou, M. Yagi, M. Kaneko, S. Mukhopadhyay, S. K. Mandal, S. Bhaduri, W. H. Armstrong, A. Mishra, W. Wernsdorfer, K. A. Abboud, G. Christou, V. Kotzabasaki, M. Siczek, T. Lis, C. J. Milios, S. Nayak, H. P. Nayek, S. Dehnen, A. K. Powell, J. Reedijk, Y. J. Park, J. W. Ziller, A. S. Borovik, E. Y. Tsui, M. W. Day, T. Agapie, E. Y. Tsui, J. S. Kanady, M. W. Day, T. Agapie, J. Yano, V. K. Yachandra, J. P. Mcevoy, J. A. Gascon, V. S. Batista, G. W. Brudvig, J. Messinger, M. Arjomand, D. J. Machin, W. Levason, C. A. Mcauliffe, M. D. Symes, Y. Surendranath, D. A. Lutterman, D. G. Nocera, M. W. Kanan, D. G. Nocera, T. Ehrenberg, M. Wiechen, P. Kurz, S. V Baranov, G. M. Ananyev, G. C. Dismukes, J. Kazimir, G. M. Cheniae, **2011**, 736.
- [131] Y. Kuwauchi, H. Yoshida, T. Akita, M. Haruta, S. Takeda, *Angew. Chemie - Int. Ed.* **2012**, *51*, 7729.
- [132] A. Wittstock, V. Zielasek, J. Biener, C. M. Friend, M. Bäumer, *Science (80-. )*. **2010**, *327*, 319.
- [133] V. Zielasek, B. Jürgens, C. Schulz, J. Biener, M. M. Biener, A. V. Hamza, M. Bäumer, *Angew. Chemie - Int. Ed.* **2006**, *45*, 8241.
- [134] C. Xu, J. Su, X. Xu, P. Liu, H. Zhao, F. Tian, Y. Ding, *J. Am. Chem. Soc.* **2007**, *129*, 42.
- [135] G. G. Li, H. Wang, *ChemNanoMat* **2018**, *4*, 897.
- [136] Y. Yi, X. Zheng, Z. Fu, C. Wang, X. Xu, X. Tan, *Materials (Basel)*. **2018**, *11*, DOI 10.3390/ma11030380.
- [137] M. Di Vece, N. P. Young, Z. Li, Y. Chen, R. E. Palmer, *Small* **2006**, *2*, 1270.
- [138] M. D. and A. G. Corby, *Icmm* **2009**, 1.
- [139] M. D. Urović, R. Puchta, Ž. D. Bugarčić, R. Van Eldik, *Dalt. Trans.* **2014**, *43*, 8620.
- [140] Y. Zhang, J. G. Wang, X. Yu, D. R. Baer, Y. Zhao, L. Mao, F. Wang, Z. Zhu, *ACS*

*Energy Lett.* **2019**, *4*, 215.

- [141] Y. H. Tan, J. A. Davis, K. Fujikawa, N. V. Ganesh, A. V. Demchenko, K. J. Stine, *J. Mater. Chem.* **2012**, *22*, 6733.
- [142] Z. Liu, G. Fu, Y. Tang, D. Sun, Y. Chen, T. Lu, *CrystEngComm* **2014**, *16*, 8576.
- [143] J. Huang, X. Han, D. Wang, D. Liu, T. You, *ACS Appl. Mater. Interfaces* **2013**, *5*, 9148.
- [144] T. Li, G. Fu, J. Su, Y. Wang, Y. Lv, X. Zou, X. Zhu, L. Xu, D. Sun, Y. Tang, *Electrochim. Acta* **2017**, *231*, 13.
- [145] J. J. Feng, A. Q. Li, Z. Lei, A. J. Wang, *ACS Appl. Mater. Interfaces* **2012**, *4*, 2570.
- [146] M. A. Mahmoud, R. Narayanan, M. A. El-Sayed, *Acc. Chem. Res.* **2013**, *46*, 1795.
- [147] S. Beyhan, K. Uosaki, J. M. Feliu, E. Herrero, *J. Electroanal. Chem.* **2013**, *707*, 89.
- [148] K. Shen, C. Jia, B. Cao, H. Xu, J. Wang, L. Zhang, K. Kim, W. Wang, *Electrochim. Acta* **2017**, *256*, 129.
- [149] Y. N. Wen, J. M. Zhang, *Solid State Commun.* **2007**, *144*, 163.

## **Chapter 2.**

# **The Effect of Intragap Morphology of Core-gap-shell Structure on the SERS Uniformity and Stability**

## 2.1 Introduction

Surface-enhanced Raman scattering (SERS) is a powerful technique that provides high sensitivity and high specificity for molecular spectroscopy and is beneficial for sensing, imaging, and diverse applications.<sup>[1–3]</sup> Plasmonic gap nanostructures have been extensively investigated as SERS probes.<sup>[4,5]</sup> Plasmonic coupling in closely adjacent structures strongly confines the incident light and localized fields in the nanogap region. Importantly, the nanometer (nm)-sized internal spacing in a nanoparticle, which is called intragap, substantially enhances the near-field and SERS intensities. Moreover, owing to structural advantages, such as fixed gap sizes, fixed morphologies, and confinement by the solid shell, of intragap, the signal variation effect in the surrounding environment is slight.<sup>[6]</sup> Additionally, it is easy to modify by specific ligands in the outer shell region for further processing applications.<sup>[7]</sup> SERS signals with strong, stable, reliable, and quantitative properties with intragap nanoparticles has a big chance to advance to practical applications. Significant progress has been made in the synthesis of substantially advanced intragap SERS nanoprobos. The representative strategies reported to date for forming an intragap in an Au-based core-gap-shell structure involve the use of DNA,<sup>[6,8–12]</sup> benzene thiol,<sup>[13–18]</sup> cyclodextrin,<sup>[19]</sup> silica,<sup>[20,21]</sup> polymer,<sup>[22]</sup> and polydopamine<sup>[23]</sup> as interlayer materials or galvanic replacement<sup>[24–33]</sup> and dealloying<sup>[34]</sup>. Depending on the materials adopted, different growth strategies, including nucleation on the core, metal shell growth on the spacer layer, and application of a sacrificial metal layer, are employed to develop a core-gap-shell structure.<sup>[5]</sup> These growth strategies

govern the size and morphology of the intragap. In addition to component and dielectric constants, the size and morphology of the intragap considerably influence the intensity of the local electric field formed in the gap. Particularly, the SERS enhancement factor (EF) is approximately proportional to the fourth power of the local electric field intensity.<sup>[3]</sup> Thus, slight variations in the few nm-scale morphology of intragap can substantially affect the near-field distribution. Many studies have reported spectroscopic measurements of the Raman signals of single molecules adjacent to small protuberances inside the gap, so-called picocavity, and found that the ultrasmall lightning-rod additionally enhances the electric-field intensity.<sup>[35-38]</sup> However, this picocavity and nanoscale roughness induce inhomogeneity in the optical properties of intragap nanoparticles. Furthermore, these structures are inhomogeneous and unstable, easily expose and collapse, and deform under harsh conditions such as high laser power and thermal state. Notably, the importance of a uniform and stable SERS signal of individual intragap nanoparticles increases when the signals need to be quantitatively analyzed according to the number of particles.<sup>[39,40]</sup> Moreover, in the biodetection field, the signals of nanoparticles are related to the amounts of the target molecule to be detected.<sup>[41]</sup> For the analysis of infinitesimal target molecules with few nanoparticles, uniform SERS intensity of individual nanoparticles becomes more critical. Therefore, nm-scale precisions and well-defined morphologies of nanoparticles should be considered, inducing homogeneous optical properties from particle to particle. Previous studies on intragap nanostructures were usually focused on the materials or synthesis methods that

could produce intragaps. Most of these studies involved complex geometries of the gap and could not precisely determine the effects of intragap morphology on the optical properties of nanostructures due to the absence of a synthetic method for intragap nanostructures. Thus, to generate intragap nanoparticles with reproducible and narrow distributions of SERS signals, the methods for the preparation of intragap nanoparticles need to be improved and our understanding of the effects of intragap geometries on the uniformities and photostabilities of SERS signals need to be extended via experimental, computational, and comparative analyses. Herein, we proved the considerable effect of intragap morphology on the uniformity and photostability of plasmon-enhanced optical signal at the single-particle level by comparing two types of core-gap-shell structures.

## 2.2 Experimental Section

### Reagents

Gold(III) chloride trihydrate ( $\text{HAuCl}_4 \cdot \text{H}_2\text{O}$ ,  $\geq 99.9\%$ ), silver nitrate ( $\text{AgNO}_3$ , 99.9999%), 4-mercaptopyridine (4-MPy, 95%), sodium dodecyl sulfate (SDS,  $\geq 98.5\%$ ), polyvinylpyrrolidone (PVP,  $M_w \approx 40000$ ), ammonium hydroxide solution ( $\text{NH}_4\text{OH}$ , 28-30%  $\text{NH}_3$  basis), (+)-Sodium L-ascorbate ( $\text{C}_6\text{H}_7\text{NaO}_6$ , L-SA,  $\geq 98\%$ ), L-ascorbic acid ( $\text{C}_6\text{H}_8\text{O}_6$ , AA,  $\geq 99.0\%$ ), iron(III) nitrate nonahydrate ( $\text{Fe}(\text{NO}_3)_3 \cdot 9\text{H}_2\text{O}$ ,  $\geq 98.0\%$ ), was purchased from Sigma-Aldrich. Cetyltrimethylammonium chloride (CTAC) was purchased from Tokyo Chemical Industry (TCI). Dimethyl sulfoxide (DMSO) was purchased from Samchun Chemicals, Deionized water (DIW; Milli-Q,  $> 18.0 \text{ M}\Omega\text{-cm}$ )

was used in all experiments.

## **Experimental Methods**

### **Synthesis of single-crystal 40 nm Au nanosphere (AuNS)**

CTAC-capped 40 nm AuNS was synthesized by seed-mediated growth procedure according to a previous protocol with minor modification.<sup>[42]</sup> First, 2-3 nm of CTAB-capped Au seed were synthesized. We prepared 9.75 mL of 100 mM CTAB solution mixed with 250  $\mu$ L of 10 mM HAuCl<sub>4</sub> solution in a 70 mL glass vial, followed by a one-shot injection of 600  $\mu$ L of A fresh, ice-cold aqueous 10 mM NaBH<sub>4</sub> solution. The reaction was held with vigorous stirring (500 rpm) for 2 min and kept undisturbed for 3 h. Next, 10 nm AuNS were synthesized with the initial 2-3 nm Au seeds. Aqueous solutions of 2 mL of 200 mM CTAC, 1.5 mL of 100 mM AA, and 50  $\mu$ L of as-prepared Au seed were sequentially added in a 20 mL glass vial, followed by 2 mL of 0.5 mM of HAuCl<sub>4</sub> at a time. The reaction was allowed to proceed at 27 °C for 15 min under vigorous stirring (500 rpm). The product was centrifuged twice at 14500 rpm for 30 min by DIW followed by 20 mM CTAC solution. Lastly, 40 nm AuNS was synthesized by dropwise addition of 1 mL of 25 mM of HAuCl<sub>4</sub> solution in to 50 mL of 100 mM CTAC, 3.25 mL of 8 mM AA, 290  $\mu$ L of 10 nm Au seed an injection rate of 1 mL/h. After the injection finished, the reaction was incubated at 27 °C for 15 min. The final product was centrifuged twice at 7000 rpm, 10 min with 1 mM CTAC and DIW.

### **Preparation of 4-MPy-modified Au nanosphere (MPy-AuNS)**

Before modifying 40 nm AuNS with 4-MPy, the surface ligand of AuNS was exchanged from CTAC to SDS by centrifuge with 1% (w/v) SDS solution twice and with 0.1% SDS solution twice. Next, to modify 4-MPy on the surface of 40 nm AuNS, 10  $\mu\text{L}$  of a 50 mM 4-MPy dissolved in DMSO was injected into 1 mL of 100 pM AuNS in a 0.1% SDS solution. The solution was sonicated for 10 min and incubated for 6 h at 60  $^{\circ}\text{C}$ . Then, the MPy-AuNS were centrifuged at 7000 rpm for 10 min and dispersed in DIW for further use.

### **Synthesis of poly-crystalline rough intragap particles (PRINs)**

The PRINs were synthesized using a previously reported procedure with some modifications.<sup>[43]</sup> The 50  $\mu\text{L}$  of 200 pM MPy-AuNS was gently mixed with 100  $\mu\text{L}$  of 1 wt% polyvinylpyrrolidone (PVP,  $M_w \approx 40000$ ) solution and incubated for 10 min at 30  $^{\circ}\text{C}$  before reaction. Then, 20  $\mu\text{L}$  of 1 mM  $\text{AgNO}_3$  solution, 10  $\mu\text{L}$  of a stock  $\text{NH}_4\text{OH}$  solution, and 100  $\mu\text{L}$  of a 1 mM  $\text{HAuCl}_4$  were sequentially added. Next, 100  $\mu\text{L}$  of a 20 mM L-SA solution was injected into the mixture under gentle shaking. The reaction was held for 1h at 30  $^{\circ}\text{C}$ . After the reaction was over, the solution was washed with DIW by centrifugation at 7000 rpm for 5 min and redispersed in 100  $\mu\text{L}$  of DIW. Next, the resulting solution of 100  $\mu\text{L}$  was mixed with 100  $\mu\text{L}$  of 1% PVP and introduced 100  $\mu\text{L}$  of 20 mM of  $\text{Fe}(\text{NO}_3)_3$  as an Ag etchant with gentle shaking and reacted for 30 min at 30  $^{\circ}\text{C}$ . The final product was washed twice with DIW by centrifugation at 7500 rpm for 5

min.

### **Synthesis of single-crystalline smooth intragap particles (SSINs)**

To synthesize SSINs, silver shell formation and galvanic replacement/reduction reaction (GRR) were performed in a sequence. First, the previously prepared 100  $\mu\text{L}$  of 100 pM MPy-AuNS was gently mixed with 100  $\mu\text{L}$  of 100 mM CTAC and incubated for 10 min at 30  $^{\circ}\text{C}$  before reaction. Then, 20  $\mu\text{L}$  of 1 mM  $\text{AgNO}_3$  solution, 10  $\mu\text{L}$  of a 100 mM  $\text{NH}_4\text{OH}$  solution, and 100  $\mu\text{L}$  of a 20 mM L-SA solution were sequentially added to the mixture under gentle shaking. The reaction was held for 1h at 30  $^{\circ}\text{C}$ . After the reaction was over, the solution was washed twice with 1 mM CTAC by centrifugation at 7000 rpm for 5 min and get MPy-AuNS core-silver shell nanoparticles (MPy-AuNS@Ag). Next, MPy-AuNS@Ag solution was mixed with 1 ml of 50 mM CTAC and incubated for 5 min at 90  $^{\circ}\text{C}$  for GRR. Finally, 100  $\mu\text{L}$  of 20 mM of AA solution and 100  $\mu\text{L}$  of 1 mM  $\text{HAuCl}_4$  solution were sequentially injected with gentle shaking and reacted for 30 min at 90  $^{\circ}\text{C}$ . The resulting mixture was washed twice with 1 mM CTAC by centrifugation at 7000 rpm for 10 min and redispersed in DIW.

### **Solution-based SERS measurement from micro-Raman spectroscopy**

The 100 pM SSINs or PRINs solution was stuffed into a capillary tube (Cat. No. 2502; soda-lime glass; Kimble Chase) to measure solution-based SERS spectra. The measurements were performed by using a Renishaw Raman microscope equipped with a

20× objective lens (NA = 0.40, Leica) and a standard charge-coupled device (CCD) detector (576 x 384 pixels; Peltier; cooled to -70 °C). The SERS spectra were obtained by using 514 nm (5 mW), 633 nm (3 mW), and 785 nm (6 mW) excitation lasers with an acquisition time of 10 s.

### **Single-particle Dark-field (DF) measurement**

The samples were prepared by drop-casting on a cover glass and let for 3 minutes, followed by blowing using an air pump for dispersity and removing residual surfactants. DF images and spectra were taken with an inverted microscopy system (Ntegra, NT-MDT). An oil condenser with NA 1.3 was used for DF measurements, and an objective lens (UNPLAN, 60x, NA 0.90) was used to obtain scattering spectra. All the spectra were measured from 5 different particles from each sample observed in DF with an exposure time of 1 s.

### **Single particle SERS measurement form AFM-correlated Raman spectroscopy**

The samples were prepared by drop-casting on a cover glass and let for 3 minutes, followed by blowing using an air pump for dispersity and removing residual surfactants. Single-particle level SSIN SERS spectra were obtained using an AFM-correlated Raman microscope (Ntegra, NT-MDT) equipped with an inverted optical microscope (IX73, Olympus) and an oil-immersion microscope objective (100×, NA = 1.4, Olympus). The laser beam was first focused on the upper surface of SSINs-loaded cover glass to match

an AFM-tip position and laser focal spot.<sup>[6,44]</sup> Then, the AFM-tip was scanned along the x- and y-axes, using a piezoelectric x, y tube scanner in the AFM head, verified laser focal spot at the highest Raman signal of the silicon (520 cm<sup>-1</sup>) detected by charged-coupled device (CCD, Peltier cooled to -70 °C). The Rayleigh scattering obtained a 785 nm excitation laser and matched it with AFM topographical images, further identifying that the SERS spectra from SSIN are at a single-particle level. The SERS spectra from individual SSINs were obtained from the position where Rayleigh scattering occurs in a photomultiplier tube image. The SERS spectra were obtained using 785 nm (170 μW) with an acquisition time of 10 s.

### SERS enhancement factor calculation

The SERS enhancement factor (EF) was calculated by the following equation:

$$\text{SERS enhancement factor (EF)} = \frac{I_{SERS}}{I_{Bulk}} / \frac{N_{SERS}}{N_{Bulk}} \times \frac{\nu^4_{Bulk}}{\nu^4_{SERS}} \quad (1)$$

Where  $I_{SERS}$  and  $I_{Bulk}$  are the intensities of the Raman peak at 1098 cm<sup>-1</sup> for the individual SSIN and 4-MPy aqueous solution (10 mM in distilled water pH 4.74).  $I_{SERS}$  was obtained by 785 nm laser with an acquisition time of 10 s, and  $I_{Bulk}$  was obtained by 633 nm laser with an acquisition time of 60 s. The  $\nu^4_{SERS}$  and  $\nu^4_{Bulk}$  are frequencies of the excitation laser. The  $N_{SERS}$  and  $N_{Bulk}$  are the number of 4-MPy molecules on a single SSIN and within the solution, respectively. The number of 4-MPy molecules on a single SSIN ( $N_{SERS}$ ) was assumed by the fully packed on the 40 nm AuNP core; the average molecular

footprint of 4-MPy has been estimated to be 0.18 nm<sup>2</sup>.<sup>[45,46]</sup> To estimate  $N_{bulk}$ , we assume that the effective excitation volume ( $V_{Bulk}$ ) is a cylinder, and the height (h) was calculated using the following equation (Equation2);

$$\frac{h}{2r} = \frac{3.28\eta}{NA} \quad (2)$$

Where  $\eta$  is the refractive index of the medium (water; 1.33), and the radius (r) was 2  $\mu\text{m}$  which is estimated by a knife-edge method with a silicon wafer. Further,  $N_{Bulk}$  was calculated using the following equation (Equation3);

$$N_{Bulk} = \left( V_{Bulk} \times \frac{D}{M} \right) \times N_A \quad (3)$$

Where  $D$  is the density of 4-MPy (22.23 mg/mL),  $M$  is the molar mass of 4-MPy (111.16 g/mol), and  $N_A$  is Avogadro's constant ( $6.02 \times 10^{23} \text{ mol}^{-1}$ ).

## Characterization

The morphological characteristics of the nanoparticles were obtained by TEM (JEM-2100, JEOL), a high-resolution TEM (HR-TEM) (JEM-2100F, JEOL). The elemental maps of the nanoparticles were obtained by EDS system (INCA, Oxford Instruments) coupled with an HR-TEM. The extinction spectra were obtained by an UV-vis spectrophotometer (HP-8453, Agilent Technologies).

## 2.3 Results and Discussion

We selected galvanic replacement/reduction (GRR) and slightly modified selective interdiffusion dealloying (SID) to control the shape of the intragap and the crystallinity of the shell. We used 4-mercaptopyridine (4-Mpy)-modified 40 nm single-crystalline Au nanoparticles as the core in both reactions (Figure 2.1). At first, the core was synthesized in high yield by seed-mediated growth (Figure 2.2). Subsequently, we performed GRR to fabricate single-crystalline and smooth intragap particles (SSINs) and slightly modified SID to synthesize polycrystalline rough intragap nanoparticles (PRINs). During the preparation of SSINs, we initially formed a highly uniform  $\sim 3$  nm Ag shell on the 4-Mpy-modified core by optimizing the reducing agent and the amount of  $\text{NH}_4\text{OH}$  (Figures 2.3 and 2.4). Constant thickness of Ag shell plays a critical role in the development of an intragap with uniform size as it facilitates the occurrence of GRR at the same rate from the outer Ag shell region to the core. Sodium L-ascorbic acid (L-SA), an oxidized form of ascorbic acid (AA), is a reducing agent generally used for metal nanoparticle synthesis and provides a fast and stable reduction rate under high pH conditions.<sup>[47]</sup> Therefore, when the Ag precursor is reduced by L-SA, a Ag shell with uniform thickness as compared to that of the shell acquired using AA is obtained; nevertheless, the reduction potential of L-SA is relatively sensitive to pH (Figure 2.3). When an optimized amount of  $\text{NH}_4\text{OH}$  is employed, the reduction potential of L-SA increases because of the increase in pH, and the formation of AgCl is prevented.<sup>[48]</sup> We achieved Ag shells with constant thicknesses for each core at optimized pH. The same result was obtained when NaOH at

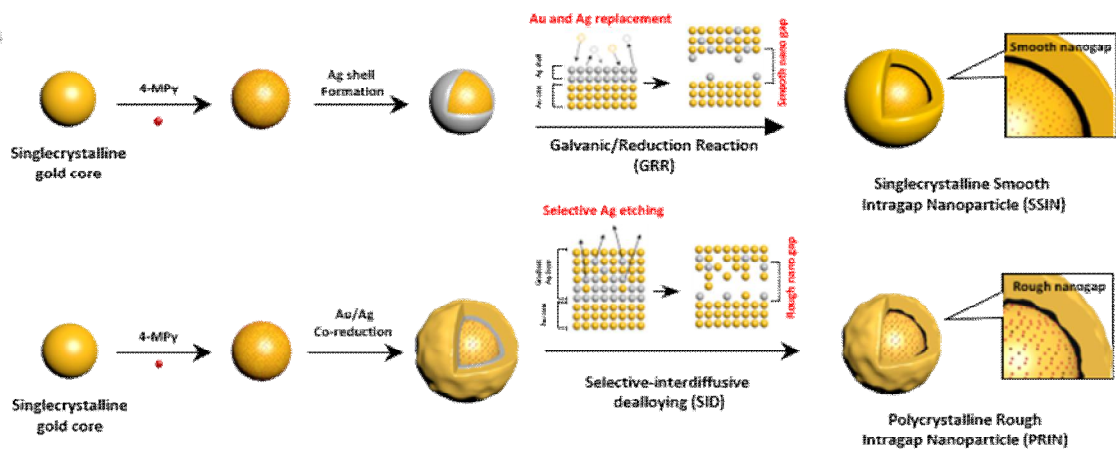


**Figure 2.1 Synthetic strategy of singlecrystalline smooth intragap nanoparticles (SSINs) and polycrystalline rough intragap nanoparticles (PRINs).** Scheme for synthesizing SSINs and PRINs through a galvanic/reduction reaction (GRR) and selective-interdiffusive dealloying (SID) process, respectively.

the same concentration as that of  $\text{NH}_4\text{OH}$  was employed instead of  $\text{NH}_4\text{OH}$  (0.1 M, pH:  $\sim 10$ , Figure 2.4). When excess or no  $\text{NH}_4\text{OH}$  was added, byproducts formed by self-nucleation or the thickness of the Ag shell considerably varied from particle to particle, respectively. Thus, we used L-SA and 0.1 M  $\text{NH}_4\text{OH}$  to form a uniform and spherical Ag shell. Thereafter, the developed core-Ag shell particles were subjected to GRR for 30 minutes in the presence of a Au precursor and AA at 90 °C, and finally, SSINs were formed. Galvanic replacement spontaneously replaced three Ag atoms with one Au atom because the standard reduction potential of  $\text{AuCl}_4^-/\text{Au}$  (0.99 V vs. standard hydrogen electrode, SHE) is higher than that of  $\text{AgCl}/\text{Ag}$  (0.22 V vs. SHE).<sup>[49]</sup> As we aimed to use Ag sacrificial layers to form a nm-scale intragap, we prepared thin Ag shells; however, they were not sufficient for the formation of  $\sim 13$  nm thick, robust Au shells by spontaneous galvanic replacement. Therefore, we simultaneously conducted both replacement and reduction by adding AA during the reaction. Temperature control during the GRR step was critical for forming a robust and smooth Au shell. Particularly, only high temperatures resulted in nearly smooth, solid, and robust spherical Au shells (Figure 2.5A). In contrast, when the GRR was performed at 25 or 60 °C, a rough shell and an irregular intragap were acquired (Figures 2.5B and C). When the temperature was increased to approximately 90 °C during the reaction, as the formation of AgCl is prevented, and a flat and even surface shell was achieved. To synthesize PRINs and compare their optical properties with those of SSINs according to the shape of the intragap, we intentionally roughened the intragap shape by modifying

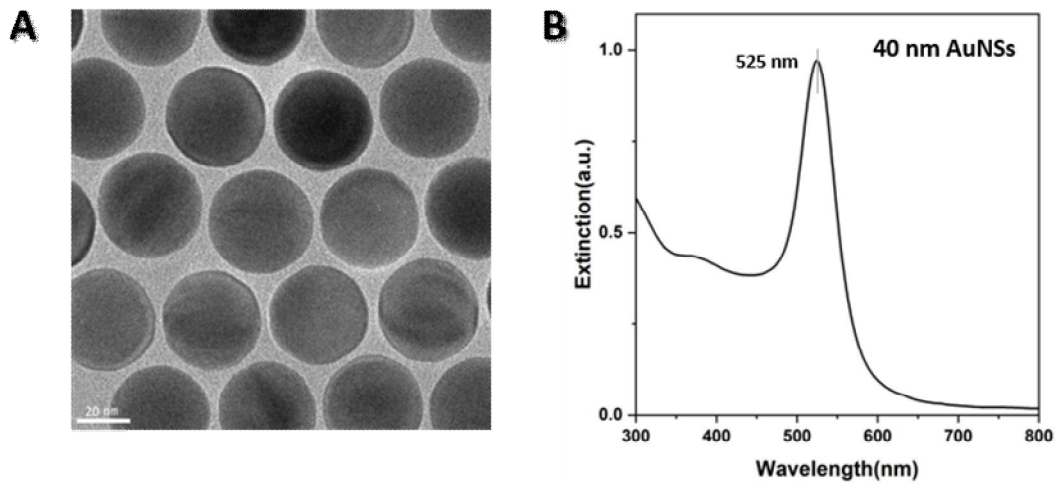


**Figure 2.2 (A) TEM and (B) UV-Vis extinction of 40 nm Au nanosphere particles (AuNSs).**

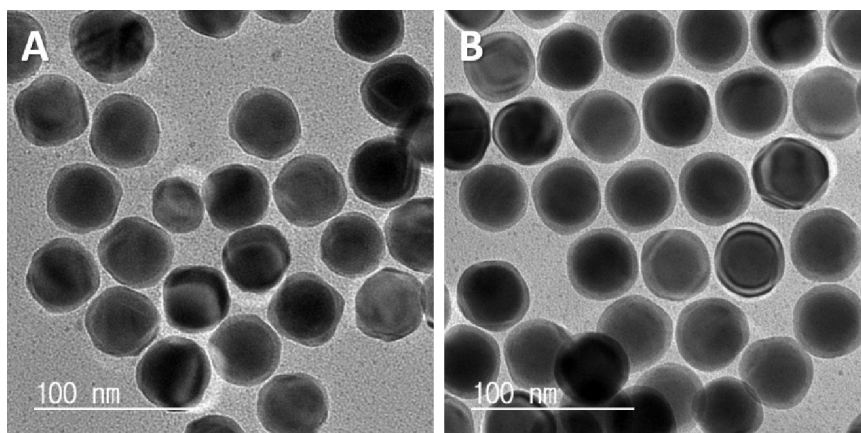


**Figure 2.3 Different reducing agent effects on the silver shell Au core-Ag shell formation with (A) AA and (B) L-SA.**

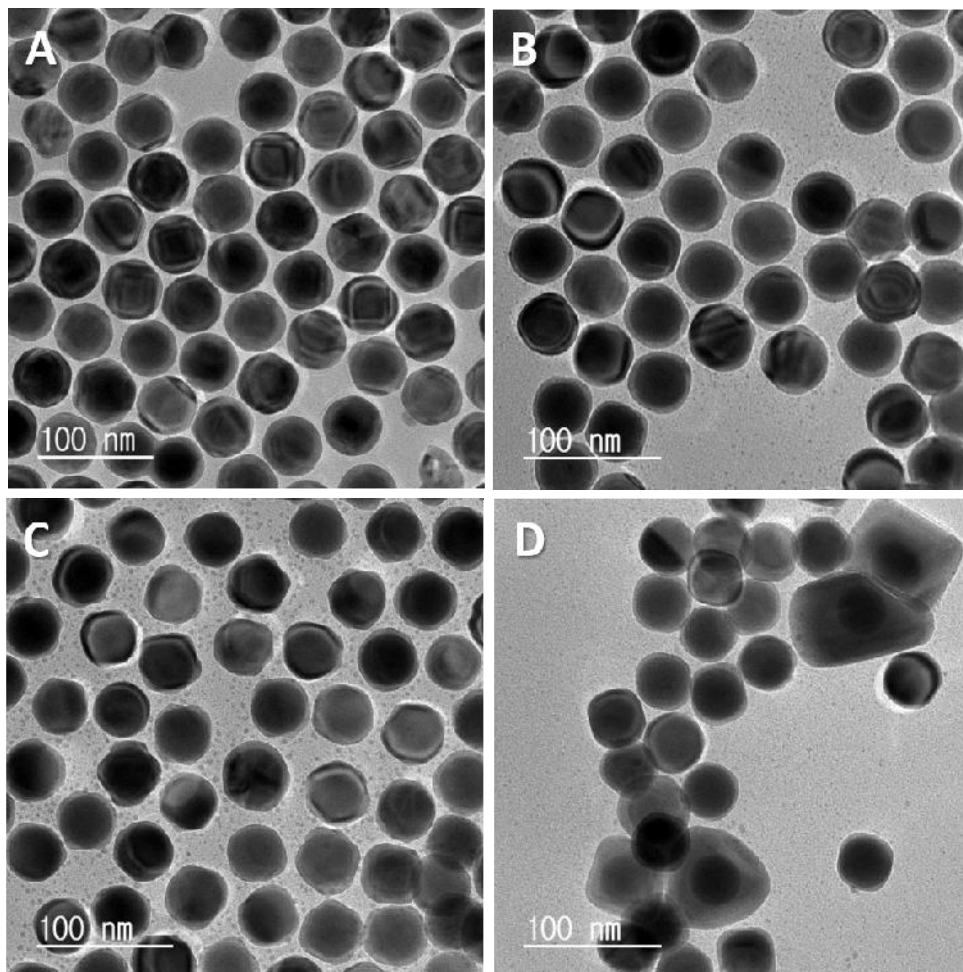


**Figure 2.4**  $\text{NH}_4\text{OH}$  concentration and  $\text{NaOH}$  effects on the silver shell formation (A)

0.1 M  $\text{NH}_4\text{OH}$  (B) 0.1 M  $\text{NaOH}$  (C) stock  $\text{NH}_4\text{OH}$  (D) without  $\text{NH}_4\text{OH}$

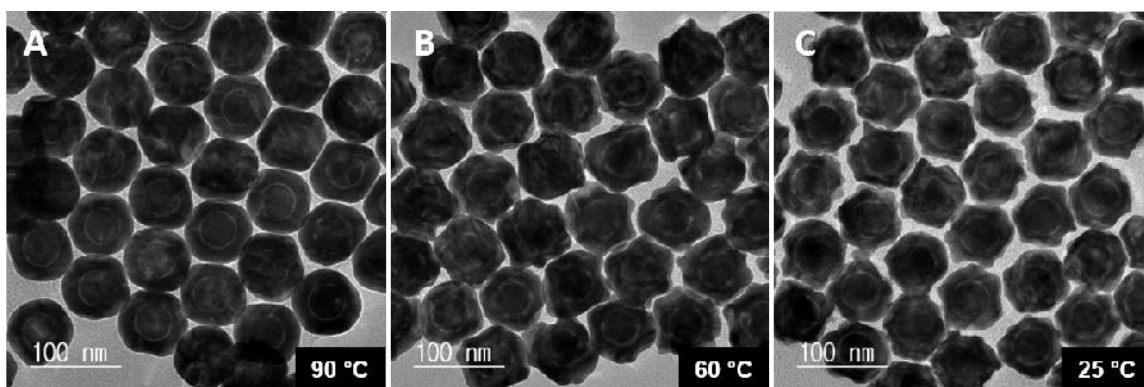


**Figure 2.5** Temperature effect on the Au shell morphology during galvanic/reduction reaction (A) 90 °C, (B) 60 °C, (C) 25 °C.

some of the SID procedures.<sup>[35]</sup> Briefly, Ag and Au were rapidly reduced simultaneously on the core with excess  $\text{NH}_4\text{OH}$  in a small reaction volume followed by treatment with  $\text{Fe}(\text{NO}_3)_3$  to selectively remove Ag and form a rough intragap and polycrystalline shell. The difference between the nm-scale shapes of the intragaps of each synthesized nanostructure was investigated by high-angle annular dark-field scanning transmission electron microscopy (HAADF-STEM) and high-resolution transmission electron microscopy (HR-TEM). HR-TEM and HAADF-STEM images of SSINs showed a clear boundary line with a smooth and uniform gap size (Figure 2.6A). In contrast, for the intragap in PRINs, an uneven dark and bright signal was observed (Figure 2.6B), indicating that the gap size and shape were not constant. Using Cs-corrected HR-TEM images and via their selected-area electron diffraction (SAED) pattern analysis, the crystallinity of each nanostructure shell was analyzed. Figure 2.6C depicts a magnified CS-TEM image of SSINs in the shell region and the corresponding SAED pattern with bright spots. These results demonstrated that during the growth of the Ag shell and GRR, the Ag shell epitaxially grew and the Ag atoms in the shell were replaced by Au atoms while maintaining the lattice because of a low degree of lattice mismatch between Au and Ag. More specifically, the SAED pattern indicated that the surfaces preferentially grew along the face-centered cubic (220) and (420) facets. In the cases of PRINs, due to the fast co-reduction rate, a multi-grain boundary (white arrow) was noticed in the magnified shell region (Figure 2.6D). Furthermore, an irregular ring-like spotty pattern around the beam block was observed in the SAED pattern, implying the formation of a

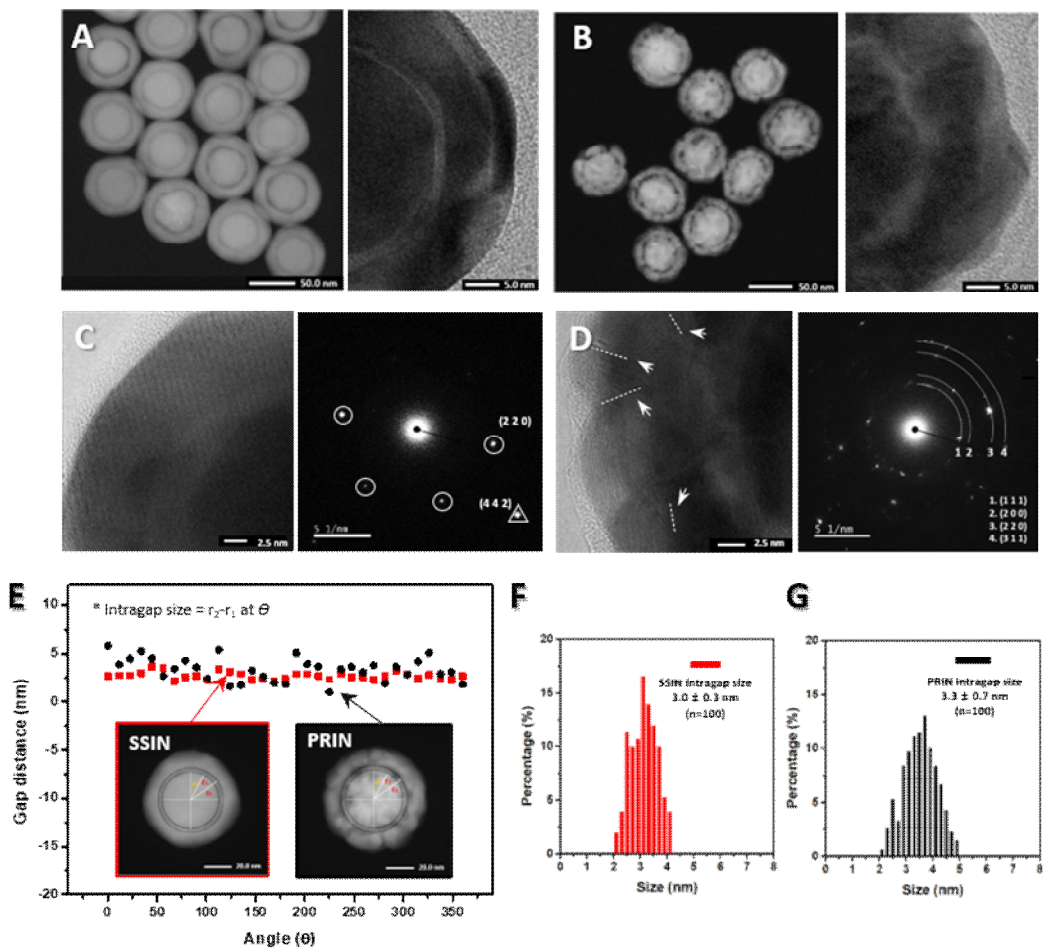


**Figure 2.6 Structural analysis singlecrystalline smooth intragap nanoparticles (SSINs) and polycrystalline rough intragap nanoparticles (PRINs).** HAADF-STEM and HR-TEM images of (A) SSINs, (B) PRINs shows smooth and rough intragap. HR-TEM image and Selective area electron diffraction (SAED) pattern of shell region showing the singlecrystalline structure of (C) SSINs and polycrystalline structure of (D) PRINs. (E) The intragap size ( $r_2-r_1$ ) distribution at the specific rotation angle in single nanoparticle. Intragap size distributions of 100 particles of (F) SSINs and (G) PRINs which were analyzed from the TEM images.

polycrystalline shell. To quantitatively represent the roughness of the intragap, the size of the gap was measured. For individual nanoparticles, the intragap distance ( $r$ ) was defined and measured as the difference between the distances from the center to the inner shell ( $r_2$ ) and from the center to the core surface ( $r_1$ ) at a specific angle ( $\theta$ ) ( $r = r_2 - r_1$  at  $\theta$ ) (Figure 2.6E). For SSINs,  $r$  demonstrated a relatively constant value from an average interval of 3 nm to a difference of 0.5–1 nm. For PRINs,  $r$  significantly deviated from an average interval of approximately 3 nm to a difference of 1–5 nm. Additionally, 100  $r$  values were calculated for each particle, and SSINs and PRINs exhibited average intragaps of 3 and 3.3 nm and the standard deviations of 10.0 and 21.2%, respectively (Figures 2.6F and G). This indicated that SSINs formed a super-uniform gap with low internal gap size deviation (Figure 2.7). Structural uniformities of the SSINs were also revealed by the scattering spectra. Before obtaining the scattering spectra, the sizes of the core, gap, and shell were adjusted to similar levels to observe the changes in the optical properties of SSINs with respect to the roughness of the intragap (Figure 2.8). Moreover, via the mapping of Au and Ag by energy-dispersive X-ray spectroscopy, we confirmed that Ag removed from both nanoparticles was evenly distributed in the shell region (5.5% for PRINs and 8.8% for SSINs) (Figure 2.9). Subsequently, we acquired light scattering images and spectra of individual nanoparticles using dark-field (DF) microscopy. Both SSINs and PRINs exhibited consistent green scattering signals (Figures 2.10A and B), respectively. In Figures 2.10C and D, all the single-particle scattering signals corresponding to the DF images of

SSINs and PRINs demonstrated maximum peaks between 500 and 600 nm (dotted line), respectively. Nevertheless, in the scattering spectra of six individual PRINs, new and inconsistent extinction shoulder peaks at approximately 700–800 nm were observed (Figure 2.10C). The difference between the maximum shoulder peaks at long wavelengths for the intragap nanoparticles is mainly due to the irregular factors of the intragap.<sup>[50]</sup> In contrast, the spectra of five individual SSINs were highly uniform with no significant new peaks at longer wavelengths (Figure 2.10D). This trend was also noticed in solution-based ensemble extinction spectra, in which SSINs demonstrated a narrow peak in the longer wavelength region, whereas the PRINs exhibited a broad shoulder peak (Figures 2.10E and F). These scattering spectra results revealed high homogeneities of SSIN structures. Furthermore, we emphasized that structural and spectral reproducibility can be achieved for SSINs by measuring every five different batches of SSIN and PRIN solutions and comparing their solution-based extinction spectra. Both samples exhibited the strongest solution-based SERS signals when a 785 nm laser source was used as compared to the cases when a 514 nm or 633 nm laser source was employed (Figures 2.11A–C). When the solution-based SERS intensity was measured as a function of particle concentration, high linearity was noticed for both samples because during ensemble SERS measurements, signal differences due to different shapes of individual particles are generally averaged (Figure 2.11D). Therefore, particle concentration does not substantially affect the interpretation of results in a biomolecule detection system even if there is a significant difference between the

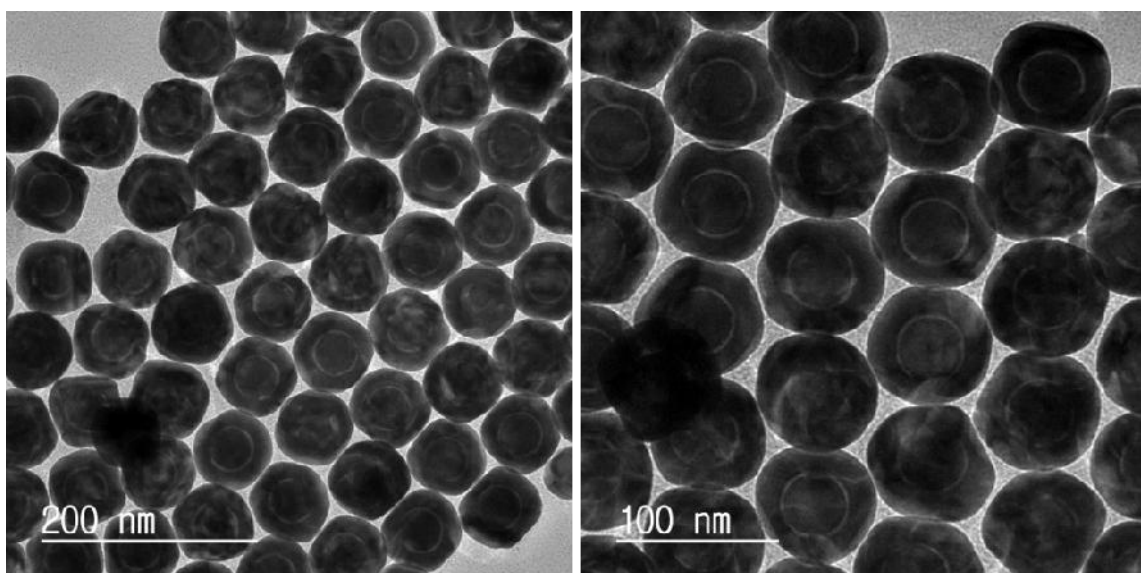


**Figure 2.7 TEM images of SSINs**

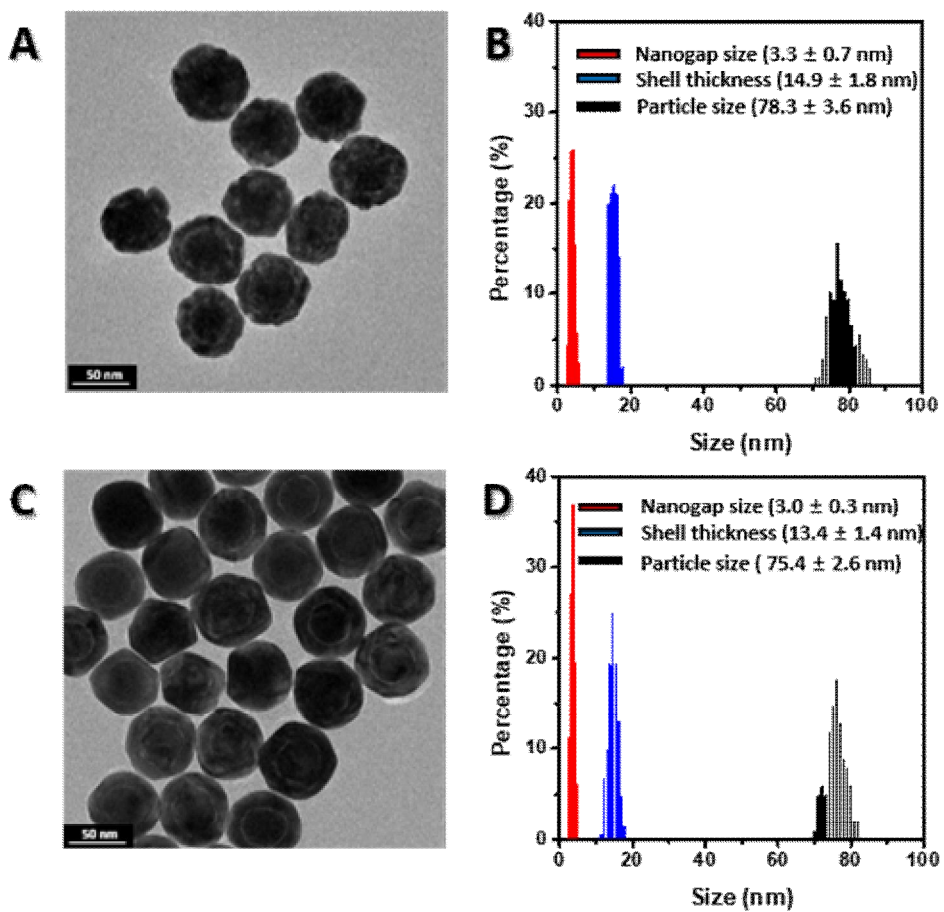


**Figure 2.8** Nanogap size, shell thickness, and particle size distributions of (A-B) PRINs and (C-D) SSINs. The TEM images of 100 particles were analyzed.

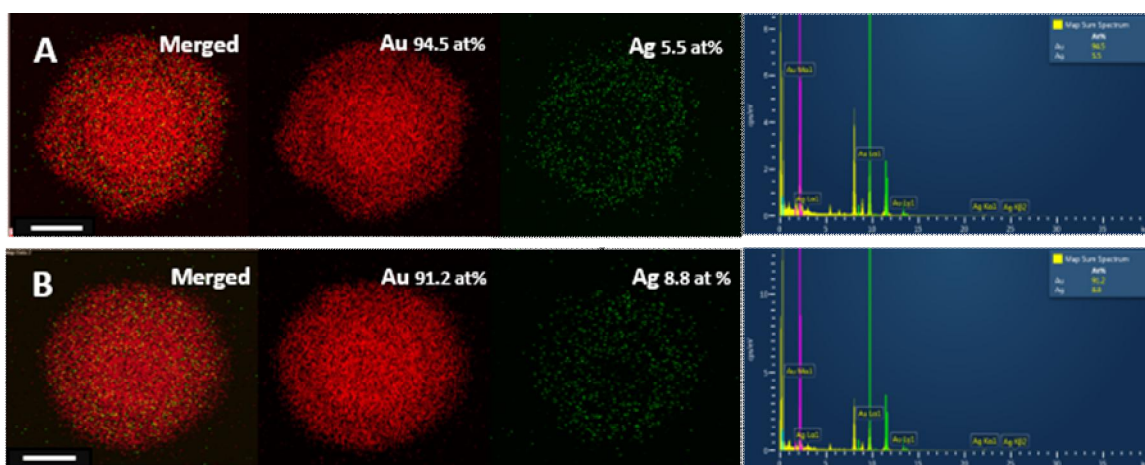


**Figure 2.9** EDX elemental mapping and atomic % of Au and Ag (A) PRINs (B) SSINs. The scale bar is 20 nm.

results obtained using different SERS probes, specifically when a sample at high concentration needs to be detected. However, when the detection concentrations of biomolecules are lower, the reproducibility and uniformity of SERS from particle to particle and the corresponding signals become more critical. Thus, performing single-particle level analysis for different particles and comparing the obtained results is necessary to determine whether the particles are suitable for single-particle level detection. To the best of our knowledge, to date, the SERS is amplified in proportion to the fourth power of the near-field when the Raman-active material is located in a region where the near-field, called a hot spot, is strongly formed. Near-field enhancement is known as the most important mechanism of the SERS. Several factors, such as shape, composition, distance, and type of the dielectric material, influence the near-field distribution. In this study, we focused on the structural aspects of particles and investigate the effects on near-field distribution. For quantitative understanding of how the roughness inside the gap affects the SERS EF distribution, we computationally modeled the PRINs and SSINs and conducted classical electrodynamic calculations (Figure 2.12A). SSINs were modeled to have a uniform thickness of the gap and the radius of curvature was the same throughout. Because of no structural differences at any locations in the gap region, SSINs are expected to cause less variation in the SERS EF. Moreover, the PRIN model was generated by inducing deformation in the SSINs. The average gap thickness for the PRINs was the same as that in the case of SSINs; however, the gap thickness was larger in concave regions and smaller in convex regions. Contrary

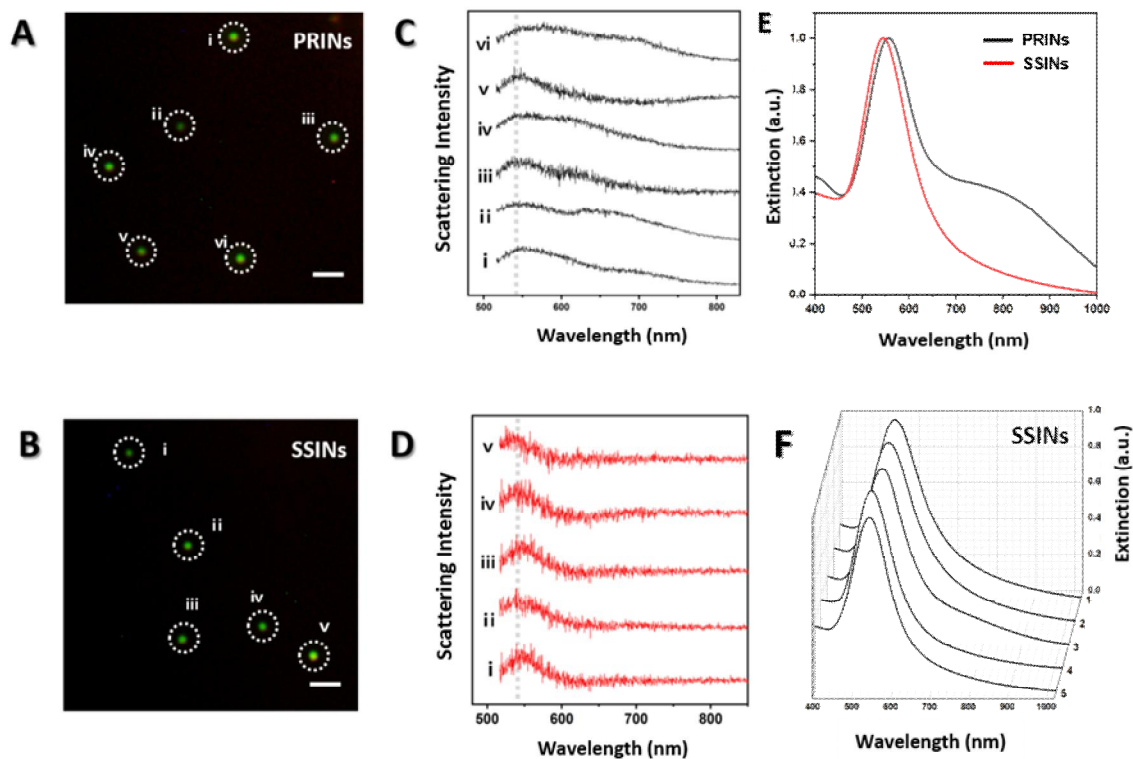


**Figure 2.10 Single-particle scattering analysis and ensemble UV-Vis extinction spectra of PRINs and SSINs.** Dark-field microscope images of (A) PRINs and (B) SSINs and corresponding single-particle scattering spectra of (C) PRINs and (D) SSINs. We acquired scattering spectra with an exposure time of 3 s. (E) Ensemble UV-Vis extinction spectra of as-synthesized PRINs and SSINs solution. (F) The solution extinction spectra from five different batches of SSINs solutions.

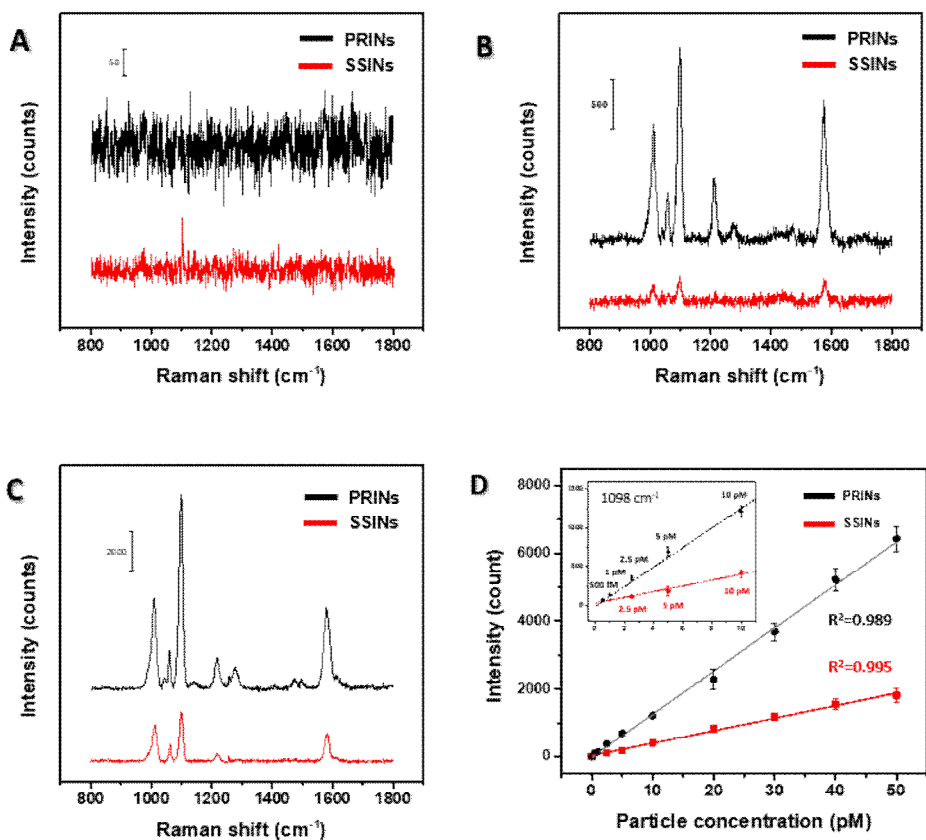


**Figure 2.11 Solution-based SERS spectra of PRINs and SSINs.** SERS spectra of NPs with (A) 514 nm (5 mW), (B) 633 nm (3 mW) (C) 785 nm (6 mW) laser with and acquisition time of 10 s. All the measurements were performed with 100 pM of particles. (D) Particle concentration-dependent changes in SERS signal intensity with 785 nm laser source.

Furthermore, if protrusions on the core and inner surfaces of the shell are adjacent, the to the case of SSINs, the local shape of the gap varied from location to location in the case of PRINs; consequently, the resulting SERS EFs of SSINs and PRINs were significantly different. Protrusions gap thickness becomes smaller, which generates a considerably stronger electric field.<sup>[51]</sup> The synergistic effect of the protrusion and smaller gap contributes the most to the SERS enhancement. Nevertheless, because each PRIN has a different number of “hotter spots”, the PRINs yield larger average enhancement and induce larger variance in EF. These results suggest that a precisely controlled smooth intragap is critical for producing a uniformly enhanced electromagnetic field, resulting in narrow SERS signal distribution. To experimentally prove this effect, we analyzed the SERS spectrum of each nanoparticle at the single-particle level using atomic force microscopy (AFM)-correlated Raman spectroscopy (Figure 2.12B-D). The SERS spectra of 200 individual particles were measured, and the peak intensity was acquired at 1098  $\text{cm}^{-1}$  (Figure 2.13). Note that the SSINs produced uniform and reproducible single-particle SERSs. The estimated EFs for single PRIN and SSIN were  $1.1 \times 10^7$ – $1.2 \times 10^9$  and  $1.6 \times 10^7$ – $1.7 \times 10^8$ , respectively (Figure 3B). Importantly, the average SERS value was higher for PRINs (average EF: ca.  $3.2 \times 10^7$  for SSINs and ca.  $1.8 \times 10^8$  for PRINs); nevertheless, the relative standard deviations of EFs for SSINs were 3.3%, which were smaller than those for PRINs (4.9%). Single-particle polarization plots of the SERS intensity results indicate that the EFs of SSINs are narrowly distributed not only between particles, but also with structural uniformity within nanoparticles. After the polarized

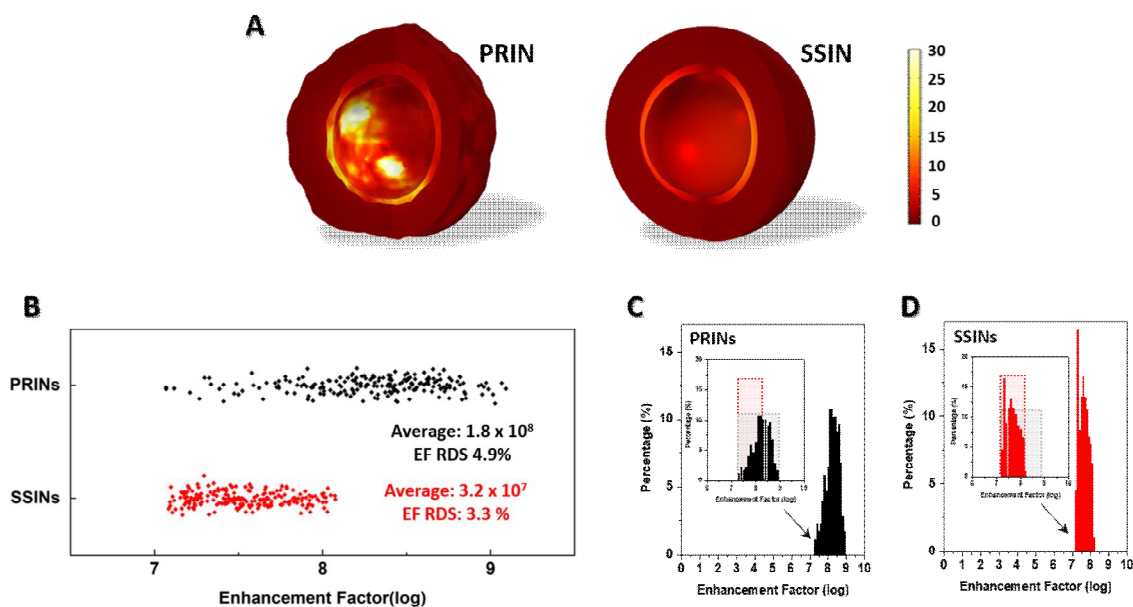


**Figure 2.12 Theoretical calculation and SERS enhancement factor (EF) distributions from AFM-correlated Raman spectroscopy-based single-particle analysis.** (A) Calculated electric near-field distributions of each nanoparticle with different intragap morphologies. (B) SERS EF distribution at  $1098\text{ cm}^{-1}$  of each of 200 individual nanoparticles and EF distribution plot as a percentage in (C) PRINs and (D) SSINs, respectively. The excitation wavelength is 785 nm.

laser was incident on a single particle, an SERS signal was obtained, which was plotted with respect to the rotation angle (Figure 2.14). When the polarized laser was incident on different single PRINs, the SERS signal fluctuated with respect to the rotation angle (Figure 2.14A). In contrast, for single SSINs, a very uniform SERS signal was noticed irrespective of the rotation angle (Figures 2.14B). To achieve high spectral reproducibility, the physical configuration of the hot spot should be precisely controlled and should be resistant to structural deformation during laser irradiation. Generally, a photostability test is conducted for a solution-based sample. Nevertheless, in the cases of low-concentration detection systems, the sample is sometimes measured in the dry state on the substrate. In these systems, considering the stability of the sample in the dry state is also essential as the ambient temperature originating from laser exposure rapidly increases in the dry state than that in the solution state. Therefore, we continuously irradiated the single particle with a laser and examined the photostability of the intragap hotspot via AFM-Raman spectroscopy (Figure 2.15). At first, to ensure the measurement of individual nanoparticles, we acquired the AFM topography image and the Rayleigh scattering image and confirmed that the particles did not overlap (Figures 2.15A and B). Then, we subjected the particles to continuous laser irradiation for 3630 s, obtained spectra at 30 s intervals, and arranged all the spectra in a row (Figures 2.15C-F). Additionally, we quantified the change in the relative value of the SERS signal at a specific time ( $I_{1100(t)}$ ) versus in the first 30s ( $I_{1100(30)}$ ) at  $1098\text{ cm}^{-1}$  during the measurement time ( $I_{1100(t)}/I_{1100(30)}$ , Figures 2.15E and F). The intensity of the relative SERS signal of

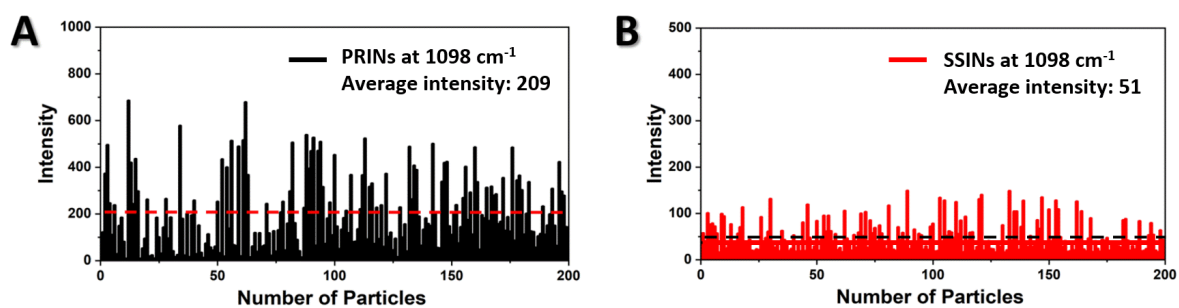
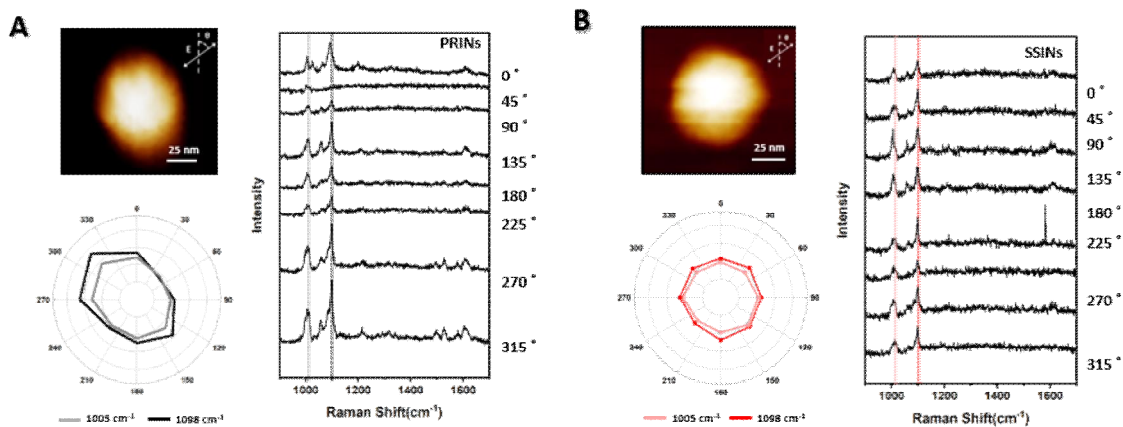


Figure 2.13 SERS intensity for 200 single nanoparticles of (A) PRINs and (B) SSINs.



**Figure 2.14 AFM-correlated Raman spectroscopic result and corresponding single-particle SERS analysis.** Magnified AFM image of a single (A) PRIN and (B) SSIN. SERS spectra and polarization-resolved plot at  $1005\text{ cm}^{-1}$  and  $1098\text{ cm}^{-1}$  with respect to a rotation angle ( $\Theta$ ), respectively.

PRINs increased up to four times during the measurement and substantially fluctuated, whereas that in the case of SSINs remained relatively constant until the end. This phenomenon is attributed to the change in the structures of nanoparticles when the unstable nanoscale protrusion of the intragap is exposed to a strong electromagnetic field.

## **2.4 Conclusion**

In conclusion, herein, we developed a precisely controlled, highly uniform intragap nanostructure in high yield, demonstrated uniform electric field distribution in the intragap region, and achieved analogous enhancement of SERS signals for individual particles. Our results suggest that a highly uniform intragap morphology is crucial for the reproducibility and stability of SERS spectra at the single-particle level. We again emphasize the importance of the strength of highly controlled intragap structures for spectral reproducibility and stability, and we believe that the significantly advanced results and findings reported in our study will accelerate the development of practical applications of SERS such as in sensing and quantitative nanoplasmonic.

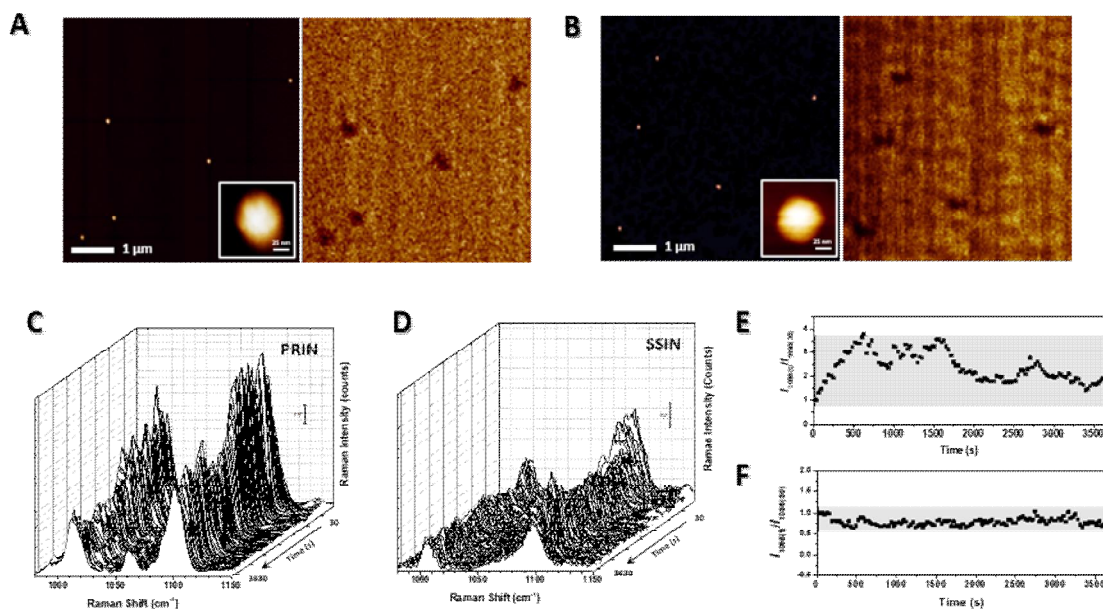


**Figure 2.15 Time-dependent SERS signal of a single nanoparticle for hotspot stability test.** (A and B) Topographical matching of AFM image (left) and Rayleigh scattering image (right) for (A) PRINs and (B) SSINs. The inset shows a magnified AFM image of a nanoparticle. (C and D) Time-dependent Raman profiles of a single nanoparticle. (E and F) SERS spectra of single nanoparticle for 30, 1800, and 3630 s and time-dependent plots of the  $I_{1104(t)}/I_{1104(30)}$  ratio. All the spectra were measured using 785 nm excitation laser source.

## 2.5 Reference

- [1] J. Langer, D. J. de Aberasturi, J. Aizpurua, R. A. Alvarez-Puebla, B. Auguie, J. J. Baumberg, G. C. Bazan, S. E. J. Bell, A. Boisen, A. G. Brolo, J. Choo, D. Ciolla-May, V. Deckert, L. Fabris, K. Faulds, F. Javier García de Abajo, R. Goodacre, D. Graham, A. J. Haes, C. L. Haynes, C. Huck, T. Itoh, M. Käll, J. Kneipp, N. A. Kotov, H. Kuang, E. C. Le Ru, H. K. Lee, J. F. Li, X. Y. Ling, S. A. Maier, T. Mayerhöfer, M. Moskovits, K. Murakoshi, J. M. Nam, S. Nie, Y. Ozaki, I. Pastoriza-Santos, J. Perez-Juste, J. Popp, A. Pucci, S. Reich, B. Ren, G. C. Schatz, T. Shegai, S. Schlücker, L. L. Tay, K. George Thomas, Z. Q. Tian, R. P. van Duyne, T. Vo-Dinh, Y. Wang, K. A. Willets, C. Xu, H. Xu, Y. Xu, Y. S. Yamamoto, B. Zhao, L. M. Liz-Marzán, *ACS Nano* **2020**, *14*, 28.
- [2] S. Laing, L. E. Jamieson, K. Faulds, D. Graham, *Nat. Rev. Chem.* **2017**, *1*, 1.
- [3] S.-Y. Ding, J. Yi, J.-F. Li, B. Ren, D.-Y. Wu, R. Panneerselvam, Z.-Q. Tian, *Nat. Rev. Mater.* **2016**, *1*, 16021.
- [4] J. M. Nam, J. W. Oh, H. Lee, Y. D. Suh, *Acc. Chem. Res.* **2016**, *49*, 2746.
- [5] J. M. Kim, C. Lee, Y. Lee, J. Lee, S. J. Park, S. Park, J. M. Nam, *Adv. Mater.* **2021**, *33*, DOI 10.1002/adma.202006966.
- [6] D. K. Lim, K. S. Jeon, J. H. Hwang, H. Kim, S. Kwon, Y. D. Suh, J. M. Nam, *Nat. Nanotechnol.* **2011**, *6*, 452.
- [7] Y. Chen, Y. Xianyu, X. Jiang, *Acc. Chem. Res.* **2017**, *50*, 310.
- [8] J. W. Oh, D. K. Lim, G. H. Kim, Y. D. Suh, J. M. Nam, *J. Am. Chem. Soc.* **2014**, *136*, 14052.
- [9] H. Lee, S. H. Nam, Y. J. Jung, S. Park, J. M. Kim, Y. D. Suh, D. K. Lim, *J. Mater. Chem. C* **2015**, *3*, 10728.

- [10] J. Shen, X. Jiang, L. Xu, Z. Ge, Q. Li, B. Song, L. Wang, S. Song, *ACS Appl. Nano Mater.* **2019**, *2*, 3501.
- [11] W. Zhou, Y. F. Tian, B. C. Yin, B. C. Ye, *Anal. Chem.* **2017**, *89*, 6120.
- [12] B. Zhao, J. Shen, S. Chen, D. Wang, F. Li, S. Mathur, S. Song, C. Fan, *Chem. Sci.* **2014**, *5*, 4460.
- [13] Y. Wang, K. Sentosun, A. Li, M. Coronado-Puchau, A. Sánchez-Iglesias, S. Li, X. Su, S. Bals, L. M. Liz-Marzán, *Chem. Mater.* **2015**, *27*, 8032.
- [14] Y. Zhang, Y. Gu, J. He, B. D. Thackray, J. Ye, *Nat. Commun.* **2019**, *10*, DOI 10.1038/s41467-019-11829-y.
- [15] Y. Gu, C. He, Y. Zhang, L. Lin, B. D. Thackray, J. Ye, *Nat. Commun.* **2020**, *11*, 1.
- [16] L. Lin, Q. Zhang, X. Li, M. Qiu, X. Jiang, W. Jin, H. Gu, D. Y. Lei, J. Ye, *ACS Nano* **2018**, *12*, 6492.
- [17] N. Gandra, S. Singamaneni, *Adv. Mater.* **2013**, *25*, 1022.
- [18] B. N. Khlebtsov, N. G. Khlebtsov, *J. Phys. Chem. C* **2016**, *120*, 15385.
- [19] J. M. Kim, J. Kim, M. Ha, J. M. Nam, *J. Phys. Chem. Lett.* **2020**, *11*, 8358.
- [20] R. Bardhan, S. Mukherjee, N. A. Mirin, S. D. Levit, P. Nordlander, N. J. Halas, *J. Phys. Chem. C* **2010**, *114*, 7378.
- [21] L. Lin, M. Zapata, M. Xiong, Z. Liu, S. Wang, H. Xu, A. G. Borisov, H. Gu, P. Nordlander, J. Aizpurua, J. Ye, *Nano Lett.* **2015**, *15*, 6419.
- [22] J. Song, B. Duan, C. Wang, J. Zhou, L. Pu, Z. Fang, P. Wang, T. T. Lim, H. Duan, *J. Am. Chem. Soc.* **2014**, *136*, 6838.
- [23] J. Zhou, Q. Xiong, J. Ma, J. Ren, P. B. Messersmith, P. Chen, H. Duan, *ACS Nano* **2016**, *10*, 11066.

- [24] L. Lin, H. Gu, J. Ye, *Chem. Commun.* **2015**, *51*, 17740.
- [25] J. Li, Z. Zhu, B. Zhu, Y. Ma, B. Lin, R. Liu, Y. Song, H. Lin, S. Tu, C. Yang, *Anal. Chem.* **2016**, *88*, 7828.
- [26] Y. Zhao, F. Zheng, W. Ke, W. Zhang, L. Shi, H. Liu, *Anal. Chem.* **2019**, *91*, 7162.
- [27] Z. Zhang, S. Zhang, M. Lin, *Chem. Commun.* **2013**, *49*, 8519.
- [28] G. Bhattacharjee, S. Majumder, D. Senapati, S. Banerjee, B. Satpati, *Mater. Chem. Phys.* **2020**, *239*, DOI 10.1016/j.matchemphys.2019.122113.
- [29] J. E. Park, S. Kim, J. Son, Y. Lee, J. M. Nam, *Nano Lett.* **2016**, *16*, 7962.
- [30] L. Ma, Y. L. Chen, D. J. Yang, H. X. Li, S. J. Ding, L. Xiong, P. L. Qin, X. B. Chen, *Nanoscale* **2020**, *12*, 4383.
- [31] W. Zhang, M. Rahmani, W. Niu, S. Ravaine, M. Hong, X. Lu, *Sci. Rep.* **2015**, *5*, 8382.
- [32] H. T. Ngo, E. Freedman, R. A. Odion, P. Strobbia, A. S. De Silva Indrasekara, P. Vohra, S. M. Taylor, T. Vo-Dinh, *Sci. Rep.* **2018**, *8*, 1.
- [33] A. Jaiswal, L. Tian, S. Tadepalli, K. K. Liu, M. Fei, M. E. Farrell, P. M. Pellegrino, S. Singamaneni, *Small* **2014**, *10*, 4287.
- [34] M. Kim, S. M. Ko, J. M. Kim, J. Son, C. Lee, W. K. Rhim, J. M. Nam, *ACS Cent. Sci.* **2018**, *4*, 277.
- [35] F. Benz, M. K. Schmidt, A. Dreismann, R. Chikkaraddy, Y. Zhang, A. Demetriadou, C. Carnegie, H. Ohadi, B. De Nijs, R. Esteban, J. Aizpurua, J. J. Baumberg, *Science (80-. )*. **2016**, *354*, 726.
- [36] C. Carnegie, J. Griffiths, B. De Nijs, C. Readman, R. Chikkaraddy, W. M. Deacon, Y. Zhang, I. Szabó, E. Rosta, J. Aizpurua, J. J. Baumberg, *J. Phys. Chem. Lett.* **2018**, *9*, 7146.
- [37] H. H. Shin, G. J. Yeon, H. K. Choi, S. M. Park, K. S. Lee, Z. H. Kim, *Nano Lett.* **2018**, *18*,

262.

- [38] M. Urbietta, M. Barbry, Y. Zhang, P. Koval, D. Sánchez-Portal, N. Zabala, J. Aizpurua, *ACS Nano* **2018**, *12*, 585.
- [39] J. E. Park, Y. Jung, M. Kim, J. M. Nam, *ACS Cent. Sci.* **2018**, *4*, 1303.
- [40] J. Kim, K. Sim, S. Cha, J. W. Oh, J. M. Nam, *J. Raman Spectrosc.* **2021**, *52*, 375.
- [41] Y. Wang, B. Yan, L. Chen, *Chem. Rev.* **2013**, *113*, 1391.
- [42] Y. Zheng, X. Zhong, Z. Li, Y. Xia, *Part. Part. Syst. Charact.* **2014**, *31*, 266.
- [43] M. Kim, S. M. Ko, J. M. Kim, J. Son, C. Lee, W. K. Rhim, J. M. Nam, *ACS Cent. Sci.* **2018**, *4*, 277.
- [44] H. Lee, J. H. Lee, S. M. Jin, Y. D. Suh, J. M. Nam, *Nano Lett.* **2013**, *13*, 6113.
- [45] W. Song, W. Li, Y. Cheng, H. Jia, G. Zhao, Y. Zhou, B. Yang, W. Xu, W. Tian, B. Zhao, *J. Raman Spectrosc.* **2006**, *37*, 755.
- [46] W. Song, Y. Wang, B. Zhao, *J. Phys. Chem. C* **2007**, *111*, 12786.
- [47] G. Gramlich, J. Zhang, W. M. Nau, *J. Am. Chem. Soc.* **2002**, *124*, 11252.
- [48] Y. C. Tsao, S. Rej, C. Y. Chiu, M. H. Huang, *J. Am. Chem. Soc.* **2014**, *136*, 396.
- [49] X. Xia, Y. Wang, A. Ruditskiy, Y. Xia, *Adv. Mater.* **2013**, *25*, 6313.
- [50] Y. Xia, X. Xia, H.-C. Peng, *J. Am. Chem. Soc.* **2015**, 150528140910003.
- [51] J. H. Lee, J. M. Nam, K. S. Jeon, D. K. Lim, H. Kim, S. Kwon, H. Lee, Y. D. Suh, *ACS Nano* **2012**, *6*, 9574.

## **Chapter 3.**

# **Kinetically Controlled Synthesis of Au-Ag Alloy Knotted Nano Ball(KNB): Enhanced Ethanol Electro-oxidation**

### 3.1 Introduction

Au was considered non-catalytic until 1987 when Haruta et al. first reported that a cluster of Au smaller than 5 nm can be applied as a catalyst if stabilized on an oxide substrate.<sup>[1]</sup> Since Au clusters are unstable and suffer from dispersion problems; therefore, reactions containing these clusters always require oxide supports. However, these supports affect the catalytic activity, the catalytic mechanism of the Au cluster alone cannot be determined.<sup>[2-4]</sup> However, dealloy-based Au nanoporous films have been proven to be stable catalysts that do not require oxide support despite the size of a single Au ligament being 30 nm or higher.<sup>[5-8]</sup> Since then, the intrinsic mechanism of catalysis in Au surface provided by unsupported Au nanoporous catalysts in chemical reactions was investigated in several studies. The catalysis appeared to be associated with the large surface area and under-coordinated surface atoms in the highly curved ligaments in the nanoporous Au catalyst.<sup>[9,10]</sup> Specifically, the fraction of surface atoms with low coordination numbers on the Au nanoporous ligaments was much larger than that of truncated octahedral Au particles with radii of curvature equivalent to those of Au nanoporous ligaments.<sup>[11]</sup> This high density of under-coordinated surface atoms arising from the steps and kinks structure explained the excellent activity of the Au nanoporous catalysts.

Existing Au nanoporous materials are mostly made of one or two-dimensional bulk materials or thin films, and their synthesis procedure involves alloying and dealloying reactions that require sintering and vacuum conditions.<sup>[12-14]</sup> Zero-dimensional (0D) porous nanoparticles have a higher surface-to-volume ratio than one and two-

dimensional Au nanoporous materials, and the ligaments bend substantially within a small volume, thereby providing several active sites on the surface. However, the synthesis of 0D Au porous nanoparticles also entails an alloying-dealloying reaction.<sup>[15–17]</sup> This reaction should be performed at a high activation temperature, in which Au and Ag are usually diffused. In particular, owing to the harsh synthesis environment for 0D nanoparticles, supporting material such as a silica shell<sup>[15]</sup> or substrate<sup>[17]</sup> is essential for maintaining their structure and preventing aggregation. Furthermore, the multiple synthesis steps are energy-consuming and involve complicated experimental conditions that hinder the formation of porous 0D Au nanoparticles.

In general, in Au-Ag alloy nanoparticles, Ag is etched through the dealloying process and the remaining Au locally forms clusters that result in ligaments.<sup>[18]</sup> Although Au and Ag have similar lattice constants (0.408 nm for Au and 0.409 nm for Ag with a lattice mismatch parameter of approximately 0.2%),<sup>[19]</sup> the reduction potentials of Au and Ag are greatly influenced by the synthesis conditions. In particular, the reduction rates of Au and Ag are seriously affected by the synthesis environment, such as the pH of the solution, choice of surfactant, and metal and halide affinity. Thus, synthesizing Au-Ag alloy nanoparticles at room temperature is challenging.<sup>[20,21]</sup> In addition, the difference in electrical reduction potential between Au and Ag ( $\text{AuCl}_4^-/\text{Au}$ : 0.99 V vs. standard hydrogen electrode (SHE) and  $\text{Ag}^+/\text{Ag}$ : 0.80 V vs. SHE) results in the galvanic replacement reaction being unavoidable and controlling the morphology difficult.<sup>[22]</sup>

## 3.2 Experimental Section

### Reagents

Gold(III) chloride trihydrate ( $\text{HAuCl}_4 \cdot 3\text{H}_2\text{O}$ ,  $\geq 99.9\%$ ), silver nitrate ( $\text{AgNO}_3$ , 99.9999%), ammonium hydroxide solution ( $\text{NH}_4\text{OH}$ , 28.0-30.0%  $\text{NH}_3$  basis), L-ascorbic acid (AA,  $\geq 99.0\%$ ), iron(III) nitrate nonahydrate ( $\text{Fe}(\text{NO}_3)_3 \cdot 9\text{H}_2\text{O}$ ,  $\geq 98.0\%$ ), potassium hydroxide ( $\text{KOH}$ ,  $> 90\%$ ) and lead(II) nitrate ( $\text{Pb}(\text{NO}_3)_2$ ) were purchased from Sigma-Aldrich (St. Louis, MO, USA). Cetyltrimethylammonium chloride (CTAC) was purchased from Tokyo Chemical Industry Co., Ltd. (Tokyo, Japan). Sodium bromide ( $\text{NaBr}$ ,  $\geq 99.0\%$ ), ethyl alcohol ( $\text{CH}_3\text{OH}$ , anhydrous, 99.9%) and sulfuric acid ( $\text{H}_2\text{SO}_4$ , 95-98 %) were purchased from DAEJUNG Chemicals & Metals Co. (Siheung, Gyeonggi, Korea). All the chemical reagents were used as received without further purification. NANOpure water (Millipore, Milli-Q 18.2  $\text{M}\Omega \cdot \text{cm}$ ) was used throughout the experiments.

### Synthesis of 10-nm-sized of gold single-crystalline seed

Gold single-crystalline seeds with a size of 10 nm were synthesized using a seed-mediated growth method. To obtain CTAB-capped Au seeds, an aqueous solutions of CTAB (200 mM, 5 mL) and  $\text{HAuCl}_4 \cdot 3\text{H}_2\text{O}$  (0.5 mM, 5 mL) was at 27 °C under stirring (500 rpm). An ice-cooled aqueous  $\text{NaBH}_4$  solution (10 mM, 0.6 mL) was injected at once into the mixture, and the solution turned brown color. The reaction mixture was further stirred for 3 min at 500 rpm and then incubated at 27 °C for 3 h without agitation. To

synthesize 10-nm-sized Au nanospheres, 50  $\mu\text{L}$  of the CTAB-capped Au seeds were injected into a mixture of CTAC (200 mM, 2 mL) and AA (100 mM, 1.5 mL) solutions. This was followed by the introduction of an aqueous  $\text{HAuCl}_4 \cdot 3\text{H}_2\text{O}$  solution (0.5 mM, 2 mL) into the reaction mixture, which was then stirred for 15 min at 27 °C under magnetic stirring (500 rpm). The final AuNSs solution was washed with DI water by centrifugation at 14,500 rpm for 30 min and then finally kept in a CTAC solution (20 mM, 1 mL) for further use.

### **Synthesis of Au-Ag Alloy Knotted Nano Ball (KNB)**

The Au-Ag Alloy Knotted Nano Ball (KNB) were synthesized using the seed-mediated growth method. To obtain 50 nm sized KNB, an aqueous solution of CTAC (20 mM, 1 mL), 10-nm-sized Au nanospheres (100 pM, 1 mL), aqueous  $\text{AgNO}_3$  solution (1 mM, 304  $\mu\text{L}$ ),  $\text{NH}_4\text{OH}$  stock solution (25  $\mu\text{L}$ ) and aqueous  $\text{HAuCl}_4 \cdot 3\text{H}_2\text{O}$  solution (1 mM, 456  $\mu\text{L}$ ) were sequentially added in 20 mL vial under stirred (500 rpm) at room temperature. Next, L-ascorbic acid (AA) solution (20 mM, 1 mL) was injected into the mixture for and then left for 30 min under continuous stirring (100 rpm). In this step, we adjusted the Au/Ag ratio of Au-Ag alloy nanoparticles by controlling the added volume of precursors (608  $\mu\text{L}$  of  $\text{AgNO}_3$  and 152  $\mu\text{L}$  of  $\text{HAuCl}_4$  solution for  $\text{Au}_{20}\text{Ag}_{80}$  alloy nanoparticles; 152  $\mu\text{L}$  of  $\text{AgNO}_3$  and 608  $\mu\text{L}$  of  $\text{HAuCl}_4$  solution for  $\text{Au}_{60}\text{Ag}_{20}$  alloy nanoparticles). Dealloying reaction was carried out by introducing 2 mL of 100 mM  $\text{Fe}(\text{NO}_3)_3$  solution as a Ag etchant into the same mixture solution above. The resulting

solution was under stirred (500 rpm) at room temperature for 1h, then washed three times with DI water by centrifugation at 8,000 rpm for 10 min, and re-dispersed in DI water.

### **Synthesis of Au core Ag-Au double shell Nanoparticle**

The 50 nm Au core Ag-Au double shell nanoparticle were synthesized through seed-mediated growth with minor change of KNB synthesis method. Briefly an aqueous solution of CTAC (20 mM, 1 mL), 10-nm-sized Au nanospheres (100 pM, 1 mL), NaBr solution (10 mM, 100  $\mu$ L), aqueous AgNO<sub>3</sub> solution (1 mM, 304  $\mu$ L), NH<sub>4</sub>OH solution (25  $\mu$ L) and aqueous HAuCl<sub>4</sub>·3H<sub>2</sub>O solution (1 mM, 456  $\mu$ L) were sequentially added in 20 mL vial. Next, L-ascorbic acid (AA) solution (20 mM, 1 ml) was injected into the mixture under stirred (500 rpm) at room temperature for 10 min and then left for 30 min under continuous stirring. Dealloying reaction was carried out by introducing 2 ml of 100 mM Fe(NO<sub>3</sub>)<sub>3</sub> solution as a Ag etchant into the mixture solution above. The resulting solution was under stirred (500 rpm) at room temperature for 1h, then washed three times with DI water by centrifugation at 8,000 rpm for 10 min, and re-dispersed in DI water.

### **Electrochemical Measurement**

All the electrochemical measurements were performed using a VMP3 multi-functional electrochemical analysis instrument (Bio-Logic, France) at room temperature with a three-electrode system composed of a Pt wire as a counter electrode, Ag/AgCl or Hg/HgO reference electrode and a glassy carbon electrode (GCE) as a working electrode.

Typically, the GCE was polished with alumina slurry and followed by washing with DI water and ethanol before use. 2  $\mu\text{L}$  Colloidal suspensions containing nanoparticle were dropped and air-dried on the pretreated GCEs at room temperature, and then 2  $\mu\text{L}$  of Nafion solution (0.5 wt%) was dropped to hold the NPs and additional dried for 1h at room temperature. The electrochemical active surface area (ECSA) of nanoparticles were estimated using cyclic voltammetry (CV) measurements in  $\text{N}_2$ -saturated 0.5 M  $\text{H}_2\text{SO}_4$  solution at a potential sweep rate of  $50 \text{ mVs}^{-1}$ . The evaluate the electrocatalytic activities of the nanoparticles toward ethanol oxidation, CV measurement were performed in a  $\text{N}_2$ -saturated 0.5 M KOH solution containing 1 M ethanol at a potential sweep rate of  $50 \text{ mVs}^{-1}$ . The measured CV was normalized against the Au mass of the nanoparticles loaded on each electrode. Chronoamperometry (CA) measurements were carried out at 0.2 V (vs. Ag/AgCl) in 0.5 M KOH solution containing 1 M ethanol over a time period of 2000 s. Underpotential deposition of lead (Pb-UPD) measurement were performed in 0.1 M NaOH containing 1 mM  $\text{Pb}(\text{NO}_3)_2$  at  $50 \text{ mVs}^{-1}$ .

## **Characterization**

The structures and compositions of the nanoparticles were characterized by transmission electron microscopy (TEM), high resolution transmission electron microscopic (HR-TEM) and Cs-corrected high resolution transmission electron microscopic (Cs-TEM) using a JEM-F2100 (JEOL), JEM-2100F (JEOL, Japan) and JEM-ARM200F (JEOL), respectively. The elemental maps and line scan profiles of the NPs were obtained using a

EDX system (INCA, Oxford Instruments) coupled with an HR-TEM. For cross section analysis of the nanoparticle, a FIB instrument Helios 650 (FEL) was used. Surface morphology analysis were performed by Field-emission SEM (FE-SEM) measurement using a SM-7800F Prime (JEOL). The UV-vis spectra were acquired using an UV-vis spectrophotometer (HP 8453, Agilent Technologies). Inductively coupled plasma-mass spectrometry (ICP-MS) measurements were employed using a Varian 820-MS (Varian). Binding energy measurements were performed using an X-ray photoelectron spectroscope (Axis HSi, KRATOS Analytical). The lattices parameter of the samples was identified by X-ray powder diffraction (XRD) using SmartLab (Rigaku).

### 3.3 Results and Discussion

In this study, we developed a novel and efficient method for synthesizing Au-Ag alloy nanoparticles, in which the position and distribution of Au and Ag atoms were controlled. This process did not require any N<sub>2</sub> or Ar environments or high-temperature sintering steps because we controlled the difference in the reduction rates of Au and Ag using halide ions during the co-reduction on the seed. The relative position and distribution of the Au atoms in the alloy are important factors in determining the structure of the final product. Therefore, we controlled the relative rates of reduction of Au and Ag, which were simultaneously reduced to a 10 nm Au core based on seed-mediated growth. These alloy nanoparticles can be easily designed and synthesized with a porous or core-hollow shell structure by selectively removing Ag using a subsequent dealloying process at room temperature. The synthesized Au-Ag porous nanoparticles and Au core-hollow shell particles were investigated as Au catalysts in the ethanol oxidation reaction (EOR), and the surface structural effect of the catalytic activity was determined.

Herein, we proposed a method to prepare alloy nanoparticles with controlled Au and Ag atom distributions by adjusting the pH and adding halide ions to the solution. Porous and core-hollow shell nanoparticles were synthesized by dealloying two types of alloy nanoparticles, as schematically shown in Figure 3.1. To synthesize evenly distributed Au-Ag alloy nanoparticles, HAuCl<sub>4</sub>, AgNO<sub>3</sub>, cetyltrimethylammonium chloride (CTAC), and NH<sub>4</sub>OH were mixed with pre-prepared 10 nm Au core seeds, and ascorbic acid was added to reduce Au and Ag precursors simultaneously at 25 °C. The Au@Ag-Au double-

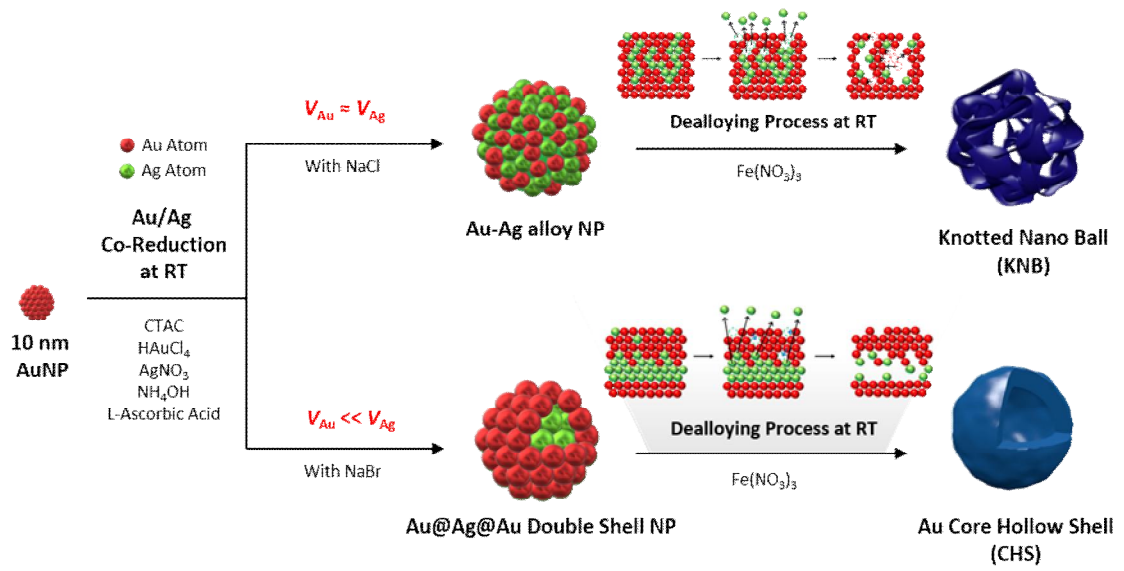


**Figure 3.1 Schematic illustration of the alloying-dealloying-based synthetic strategy for Au-Ag Knotted Nano Ball (KNB) particles and Au core-hollow shell (CHS) nanoparticles.**

shell structure was obtained using the same synthesis procedure as above with the addition of NaBr. After 30 min of incubation,  $\text{Fe}(\text{NO}_3)_3$  was added during the dealloying process without washing. After dealloying, the uniformly distributed Au-Ag alloy nanoparticles possessed a porous structure named knotted nano ball (KNB). An Au core-hollow-shell (CHS) structure was obtained for the Au@Ag-Au double shell. All processes were performed at room temperature for 1.5 h (refer to the Experimental section for more details).

Energy dispersive spectroscopy (EDS) mapping image of the alloy nanoparticles in an intermediate state were obtained to confirm the distribution of Au and Ag atoms in the nanoparticles. According to the EDS mapping image and corresponding elemental line-scan profile of the shell region, the Au and Ag atoms in the Au-Ag alloy nanoparticles were well distributed throughout the shell region (Figures 3.2A and C). In contrast, most Ag atoms existed inside the Au@Ag-Au double-shell nanoparticles and Au atoms were distributed on the outer shell region to form these nanoparticles (Figures 3.2B and D). From the transmission electron microscopy (TEM) images and corresponding selected area electron diffraction (SAED) patterns, the Au-Ag alloy and Au@Ag-Au double-shell nanoparticles were found to be polycrystalline with average sizes of approximately 55 and 57 nm, respectively (Figures 3.2E and F). The facile synthesis of both the particles provided a high yield (Figure 3.3: EDS mapping image with a low magnification). Additionally, we monitored the unique localized surface plasmon resonance (LSPR) peaks of nanoparticles to understand the growth process. Furthermore, time-dependent

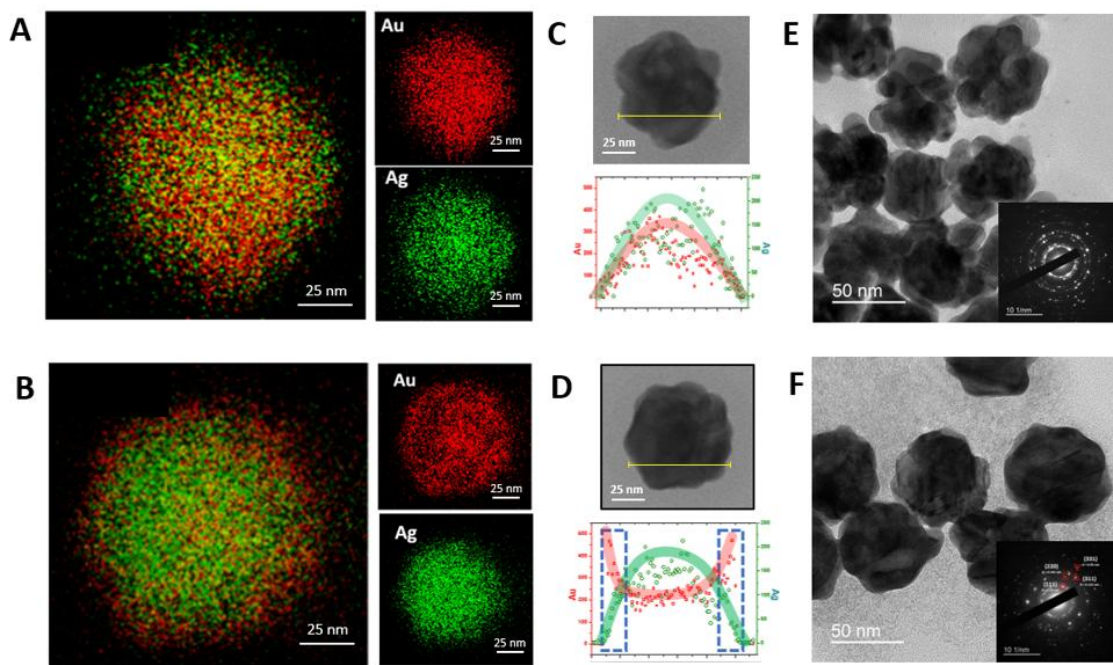


**Figure 3.2 Elemental mapping images** of (A) Au-Ag Alloy NP and (B) Au@Ag-Au double shell NP for each element and merged images Au (red), Ag (green). Scale bars are 25 nm. (C-D) TEM images and EDX line scan profiles across the NP : (C) Au-Ag Alloy NP, (D) Au@Ag-Au double shell NP. (E-F) Low magnification TEM images of (E) Au-Ag Alloy NP and (F) Au@Ag-Au double shell NP. The inset shows a ring shaped SAED pattern, indicating there is a polycrystalline structure

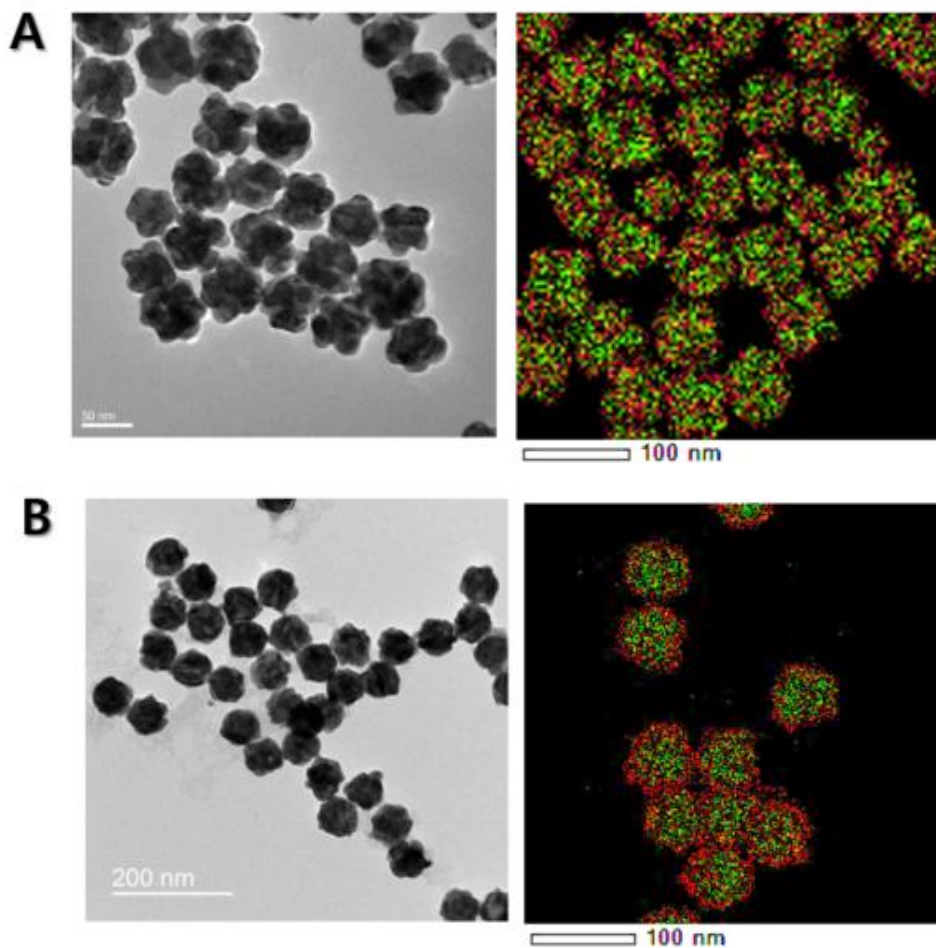


**Figure 3.3** Low magnification EDS of Au-Ag alloy NP and Au@Ag-Au double shell NP. Facile synthesis of both particles were synthesized in a high yield.

ultraviolet-visible (UV-vis) spectra were obtained and monitored during the growth of Au and Ag under each condition at 2s intervals (Figures 3.4A and B). In the precursor solution of the Au-Ag alloy nanoparticles, the strength of the reducing agent was sufficiently high owing to the high pH,<sup>[23]</sup> and the Au and Ag reduction rates were high. Under these conditions, the maximum peak of the LSPR remained constant at approximately 490 nm during the growth. This peak was located in the middle of the Au ( $\lambda = \sim 520$  nm, red) and Ag ( $\lambda = \sim 400$  nm, yellow) absorption bands, and the color of the Au-Ag alloy nanoparticles solution immediately changes from red to orange (Figure 3.4A). This result indicated that the Au and Ag atoms were deposited evenly on the core throughout nucleation and growth. However, for the Au@Ag-Au double-shell nanoparticles, the LSPR band at approximately 400 nm appeared in the initial stage of growth and gradually red-shifted to approximately 500 nm with time (Figure 3.4B). The color of the solution was first yellow and turned reddish-orange a few minutes later. This result indicated sequential growth in the order of Ag to Au, thereby resulting in a core-shell structure.

We separated the Au and Ag shell growth on the core and compared the growth rates of each nanoparticle for an in-depth understanding. We plotted and normalized each maximum LSPR peak of Au and Ag and compared the growth slope until a steady state was reached. Figures 3.4C and D shows a similar growth slope for Au and Ag in the Au-Ag alloy formation condition which reflects Au and Ag simultaneous growth on the Au core. However, the difference in the relative growth slopes of Au and Ag was pronounced

when excess bromide was added (Figure 3.4D). The Au and Ag growth slopes decreased after the addition of bromide ions. These results were observed owing to the high affinity between the Au core surface and bromide ion. The bromide ions partially blocked the Au surface and resulted in a low growth rate in Au and Ag. A further decrease in the Au reduction rate can be explained by the different stabilities of the  $[\text{AuCl}_4]^-$ ,  $[\text{AuBr}_4]^-$  and  $[\text{AuOH}_4]^-$  complexes. In the presence of excess NaBr, excess bromide ions can exchange  $[\text{AuCl}_4]^-$  complexes with  $[\text{AuBr}_4]^-$ , and also, high pH conditions can exchange  $[\text{AuCl}_4]^-$  or  $[\text{AuBr}_4]^-$  complexes with  $[\text{AuOH}_4]^-$ . The  $\text{AuCl}_4^-$  complexes are known to be less stable than  $[\text{AuBr}_4]^-$  and  $[\text{AuOH}_4]^-$  complexes due to the difference in redox potential between and are rapidly reduced ( $\text{AuCl}_4^-/\text{Au}^0$ :  $E^0 = +1.00$  V;  $\text{AuBr}_4^-/\text{Au}^0$ :  $E^0 = +0.85$  V;  $\text{AuOH}_4^-/\text{Au}^0$ :  $E^0 = +0.6$  V).<sup>[24]</sup> Under excessive Cl and Br synthesis conditions, Au complexes can exist as  $[\text{AuCl}_{4-x}(\text{OH})_x]^-$  or  $[\text{AuBr}_{4-x}(\text{OH})_x]^-$  under high pH synthesis conditions. The average value of the standard reduction potential of  $[\text{AuCl}_{4-x}(\text{OH})_x]^-$  is similar to the  $\text{Ag}^+$ , and the average value of the standard reduction potential of  $[\text{AuBr}_{4-x}(\text{OH})_x]^-$  is lower than that of  $\text{Ag}^+$ . For this reason, we argue that the relative growth rates of Ag and Au depend on the Au-halide complex morphology (Fig. 3.4E). In the control experiment, when an alloy nanoparticle was synthesized at a low pH, the growth rate of the nanoparticles was low, and the reaction was complete after 6 h (Figure 3.5). Figures 3.5A–C shows the TEM image and UV-vis spectra, as well as the separately plotted Au and Ag maximum LSPR peaks. Under low-pH conditions, the shapes of the nanoparticles were irregular, and the size deviation was substantial. Analysis of the growth rate using the UV-vis

spectra showed that the Ag growth exhibited a substantially lower slope than that of the Au growth, which was attributed to the slow growth of Ag resulting from the generation of AgCl in the absence of NH<sub>4</sub>OH. Therefore, the high reduction rates of Au and Ag were essential for synthesizing Au-Ag alloy nanoparticles. In addition, the introduction of the halide ions enabled the better design of the relative kinetics of Au and Ag.

Dealloying is a typical corrosion process that involves the selective dissolution of less noble components, in which the remaining component diffuses into the initial crystal lattice of the metal and reorganizes into a three-dimensional network. Therefore, the initial distribution of Au atoms in the parent alloy nanoparticles was essential for determining the final dealloyed nanostructure. Figures 3.6A and B show the formation of porous and core-hollow shell nanoparticles from Au-Ag alloy nanoparticles and Au@Ag-Au double-shell nanoparticles. In Au@Ag-Au double-shell nanoparticles, the Ag atoms distributed around the core region were selectively etched out and formed a hollow structure, and the outermost Au atoms formed a thin-shell nanostructure by reconstructing nearby Au atoms, thereby resulting in a CHS structure (Figure 3.6A). In contrast, the selectively dissolved Ag atoms from the Au-Ag alloy nanoparticles formed many pores, and the remaining well-dispersed Au formed a thin ligament, thereby resulting in a KNB structure (Figure 3.6B). After the Ag atoms were dissolved, the EDS mapping data confirmed that the shells and ligaments of the CHS and KNB structures were predominantly composed of Au, and residual Ag was also present. Additionally, the SAED and wide-angle X-ray diffraction (XRD) patterns were obtained to reveal the

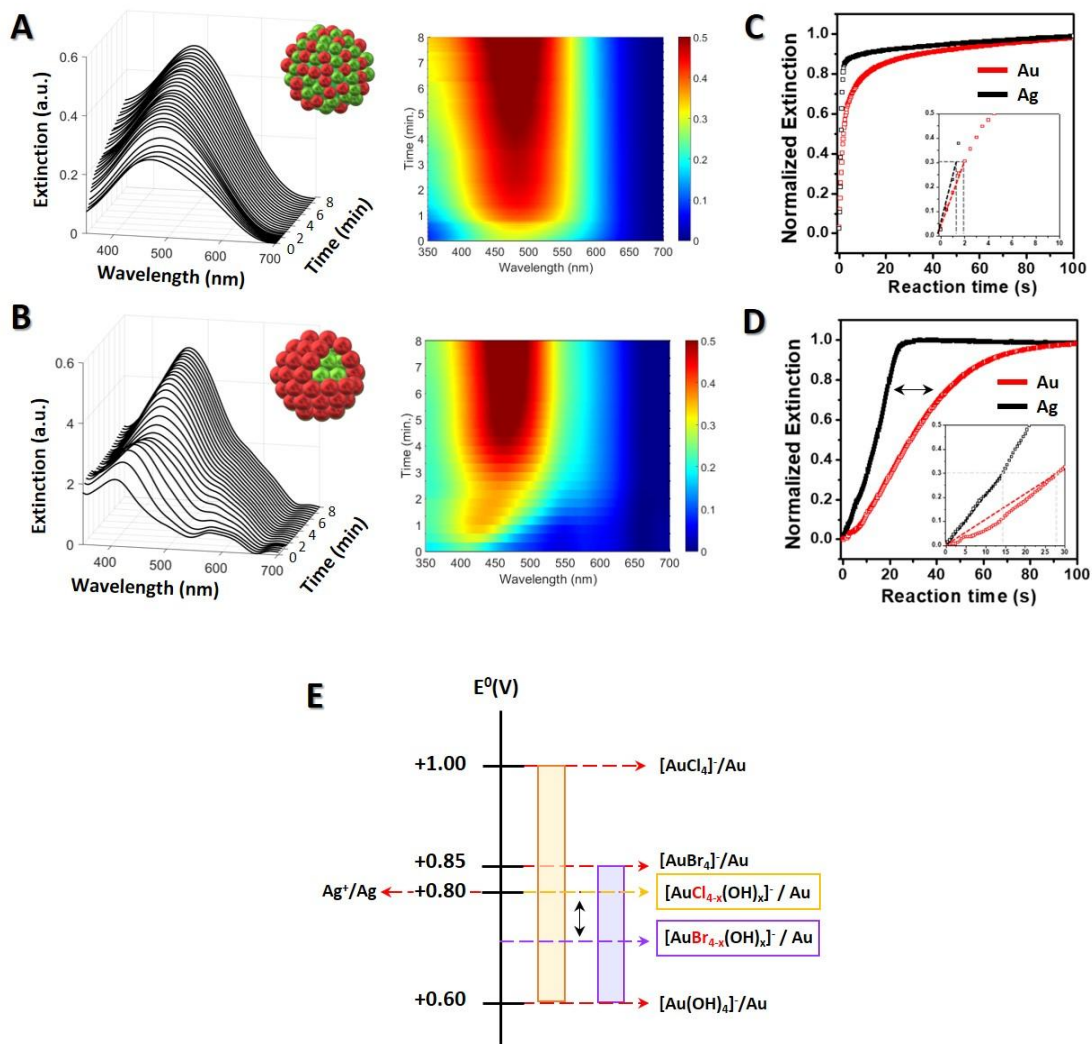


**Figure 3.4 (A-B) Time-dependent UV-vis spectra** showing (A) the consistent band position of SPR absorption in the growth solution of Au-Ag alloy NP and (B) a significant blue shift with time in the solution of Au@Ag-Au double shell NP. The kinetic measurement by tracking the extinction at maximum wavelengths of gold and silver of (C) Au-Ag alloy NP and (D) Au@Ag-Au double shell NP. (E) Schematic illustration of the possible Au complex form and their reduction potential.

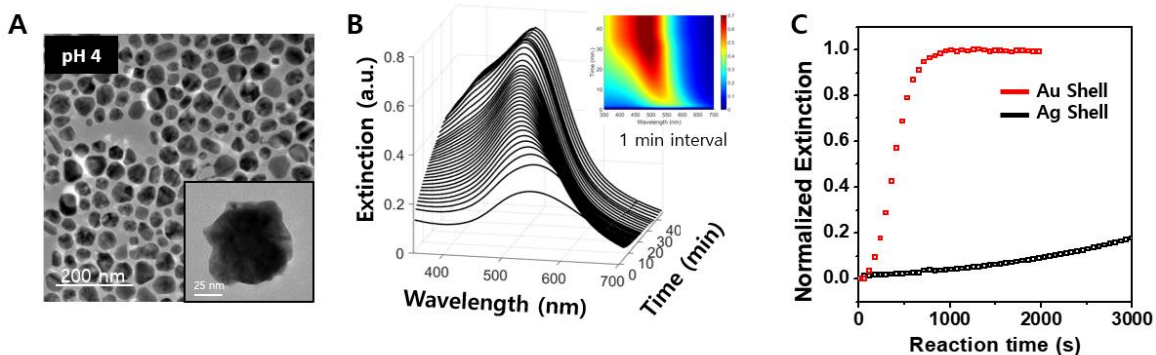


**Figure 3.5 Au-Ag co-reduction in low pH condition.** (A) TEM images of Au and Ag precursor co-reduction on the 10 nm Au seed. (B) Time-dependent UV-vis spectra in 1 min interval showing a significant blue shift with time in the solution. Insets represent contour plots of the changes in the UV vis extinction spectra with increasing irradiation time. (C) Plotting of Maximum extinction peak with time-dependent growth of Au or Ag on the 10 nm core Au nanoparticle.

crystallinity of the CHS and KNB structures (Figure 3.6E). The d-spacing and fcc of Au (JCPDS No. 04-7084 043) and Ag (JCPDS No. 04-0783) were assigned, and the displayed peaks corresponded to the (111), (200), (220), (311) planes, respectively. In the high-resolution TEM (HR-TEM) analysis, the thickness of the shell in the CHS structure was observed to be approximately 12.2 nm, and the Au core used as a seed of the synthesis was clearly visible in the TEM images displaying the inside of the nanoparticle (Figure 3.6C). The average pore size and ligament thickness of KNB were approximately 15 and 10 nm, respectively (Figure 3.6D). Especially in the KNB structure, as the concentration of the etchant increased, the evolution of porosity increased the surface area, as well as the concave and convex curvatures of the ligament. As the concentration of  $\text{Fe}(\text{NO}_3)_3$  increased from 0 to 100 mM, the remaining Ag was completely etched and the pores became large (Figure 3.7A). This feature was also represented in LSPR, which was shifted to high wavelengths when the particle became increasingly hollow (Figure 3.7B). The average size of the KNB nanoparticles was approximately 55 nm, and the average size decreased to 53 nm after dealloying (Figure 3.7C). These results indicated that the remaining components were rearranged during dealloying to reduce their surface energy, and their sizes were decreased. The HR-TEM tilting images of the KNB structures were collected at angles of  $0^\circ$ ,  $15^\circ$ , and  $30^\circ$  in the x-axis direction and  $0^\circ$ ,  $10^\circ$ , and  $20^\circ$  in the y-axis direction (Figure 3.8). The combined HR-TEM tilting images revealed that nanopores were present throughout the nanoparticles and were interconnected by thin ligaments to form a bi-continuous structure (Supporting

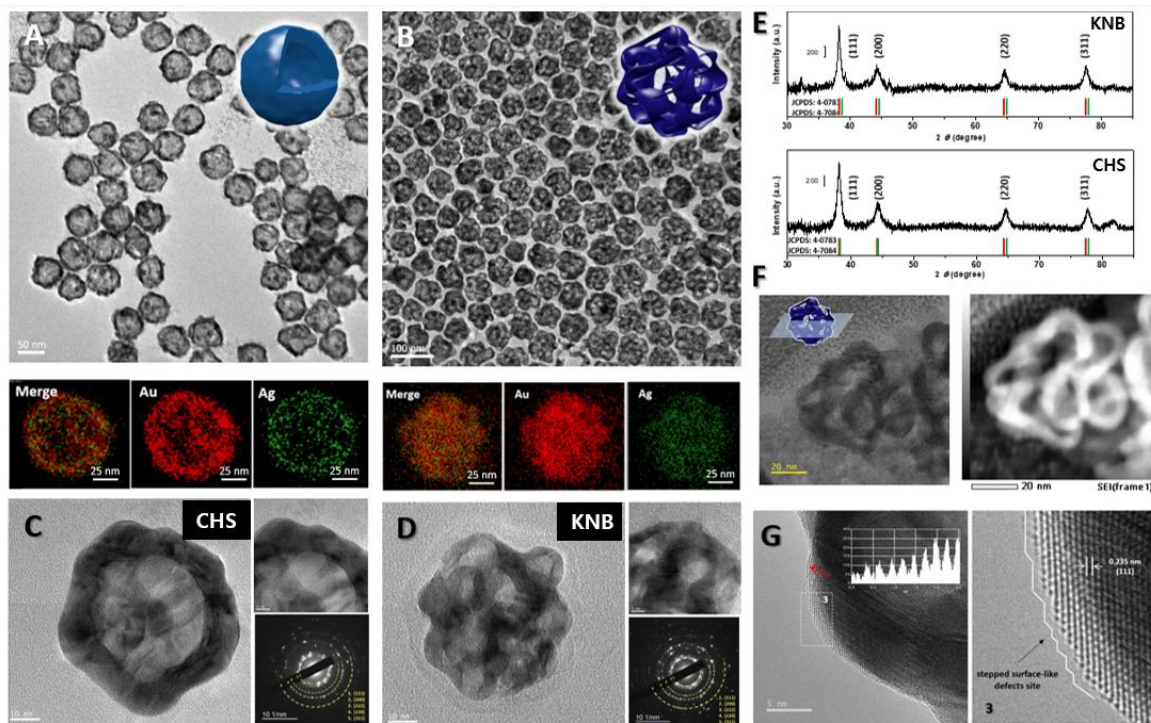


**Figure 3.6 Syntheses and characterization of KNB and CHS.** The TEM image and EDX elemental mapping images of the synthesized (A) CHS, (B) KNB showing a high-yield synthesis of the targeted nanostructures. (C-D) The HR-TEM images and SAED pattern of the ligaments of CHS and KNB (E) (F) TEM and HAADF STEM images of cross section of the KNB obtained by cutting the nanoparticle by using a focused ion beam (FIB). (G) A stepped surface is shown at the surface of the shell and intensity profile obtained from the dotted arrow region, indicates that the shell surface has stepped surface defect sites.

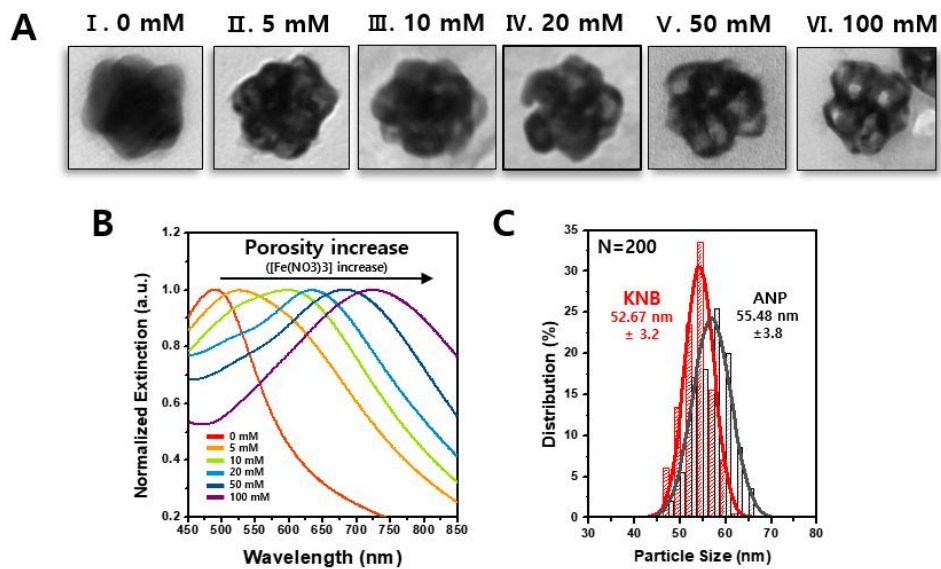


**Figure 3.7 Changes in structure and optical properties of KNB with dealloying reaction.** (A) Structural and Ag/Au atomic ratio changes in KNB with increase in amount of Fe(NO<sub>3</sub>)<sub>3</sub> added. (B) Interior-nanogap-formation-dependent UV-vis spectra of KNB. (C) Particle size distribution of nanoparticle before and after dealloying.

Information, Movie 1). To confirm that the pores and ligaments were formed on the surface and inside the particle, we deliberately cut a specific side of the KNB structure using a focused ion beam. As shown in Figure 3.6F, the TEM and high-angle annular dark-field scanning transmission electron microscopy images display a cross-section of the KNB structure and demonstrate that the pores and ligaments are present deep inside the core regions. In Figure 3.6G, the surface defects derived from the convex curvature of a thin ligament of the KNB structure are confirmed and the intensity profile is obtained in the direction of the arrow. The high-magnification HR-TEM image of the dashed box region clearly reveals stepped surface-like defects that enhanced the catalytic performance of the nanoparticles. One of the most significant advantages of this synthesis method is that the size and porosity of the KNB nanoparticles can be controlled by changing the ratios of the Au and Ag precursor while maintaining the same synthesis protocol. Figure 3.9 shows the TEM images of the KNB nanoparticles, the porosity of which was controlled with an atomic ratio of Au being 20 to 60%. Additionally, the final size of the nanoparticles was adjusted from 50 to 80 nm with the total amount of Au and Ag precursors. Thus far, we have synthesized KNB and CHS structures with completely different structures by controlling the Au distribution of the alloy nanoparticles by simply changing the synthesis environment. Next, we performed EOR with KNBs synthesized with different pore sizes. The EOR changes with the change in the distribution of active sites within a fixed volume. Therefore, we first investigated whether the synthesized Au nanocatalyst exhibited EOR activity. The catalytic performances of the KNB and CHS

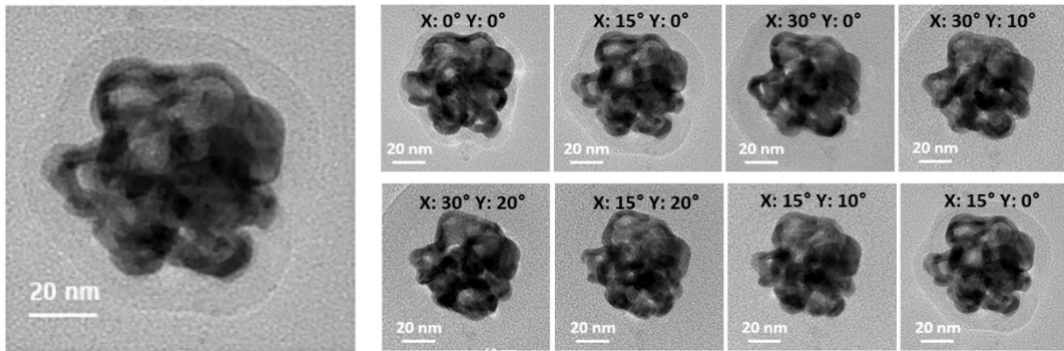


**Figure 3.8** A tilt series of TEM images of an individual KNB for tomography reconstruction. TEM images were collected with the tilt angles of  $-30^\circ$ ,  $-15^\circ$ ,  $0^\circ$ ,  $15^\circ$ ,  $30^\circ$

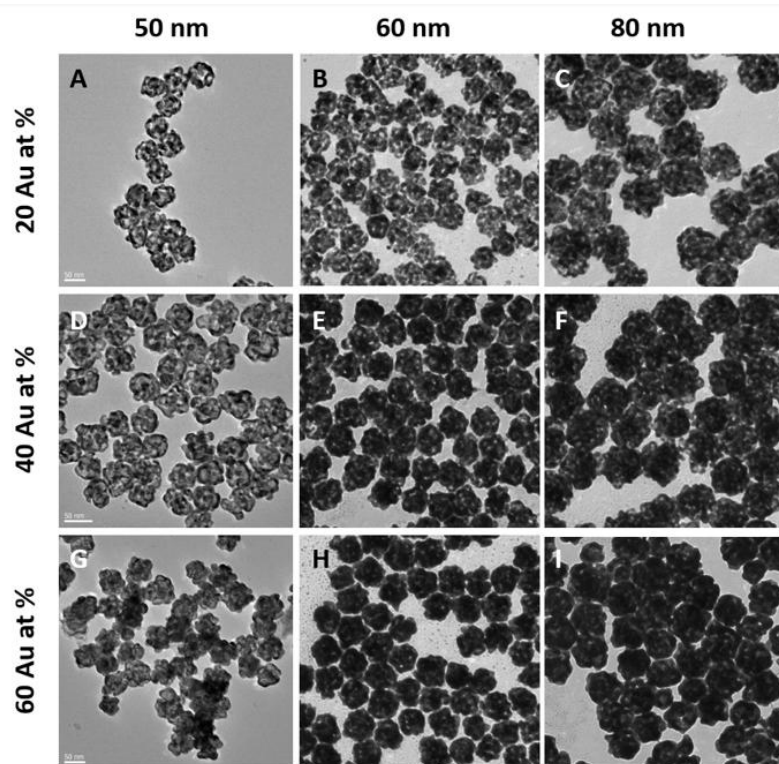


**Figure 3.9 KNB size and composition ratio controllable.** The TEM image of the synthesized KNB size and composition control 50 nm to 100 nm and 20 at % to 60 at %.

nanoparticles were subsequently evaluated using an electrocatalytic EOR in an alkaline solution. Before the electrocatalytic measurements, the catalysts were washed several times with de-ionized water and modified on glassy carbon electrodes for further electrochemical cleaning to thoroughly remove the surfactants within the catalysts (see the Experimental section for more details). To confirm that the electroactivity and oxidation peaks were a result of the oxidation of ethanol owing to the Au catalyst, we conducted cyclic voltammetry (CV) studies in the absence of ethanol and a blank glassy carbon electrode. In the absence of ethanol, in a positive sweeping scan, the CV curve of the KNB nanoparticles exhibited a single broad oxidation peak in the potential range of 0.10–0.40 V (gray trace in Figure 3.10). The reduction peak at 0.10 V corresponded to the Au oxide reduction in the negative sweeping scan. When only the glassy carbon electrode without an Au catalyst was employed, no oxidation peak was observed in the CV curve of the ethanolic solution (black trace in Figure 3.10). This result indicated that the catalytic electrooxidation effect originated from the Au nanocatalysts (red trace in Figure. 3.10). The positions of the two oxidation peaks appearing in the Au-catalyzed EOR reaction were similar to those reported in previous studies.<sup>[26]</sup> This can explain the mechanism of the EOR occurring on the Au surface, which indicated that the reaction with the ethoxy anion was initiated by the hydroxyl group formed by the oxidation of the Au surface. Therefore, the adsorbed hydroxyl group formed on the surface of our synthesized catalyst was a critical factor in the progress of the reaction. Next, by measuring the electrochemically active surface area (ECSA) and catalytic activity of

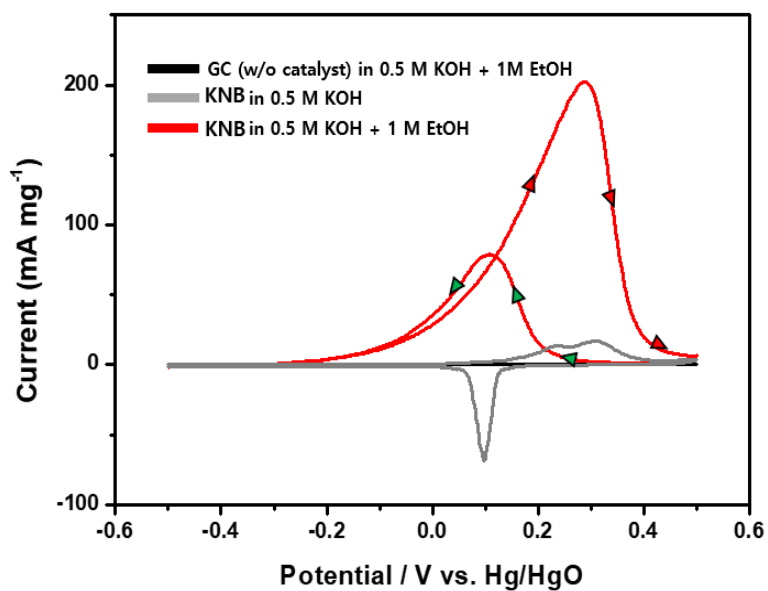


**Figure 3.10** Cyclic voltammetry at various electrochemical set-up. Cyclic voltammograms of KNB and blank glassy carbon in deoxygenated solutions containing 0.5 M KOH with and without 1 M C<sub>2</sub>H<sub>5</sub>OH.

EOR of CHS and KNB nanoparticles, we confirmed the effect of the surface area on the catalytic activity. The ECSAs of the CHS and KNB nanoparticles were measured by performing an electrochemical Au oxide stripping reaction in a 0.5 M H<sub>2</sub>SO<sub>4</sub> aqueous solution at a scan rate of 50 mV·s<sup>-1</sup> at 25 °C (Figure 3.11). The ECSAs were measured by integrating the Au oxide reduction curve close to 0.9 V and assuming a specific charge of 450 mC·cm<sup>-2</sup> for the Au oxide reduction.<sup>[27,28]</sup> As a result, ECSAs of 9.3 and 25.30 m<sup>2</sup>·g<sup>-1</sup> were obtained for the CHS and KNB nanoparticles as catalysts, respectively. The KNB nanoparticles possess 2.7 times higher specific ECSAs for catalysis than that of the CHS nanoparticles. Figure 3.11 shows the CV curves of the CHS and KNB nanoparticles in the presence of 1 M ethanol, in which the characteristic EOR peak was identified in the forward and backward scans. The mass activity current values of the CHS and KNB nanoparticles were 123.2 and 425.3 mA·mg<sup>-1</sup>, respectively, at a scan rate of 50 mV·s<sup>-1</sup>. The KNB nanoparticles as catalysts have an EOR mass activity that is 3.4 times higher than that of the CHS nanoparticles. We confirmed that the electrocatalytic activity obtained by the EOR was strongly correlated with the surface area of the catalyst and the Au atoms efficiently distributed in the same volume were essential for catalytic activity. In addition, the existing Au porous film ligaments demonstrated a limited mass transfer because they are generally very thick (approximately 100 nm). Furthermore, the KNB nanoparticle with a 0D particle structure has a much higher surface-to-volume ratio than that of the KNB nanoparticle with a film structure.

$$\text{ECSA}(\text{m}^2/\text{g}) = \frac{Q(\text{C})}{450(\mu\text{C}/\text{cm}^2) \text{Mass}(\text{g})}$$

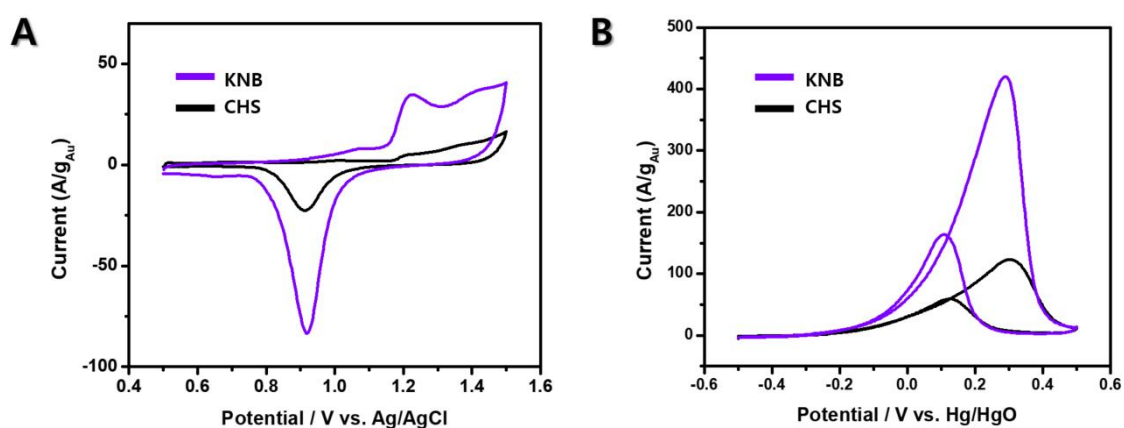


**Figure 3.11 CV curves performed in 0.5 M H<sub>2</sub>SO<sub>4</sub>.** (A) CV curves in 0.5 M KOH electrolyte solutions containing 1 M ethanol. (B) All CV was measured at a potential sweep rate of 50 mV/s. The currents were normalized against the mass loaded on each electrode.

This may have been advantageous in improving the mass transfer and catalytic activity.

An advantage of our proposed synthesis method is that by considering the atomic ratio of Au and Ag in the initial Au-Ag alloy nanoparticles, the pore size can be controlled from 2 to 10 nm even at room temperature. Simultaneously controlling the catalyst structure and amount of Au remaining after dealloying is possible, thereby reducing the amount of expensive noble metals and identifying the optimal catalyst structure that can produce a large surface area. We obtained KNB 60, 40, and 20 as the final products by adjusting the volume ratios of Au and Ag as follows: Au<sub>60</sub>Ag<sub>40</sub>, Au<sub>40</sub>Ag<sub>60</sub>, and Au<sub>20</sub>Ag<sub>80</sub> during the Au-Ag alloy nanoparticle synthesis process (Figures 3.12A–C). Because the KNB 60 alloy nanoparticle was formed with a relatively larger amount of Au than that of Ag, it had very small or no pores owing to low surface diffusivity, although it had the potential to provide many active sites after dealloying. However, in KNB 20, because the amount of Ag was much greater than that of Au in the initial alloy nanoparticle, Au rapidly diffused through the surface and formed large pores during dealloying. Figure 4D shows the corresponding ECSAs were obtained by CV analysis in 0.5 M H<sub>2</sub>SO<sub>4</sub> for synthesized alloy nanoparticle which consist with Au 40 Ag60 (ANP 40), KNB 60, 40, and 20. The calculated ECSA values for ANP 40, KNB 60, 40, and 20 were 8.2, 14.3, 25.3, and 19.34, respectively, and the ECSA per unit Au mass was highest for KNB 40 (Figure 3.12F). The EOR results were in good agreement with the trend shown by the ECSAs. The mass activity of ANP 40, KNB 60, 40, and 20 was 20.1, 64.8, 425.3, and 266.78, respectively (Figure 3.12E). KNB 40 showed the highest mass activity, which

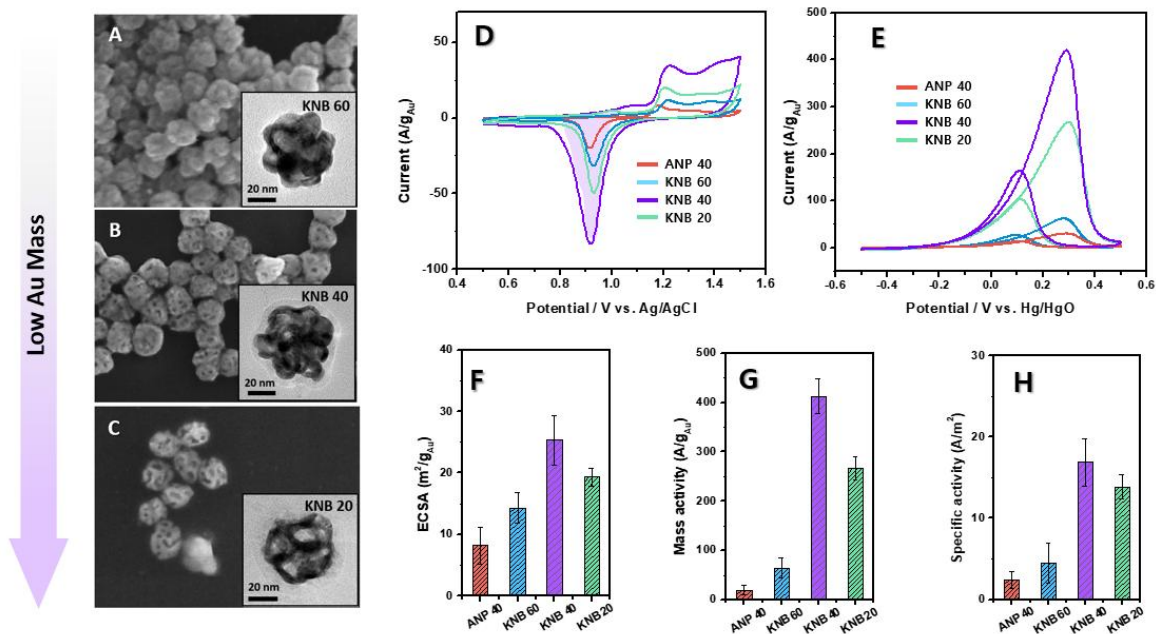


**Figure 3.12** (A) The SEM and TEM images of the synthesized (A) KNB 60, (B) KNB 40 and (C) KNB 20. (D) CV curves of ANP 40, KNB 60, KNB 40 and KNB 20 in 0.5 M H<sub>2</sub>SO<sub>4</sub> and (E) in 0.5 M KOH electrolyte solutions containing 1 M ethanol at a potential sweep rate of 50 mV/s . (F) Electrochemically Active Surface Area (ECSA), (G) Mass activities and (H) specific activities.

was 21, 15, 8, and 2 times higher than that of ANP, KNB 60, and KNB 20, respectively (Figure 3.12G). The mass activity is greatly affected by the amount of Au catalyst used and the efficiency with which the Au atoms are distributed and exposed on the surface. Therefore, KNB 40 displayed the optimal structure with the highest mass activity in the EOR because Au was efficiently distributed over a large surface area. The Au mass activity of KNB 40 obtained in our study was the highest for the Au catalyst used for the EOR (Table 1).<sup>[16,29–33]</sup> Chronoamperometry analysis showed that the catalytic activity of KNB was robust (Figure 3.13A). By monitoring the change in the electrocatalytic current in a 0.28 V continuous working environment, KNB 40 was confirmed to retain a specific current of approximately 50 mA/mg after 2000 s of electrocatalysis. We further performed CV measurements on KNB 40 at different potential sweep rates ( $v$ ) for the EOR (Figure 3.13B). The peak current ratio of the forward to backward ( $I_f/I_b$ ) scan reveals the resistance of catalysts to the accumulation of carbonaceous species.<sup>[16]</sup> A high  $I_f/I_b$  value indicates a complete oxidation process with less accumulation of residual carbonaceous species. As  $v$  increased,  $I_f/I_b$  also increased, thereby indicating that, with a fast potential sweep, the resistance to the accumulation of carbonaceous species becomes increasingly robust. Additionally, the molecular diffusion rates differ inside and outside the porous Au structure owing to the nanoconfinement effect induced by the complex local curvature ligaments.<sup>[34]</sup> The forward peak current possesses a linear relationship with the square root of the scan rate ( $v^{1/2}$ , Figure 3.13C). This result suggested that electrocatalytic reactions involving KNB 40 may include simple diffusion or surface-

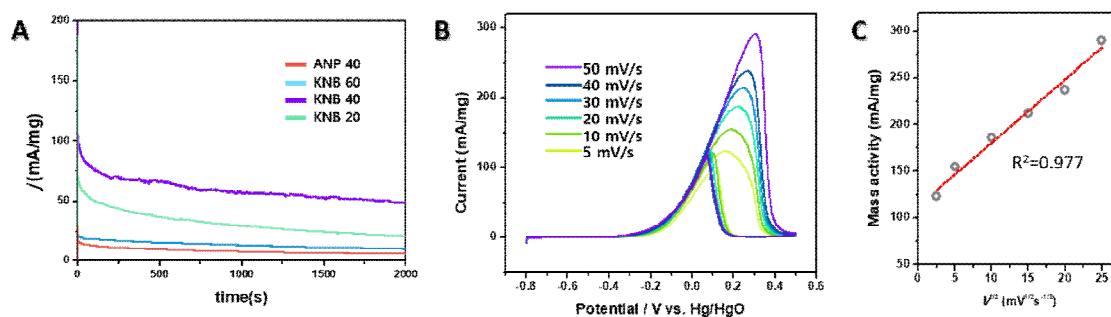


**Figure 3.13 (A) Chronoamperometric results of EOR at 0.28 V on ANP 40, KNB 60, KNB 40 and KNB 20 in 0.5 M KOH + 1.0 M ethanol solution. (B) CV curves of KNB 40 with a scan rate of 5, 10, 20, 30, 40, 50 mV/s in 0.5 M KOH and 1.0 M ethanol. (C) The linear relationship between the forward peak current and square root of scan rate ( $v^{1/2}$ ).**

controlled processes on the nanoligament surface. Additionally, the specific activity (the mass activity per unit area) of KNB 40 and 20 was 16.9 and 13.9  $\text{A}\cdot\text{m}^{-2}$ , respectively, which was higher than that of 5.6 nm-sized Au nanoparticles ( $13.4 \text{ A}\cdot\text{m}^{-2}$ ) (Figure 3.12H).<sup>[32]</sup> The high surface activity of small-sized Au nanoparticles indicates that supporting materials, such as Ti and C, must be used for stability. However, the KNB nanoparticles do not require supporting material because of their high surface activity and stability, which is a substantial advantage.

Interestingly, nanosponge Au, which has a structure similar to that of KNB, has a high surface area but a relatively low specific activity of  $4.1 \text{ A}\cdot\text{m}^{-2}$ .<sup>[16]</sup> Therefore, we performed an underpotential deposition of Pb (Pb-UPD) on KNB 60, 40, and 20 assuming that the specific facet formed on the ligament affected the catalytic activity. The Pb-UPD peak potentials are beneficial for identifying different types of surface facet information.<sup>[36]</sup> The results of the Pb-UPD voltammetry profile in the range of  $-0.7$ – $-0.1$  V showed different patterns for KNB 60, 40, and 20 (Figure 3.15). In the Pb-UPD voltammetry traces for each particle, four major peaks were clearly distinguished. The peaks of approximately  $-0.35$ ,  $-0.47$ ,  $-0.53$ , and  $-0.63$  V corresponded to the  $\{110\}$  facet,  $\{100\}$  facet,  $\{111\}$  facet, and step/kink structures, respectively.<sup>[29,35]</sup> To quantitatively estimate the proportions of the different facets on each particle surface, the Pb-UPD peaks were deconvoluted (Figure 3.14). The proportion of each facet was obtained by normalizing the charge value of Pb for the different facets. From the results in Figure 3.14, the  $\{111\}$  and step/kink fractions for KNB 40 were 23.9 and 13.0%, respectively,

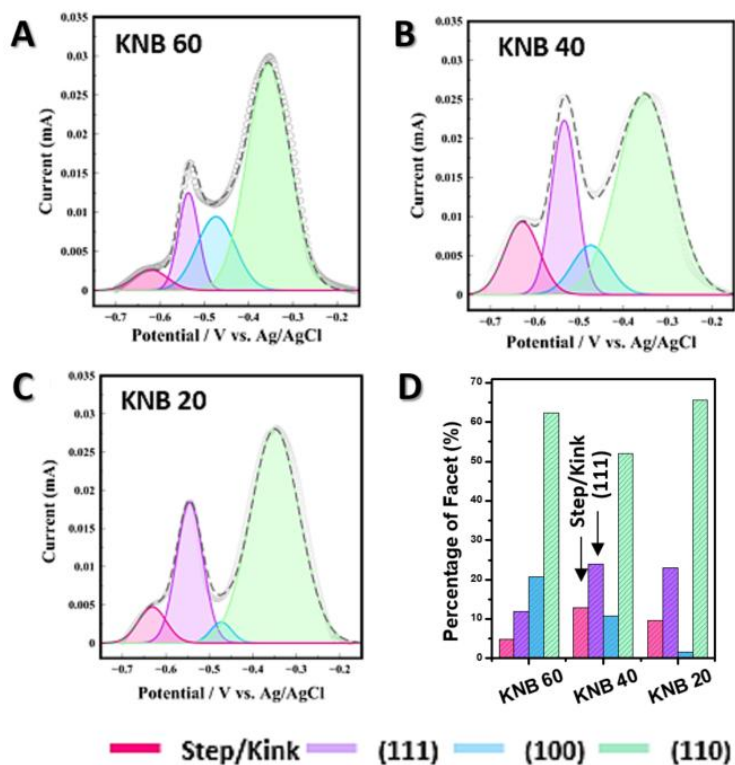


**Figure 3.14** Underpotential deposition of lead (pb-UPD) of (A) KNB 60, (B) KNB 40, (C) KNB 20 and (D) the percentages of different facets in Au-Ag alloy 40 and KNB 40. Pb-UPD in 0.1 M NaOH + 1 mM Pb(NO<sub>3</sub>)<sub>2</sub>. Scan rate: 50 mV/s.

which were the highest when compared with KNB 20 (22.8, 9.7%) and 60 (11.9, 4.9%). High-index planes were mainly identified together with low-index planes. In particular, the {111} plane is known to stabilize concave and convex curvatures while forming a flat terrace on the ligament surface.<sup>[36]</sup> This structural configuration imparted additional stability to the KNB nanoparticles. The percentages of {100} were 20.7%, 10.8%, and 1.6% for KNB 60, 40, and 20, respectively. The proportions of {110} facets were the highest in all the KNB nanoparticles, which were 62.3%, 52.1%, and 65.6% for KNB 60, 40, and 20, respectively.

Au reconstruction is a kinetically controlled process because a high concentration of Ag etchant is used in the synthesis of KNB nanoparticles. Therefore, for KNB 60, 40, and 20, the {110} plane with the highest surface free energy developed with the highest proportions. We hypothesized that a change in the proportion of the facets in the KNB nanoparticles according to the change in pore size may profoundly affect the specific activity obtained from EOR. In previous studies, the catalytic activity in alcohol electrooxidation reactions, including EOR in an alkaline solution, is known to be the highest for catalysts containing steps/kinks and {111}.<sup>[29,35,37,38]</sup> Additionally, the catalytic activity is known to be in the order of {100} and {110}. In particular, the generally known surface free energy ( $\gamma(111)$  ( $1.52 \text{ J}\cdot\text{m}^{-2}$ )  $<$   $\gamma(100)$  ( $1.80 \text{ J}\cdot\text{m}^{-2}$ )  $<$   $\gamma(110)$  ( $1.94 \text{ J}\cdot\text{m}^{-2}$ ) shows the opposite trend in low index facets.<sup>[39]</sup> This trend can be explained by the adsorption density per unit area and surface free energy after the adsorption of the surface hydroxyl groups that affect the overall EOR.<sup>[38]</sup> The {111} facet has the most

closely packed arrangement of atoms per unit surface area among the low Miller indices. This characteristic induces the surface hydroxyl group to be adsorbed on the surface with a high density, and the surface energy of {111} increases after adsorption, thereby increasing the alcohol electrooxidation efficiency. The trends of the specific activities of KNB 40, 60, and 20 correspond to the proportion of the {111} facet and step/kink formed on the surface. These results suggested that the structure of the Au catalyst and the facet of the ligament play an essential role in the EOR.

### **3.4 Conclusion**

In conclusion, we developed a novel synthesis method for the design of Au-Ag alloy nanoparticles and porous nanostructures. The synthesis method developed in this study controlled the reduction rates of Au and Ag by changing the synthesis environment. This was determined the distribution of Au and Ag in the nanoparticles at room temperature. Additionally, nanoparticles with various surface areas were formed using the dealloying reaction. Among KNBs with various porosity, KNB 40 nanoparticles showed the highest ECSA and mass activity of EOR. In addition, through the Pb-UPD measurements and facet proportion analysis in KNB nanoparticles, the step/kink and {111} facets were confirmed to be major factors influencing the high specific activity obtained from the EOR. Our results show that the highest EOR activity was found in KNB 40, suggesting that it is important to have a large ECSA and efficiently distribute the abundant surface defect and {111} facets which is the origin of catalytic activity.

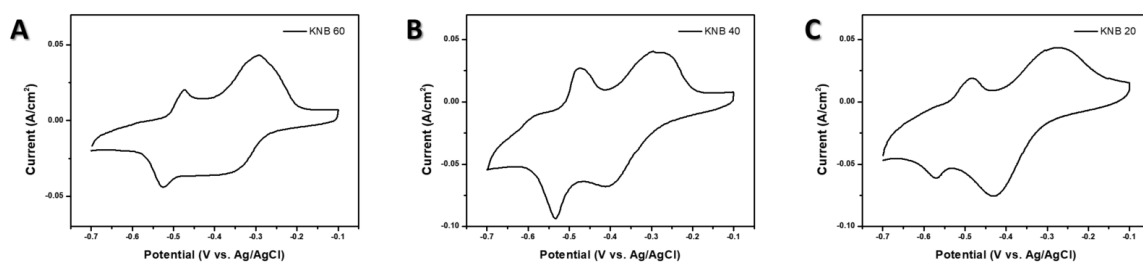


**Figure 3.15 Underpotential deposition of lead (pb-UPD) of (A) KNB 60, (B) KNB 40 (C) KNB 20 in 0.1 M NaOH + 1 mM Pb(NO<sub>3</sub>)<sub>2</sub>. Scan rate: 50 mV/s.**

\*  = 0-D Nanoparticle

Catalyst	Mass Activity (A/g)	Specific activity (A/m <sup>2</sup> )	ECSA (m <sup>2</sup> /g)
<b>Knotted Nano Ball 40</b>	<b>425.3</b>	<b>16.9</b>	<b>25.3</b>
L-NPG <sup>[1]</sup>	374	55	6.8
Nanosponge Au <sup>[2]</sup>	328	4.1	80
Au nanocorals <sup>[3]</sup>	169.5	15	11.3
Au dendritic nanostructures <sup>[4]</sup>	137.4	20.8	6.6
Au nanoparticle (5.6 nm) <sup>[5]</sup>	81.9	13.4	6.1
Au nanodendrites <sup>[6]</sup>	30.6	1.96	15.3

[1] Mingwei Chen \* et. al., *Adv. Mater.*, 1703601 (2017)

[2] Hui Wang \* et. al., *Nano Lett.*, 16, 7248 (2016)

[3] Tianhong Lu\* et. al., *CrystEngComm.*, 16, 8576 (2014)

[4] Tianyan You\* et. al., *ACS Appl. Mater. Interfaces*, 5, 9148 (2013)

[5] Tongfei Lia\* et. al., *Electrochim. Acta.*, 231, 13 (2017)

[6] Ai-Jun Wang\* et. al., *ACS Appl. Mater. Interfaces.*, 4, 2570 (2012)

**Table 1.1 Comparison of the activities of various Au catalyst for EOR.**

### 3.5 Reference

- [1] M. Haruta, T. Kobayashi, H. Sano, N. Yamada, *Chem. Lett.* **1987**, *16*, 405.
- [2] M. Valden, X. Lai, D. W. Goodman, *Science (80-. )*. **1998**, *281*, 1647.
- [3] G. W. Brudvig, T. M. Iverson, K. Maghlaoui, J. Barber, S. Iwata, J. Kern, W. Saenger, A. Zouni, J. Biesiadka, M. Haumann, K. Kawakami, J. R. Shen, N. Kamiya, R. H. Crabtree, G. W. Brudvig, A. Grundmeier, P. Loja, M. Haumann, J. W. Murray, V. L. Pecoraro, G. Christou, M. Yagi, M. Kaneko, S. Mukhopadhyay, S. K. Mandal, S. Bhaduri, W. H. Armstrong, A. Mishra, W. Wernsdorfer, K. A. Abboud, G. Christou, V. Kotzabasaki, M. Siczek, T. Lis, C. J. Milios, S. Nayak, H. P. Nayek, S. Dehnen, A. K. Powell, J. Reedijk, Y. J. Park, J. W. Ziller, A. S. Borovik, E. Y. Tsui, M. W. Day, T. Agapie, E. Y. Tsui, J. S. Kanady, M. W. Day, T. Agapie, J. Yano, V. K. Yachandra, J. P. Mcevoy, J. A. Gascon, V. S. Batista, G. W. Brudvig, J. Messinger, M. Arjomand, D. J. Machin, W. Levason, C. A. Mcauliffe, M. D. Symes, Y. Surendranath, D. A. Lutterman, D. G. Nocera, M. W. Kanan, D. G. Nocera, T. Ehrenberg, M. Wiechen, P. Kurz, S. V Baranov, G. M. Ananyev, G. C. Dismukes, J. Kazimir, G. M. Cheniae, **2011**, 736.
- [4] Y. Kuwauchi, H. Yoshida, T. Akita, M. Haruta, S. Takeda, *Angew. Chemie - Int. Ed.* **2012**, *51*, 7729.
- [5] A. Wittstock, V. Zielasek, J. Biener, C. M. Friend, M. Bäumer, *Science (80-. )*. **2010**, *327*, 319.
- [6] V. Zielasek, B. Jürgens, C. Schulz, J. Biener, M. M. Biener, A. V. Hamza, M. Bäumer, *Angew. Chemie - Int. Ed.* **2006**, *45*, 8241.
- [7] C. Xu, J. Su, X. Xu, P. Liu, H. Zhao, F. Tian, Y. Ding, *J. Am. Chem. Soc.* **2007**, *129*, 42.
- [8] R. Liquid, J. Erlebacher, M. J. Aziz, A. Karma, N. Dimitrov, *Nature* **2001**, *410*, 5.

- [9] J. Biener, M. M. Biener, R. J. Madix, C. M. Friend, *ACS Catal.* **2015**, *5*, 6263.
- [10] G. G. Li, H. Wang, *ChemNanoMat* **2018**, *4*, 897.
- [11] P. Liu, P. Guan, A. Hirata, L. Zhang, L. Chen, Y. Wen, Y. Ding, T. Fujita, J. Erlebacher, M. Chen, *Adv. Mater.* **2016**, *28*, 1753.
- [12] Y. Ding, Y. J. Kim, J. Erlebacher, *Adv. Mater.* **2004**, *16*, 1897.
- [13] D. Wang, P. Schaaf, *J. Mater. Chem.* **2012**, *22*, 5344.
- [14] G. Hyun, J. T. Song, C. Ahn, Y. Ham, D. Cho, J. Oh, S. Jeon, *Proc. Natl. Acad. Sci. U. S. A.* **2020**, *117*, 5680.
- [15] K. Liu, Y. Bai, L. Zhang, Z. Yang, Q. Fan, H. Zheng, Y. Yin, C. Gao, *Nano Lett.* **2016**, *16*, 3675.
- [16] G. G. Li, Y. Lin, H. Wang, *Nano Lett.* **2016**, *16*, 7248.
- [17] Y. Yi, X. Zheng, Z. Fu, C. Wang, X. Xu, X. Tan, *Materials (Basel)*. **2018**, *11*, DOI 10.3390/ma11030380.
- [18] I. McCue, E. Benn, B. Gaskey, J. Erlebacher, *Annu. Rev. Mater. Res.* **2016**, *46*, 263.
- [19] M. Di Vece, N. P. Young, Z. Li, Y. Chen, R. E. Palmer, *Small* **2006**, *2*, 1270.
- [20] Y. Wang, J. He, C. Liu, W. H. Chong, H. Chen, *Angew. Chemie - Int. Ed.* **2015**, *54*, 2022.
- [21] M. Ha, J. H. Kim, M. You, Q. Li, C. Fan, J. M. Nam, *Chem. Rev.* **2019**, *119*, 12208.
- [22] X. Xia, Y. Wang, A. Ruditskiy, Y. Xia, *Adv. Mater.* **2013**, *25*, 6313.
- [23] G. Gramlich, J. Zhang, W. M. Nau, *J. Am. Chem. Soc.* **2002**, *124*, 11252.
- [24] M. D. and A. G. Corby, *Icmm* **2009**, *1*.
- [25] M. D. Urović, R. Puchta, Ž. D. Bugarčić, R. Van Eldik, *Dalt. Trans.* **2014**, *43*, 8620.
- [26] Y. Zhang, J. G. Wang, X. Yu, D. R. Baer, Y. Zhao, L. Mao, F. Wang, Z. Zhu, *ACS Energy Lett.* **2019**, *4*, 215.

- [27] S. Pedireddy, H. K. Lee, W. W. Tjiu, I. Y. Phang, H. R. Tan, S. Q. Chua, C. Troadec, X. Y. Ling, *Nat. Commun.* **2014**, *5*, 1.
- [28] Y. H. Tan, J. A. Davis, K. Fujikawa, N. V. Ganesh, A. V. Demchenko, K. J. Stine, *J. Mater. Chem.* **2012**, *22*, 6733.
- [29] Z. Wang, S. Ning, P. Liu, Y. Ding, A. Hirata, T. Fujita, M. Chen, *Adv. Mater.* **2017**, *29*, 1.
- [30] Z. Liu, G. Fu, Y. Tang, D. Sun, Y. Chen, T. Lu, *CrystEngComm* **2014**, *16*, 8576.
- [31] J. Huang, X. Han, D. Wang, D. Liu, T. You, *ACS Appl. Mater. Interfaces* **2013**, *5*, 9148.
- [32] T. Li, G. Fu, J. Su, Y. Wang, Y. Lv, X. Zou, X. Zhu, L. Xu, D. Sun, Y. Tang, *Electrochim. Acta* **2017**, *231*, 13.
- [33] J. J. Feng, A. Q. Li, Z. Lei, A. J. Wang, *ACS Appl. Mater. Interfaces* **2012**, *4*, 2570.
- [34] M. A. Mahmoud, R. Narayanan, M. A. El-Sayed, *Acc. Chem. Res.* **2013**, *46*, 1795.
- [35] Z. Wang, P. Liu, J. Han, C. Cheng, S. Ning, A. Hirata, T. Fujita, M. Chen, *Nat. Commun.* **2017**, *8*, 1.
- [36] T. Fujita, P. Guan, K. McKenna, X. Lang, A. Hirata, L. Zhang, T. Tokunaga, S. Arai, Y. Yamamoto, N. Tanaka, Y. Ishikawa, N. Asao, Y. Yamamoto, J. Erlebacher, M. Chen, *Nat. Mater.* **2012**, *11*, 775.
- [37] S. Beyhan, K. Uosaki, J. M. Feliu, E. Herrero, *J. Electroanal. Chem.* **2013**, *707*, 89.
- [38] K. Shen, C. Jia, B. Cao, H. Xu, J. Wang, L. Zhang, K. Kim, W. Wang, *Electrochim. Acta* **2017**, *256*, 129.
- [39] Y. N. Wen, J. M. Zhang, *Solid State Commun.* **2007**, *144*, 163.

## 고도로 제어된 귀금속 나노구조체 합성 및 광학/촉매 특성

최근 금속 나노입자의 응용이 다양해지고 있으며, 그 응용을 위해 입자를 고도로 제어하는 것이 더욱 중요해지고 있다. 따라서 나노 입자를 고도로 제어하는 방법을 이해하면 광학 및 촉매 응용 분야에서 보다 적합한 구조로 나노 입자를 설계하고 합성하는 데 통찰력을 얻을 수 있다. 여기에서는 정량적 표면 강화 라만 산란(SERS) 및 고효율 전기 산화 에탄올 반응(EOR)을 위한 최적의 금속 나노구조를 제시한다. SERS로 알려진 고도로 향상된 라만 산란은 거친 은 표면에 흡수된 분자에 의해 처음 발견되었다. 그 이후로 많은 연구에서 금속 나노입자 사이의 국부 전자기장 영역에 라만 분자를 증착하여 단일 분자 검출 수준 SERS에 대해 보고하고 있다. 그 중 nm 규모의 내부 갭을 갖는 나노구조는 갭 내부에 라만 분자가 위치하고 갭 크기가 고정되어 있어 SERS 신호의 신뢰성, 정량성 및 높은 안정성을 보인다. 현재까지 내부갭 나노입자에 대한 최근 연구는 새로운 합성 방법을 개발하거나 실제 응용 가능성을 보여주는 데 중점을 두고 있다. 다양한 합성 방법이 개발되었지만 균일하고 안정적인 SERS 신호에 대해 내부갭을 엄격하게 제어하여 갭 모양의 영향을 비교하는 연구는 수행되지 않았다. 따라서, 잘 정의되고 높은 수율의 나노입자로 SERS의 EF(Enhancement factor)의 좁은 분포를 가지는 내부갭 입자를 합성하고 이를 균일

하지 못한 내부갭 나노입자와 비교함으로써 갭 모양에 대한 영향을 연구할 기회가 여전히 있다.

Au 나노다공성 구조는 높은 표면 대 부피 구조적 특성으로 인해 전기화학 반응 촉매로 널리 사용되어 왔다. 기존의 Au 나노다공성 구조의 대부분은 박막인데, Au 나노다공성 필름에 비해 Au 다공성 나노입자는 표면 대 부피비가 더 높고 인대가 작은 부피에서 더 휘어져 필연적으로 많은 표면 결함을 노출시킨다. 이러한 이유로 Au 나노다공성 구조는 고급 촉매 성능을 보이며 널리 연구되어 왔으며 기존의 Au 나노 다공성 구조의 합성 방법은 복잡하고 어려웠던 다단계 합성 조건을 포함하고 있으므로 온화한 조건에서 Au 나노다공성 입자를 고수율로 쉽게 합성할 수 있는 방법을 고안해야 한다.

본 학위논문에서는, 가장 효율적인 광학 및 촉매 성능을 위해 금(Au)과 은(Ag)으로 구성된 고도로 제어된 금속 나노구조 제조 방법을 제시한다. 특히 신뢰할 수 있고 정량적인 SERS 적용을 위해 Au 나노 입자의 내부 간극 모양을 고도로 제어하고 광학 균일성과 안정성의 효과를 조사했다. 또한, Au 기반 나노 입자의 전기 촉매 효율을 향상시키기 위해 공동 환원 화학 및 탈 합금 반응을 기반으로 Au-Ag 다공성 나노 입자를 합성하였다. 합성 과정에서 Au 대 Ag 비율을 조정함으로써 나노 입자의 다공성 및 표면 결함 의존적 촉매 활성을 쉽게 제어하고 조사할 수 있었다.

1장에서는 귀금속 나노입자 합성 및 다양한 응용에 대한 개요를 설명한다. 먼저, 고수율 나노입자 및 첨단구조의 제조 및 제어방법을 소개한다. 다음으로, 우리는 다양한 응용, 특히 SERS 및 금속 나노입자 촉매에 영향을 주는 요인들에 대해 조사한다.

2장에서는 신뢰할 수 있고 정량적인 표면 강화 라만 산란(SERS)을 위한 고도로 제어된 단결정 평활 갭 내 나노입자(SSIN)를 제시한다. 우리는 각 나노 입자의 증폭된 SERS 강도와 균일성에 대한 내부 갭 모양의 영향을 조사하고 이를 다결정질 거친 내부 갭 나노 입자(PRIN)와 비교했다.

3장에서는 고다공성 Au-Ag Alloy Knotted Nano Ball(KNB)의 합리적인 설계를 제시한다. 종자 매개 성장 동안 Au 및 Ag의 상대적 환원 속도를 정확하게 조절하고 이어 합금 해제 반응을 하여 다공성인 Au-Ag Alloy KNB를 형성하였다. 이 방법은 다양한 기공 크기 나노입자를 합성하기 위해 쉽게 조정할 수 있다. KNB 나노입자의 최적화된 기공 크기는 에탄올 반응(EOR)의 전기 산화에서 Au 기반 촉매 중에서 가장 높은 질량 활성을 보였다. 특히, 상이한 나노구조 상의 인대의 표면 결함의 비율이 EOR 반응의 mass activity 및 specific activity에 중요한 역할을 한다고 주장한다. 이러한 합성 전략과 KNB 나노입자의 EOR에 대한 결과는 손쉽게 합성된 KNB 다공성 나노구조가 높은 활성을 나타내는 나노촉매로의 가능성을 보여주었다.

결론적으로, 잘 설계된 고수율 나노입자는 특정 응용 분야에서 최대 효율을 가져올 것이며 미래에 나노입자의 실제 상업적 사용에 필수적이 될 것입니다. 이러한 이유로 응용분야에 영향을 주는 요소들과 나노입자를 원하는 모양으로 제어할 수 있는 종합적인 이해가 필수적이다.

**주요어** : 귀금속 나노구조, 플라즈몬 인트라갭 나노입자, 나노다공성 금구조, 표면강화라만산란(SERS), 전기-에탄올 산화 반응

**학생번호** : 2015-20397